THE INFLUENCE OF SURFACTANTS ON THE CHARACTERIZATION STUDIES OF COPPER OXIDE NANOMATERIALS FOR PHOTOCATALYTIC AND SUPERCAPACITOR APPLICATIONS

A THESIS

Submitted by

S.MUTHURANI

(Reg. No. 12048)

PHYSICS

in partial fulfillment of the requirements for the award of degree of

DOCTOR OF PHILOSOPHY

MANONMANIAM SUNDARANAR UNIVERSITY

TIRUNELVELI – 627 012

TAMILNADU, INDIA

APRIL - 2018

MANONMANIAM SUNDARANAR UNIVERSITY

TIRUNELVELI - 627 012

CERTIFICATE

The research work embodied in the present Thesis entitled **"THE INFLUENCE OF SURFACTANTS ON THE CHARACTERIZATION STUDIES OF COPPER OXIDE NANOMATERIALS FOR PHOTOCATALYTIC AND SUPERCAPACITOR APPLICATIONS"** has been carried out in the **Department of Physics, St. Xavier's College (Autonomous), Palayamkottai, Tamil Nadu**. The work reported herein is original and does not form part of any other thesis or dissertation on the basis of which a degree or award was conferred on an earlier occasion or to any other scholar.

I understand the University's policy on plagiarism and declare that the thesis and publications are my own work, except where specifically acknowledged and has not been copied from other sources or been previously submitted for award or assessment.

S. MUTHURANI

RESEARCH SCHOLAR

Dr. D. PREM ANAND
Research Supervisor &
Head of the Department
Department of Physics,
St. Xavier's College (Autonomous),
Palayamkottai – 627 002,
Tamil Nadu

ACKNOWLEDGEMENT

First and foremost, I would like to thank **The God Almighty** who blessed me and given wisdom to complete my research work.

I wish my sincere and profound gratitude to my supervisor, **Dr. D. Prem Anand,** Head of the Department of Physics, St. Xavier's College (Autonomous), Palayamkottai for getting registered and permitting me to do the project under his guidance. He has given me constant guidance, supervision, valuable suggestions and motivation in each and every step of my research work. I take this as the most appropriate moment to thank him for his guidance and support in all the times.

I am thankful to **Rev. Dr.V. Britto, S.J.** Principal, and, **Rev. Dr.Gilburt Camillus, S.J.** former Principal, St. Xavier's College (Autonomous), Palayamkottai for their blessings and permission to pursue research in Physics research centre at St. Xavier's College (Autonomous), Palayamkottai.

I offer my sincere thanks to **Dr. G. Hirankumar,** Assistant Professor, Department of Physics, Vivekananda college Chennai formerly working at PSN college of engineering of science and technology who gave me an opportunity to use the laboratory and valuable discussions about my research work. **Ms. S. Abarna** and **Dr. Muthupoongodi** , Research scholars, PSN, Tirunelveli who helped to handle the instruments and for their wonderful discussions regarding the application part of my project.

I would like to thank **Mr. J. Victor, Administrative Staff, St. Xaveir's College** for introduce my guide and helping me to do this project in this institute. I also thank his family for their blessings and prayers.

I thank **Dr. S. Paulraj**, **Dr. V. Sivashankar**, **Dr. G. David Rathinavelu, Dr. B. Helina, Dr. R. Mary Jenila, Dr. S. Anna Venus, Dr. S. G. Rejith, Dr. M. Augustin,** and **Dr. L. Arun Jose,** Department of physics, St. Xavier's College (Autonomous), Palayamkottai for their motivation and support.

I also grateful to my co researchers **Dr. K. Daries Bella, Mr. M. Ambrose Raj kumar,** and **Ms. D. Sathya,** PG student **Mr. P. Ajith**, lab assistant **Mr. Rajaguru @ Rex,** for their timely help and support throughout my research work.

Words alone are insufficient as I attempt my deep sense of gratitude to my soul mate, my spouse **D. Arunachalam**, and my son **A. Bharani Arun** for their abundant love, care and moral support. I am extremely grateful to them for the successful completion of the thesis and this research work would not be possible without their sacrifice.

I express my heartfelt gratitude to my parents **V. Shunmugam, S. Muthulakshmi** and my parent in-laws **A. Palavesam, P. Muthammal** for their boundless love, motivation, taking care on my child, constant support and encouragement. I would like to express my thanks to my lovely sister **S. Revathypapathi** and all **my brothers**for her affectionate attitude and incomparable understanding.

I express my thanks to my brother –in law **Mr. C. Siva**, proprietor, Laser Express, Palay for his motivation, moral support, encouragement and his help during the printing stage of the thesis.I also extend my thanks to my all my **relatives** and **friends** who have directly and indirectly motivated and encouraged during my research.

The services rendered by C-SAR, PSN College, Tirunelveli, St. Joseph's College, Trichy, Kalasalingam University, Srivilliputhur, Manonmaniam Sundaranar University, Tirunelveli are gratefully acknowledged.

S. MUTHURANI

CONTENTS

Chapter – IX

Applications

Chapter - X

Summary, Conclusions and Suggestions for future work

REFERENCE

APPENDICES

LIST OF TABLES

LIST OF FIGURES

LIST OF ABBREVIATIONS AND SYMBOLS

%	Percentage
°	Degree
0 D	Zero dimensional
1 D	One dimensional
2 D	Two dimensional
3 D	Three dimensional
Å	Angstrom
AC	Alternative Current
ACF	Auto correlation function
AFM	Atomic Force Microscope
$BaSO_4$	Barium sulfate
BSE	back scatter electrons
C	Capacitance
C_0	vacuum capacitance
CoO	Cobalt oxide
CTAB	Cetyltrimethyl ammonium bromide
$Cu(NO_3)_2$	Copper nitrate
CuO	Copper oxide
D	Crystallite Size
DLS	Dynamic Light Scattering
E_ω	Frequency dependent potential
E_g	Energy gap
EG	Ethylene Glycol
EIS	Electrochemical impedance spectroscopy
F	Fahrenheit
f	frequency
Fig.	Figure
FTIR	Fourier transform of Infrared
FWHM	Full width at half maximum
GB	Giga Bytes
HOMO	Highest Occupied Molecular Orbital
Hrs	Hours
Hz	Hertz
I_ω	Frequency dependent current
K	Kelvin
LUMO	Lowest Unoccupied Molecular Orbital

MgO	Magnesium oxide
MHz	Mega Hertz
MRAM	Magneto resistive Random Access Memory
NaOH	Sodium Hydroxide
NCRT	Negative coefficient of Resistance and temperature
NiO	Nickel Oxide
nm	nanometer
OER	oxygen evolution reaction
PCS	Photon Correlation Spectroscopy
PEG	Poly Ethylene Glycol
PSD	Particle size distribution
PVP	Polyvinyl Pyrrolidine
R	Reflection coefficient
RuO_2	Ruthedium Oxide
SE	Secondary electrons
SED	Secondary electron detector
SEM	Scanning electron microscope
STM	Tunneling Microscope
TiO_2	Titanium Oxide
UV	Ultra Violet
Vs	Versus
XRD	X-ray diffraction
Z'	Real part of impedance
Z''	Imaginary part of impedance
α	Alpha
ε''	the imaginary or dielectric loss.
ε'	the real or relative permittivity or dielectric constant
ε_0	permittivity of free space
μS	micro seconds
σ_{ac}	AC conductivity
σ_{dc}	DC conductivity
λ	wave length
τ	Relaxation time

CHAPTER I
INTRODUCTION TO NANOMATERIALS

1.1 Classification of materials

Solid materials can be broadly classified as crystalline and amorphous. In crystalline materials, the atoms are arranged periodically, whereas in amorphous there is no periodicity. Crystalline materials are further classified as single crystalline and polycrystalline materials. In single crystal, orientation of atoms exists in one direction. But the periodicity of atoms in polycrystalline is limited only inside some grains; usually the grain size is in micrometer. The materials which have the grain size in nanometer are known as nanomaterials. A nanocrystalline (NC) material is a polycrystalline material with a crystallite size of only a few nanometers. These materials fill the gap between amorphous materials without any long range order and conventional coarse-grained materials. Nanoscience and nanotechnology pertain to the synthesis, characterization, exploration, interrogation, exploitation, and utilization of nanostructured materials. Nanoscale materials are defined as a set of substances where at least one dimension is typically ranging from sub nanometers to several hundred nanometers. So nanotechnology is the ability to manipulate molecules and atoms to create structures, which may be used in the real world.

1.2 Nano scale

'Nano' derives from the Greek word "nanos", which means dwarf or extremely small. In the International System of Units, the prefix "nano" means one-billionth, or 10^{-9}; therefore one nanometer is one-billionth of a meter. It's difficult to imagine just how small that is, so here are some examples:

- A sheet of paper is about 100,000 nanometers thick
- A strand of human DNA is 2.5 nanometers in diameter
- There are 25,400,000 nanometers in one inch

- A human hair is approximately 80,000- 100,000 nanometers wide
- A single gold atom is about a third of a nanometer in diameter
- On a comparative scale, if the diameter of a marble is one nanometer, then diameter of the Earth would be about one meter
- One nanometer is about as long as your fingernail grows in one second

Fig. 1.1 compares the nanofibres with the human hair and helps us to understand how small nano is. It is recognized that the size range that provides the greatest potential and, hence, the greatest interest is that below 100 nm; however, there are still many applications for which larger particles can provide properties of great interest. Therefore, for the purposes of this article, it can have arbitrarily taken nanoparticles to be discrete particles that have a diameter of 250 nm or less [Pitkethly 2004].

1.3 Big thing behind the small scale

In nanomaterials atoms at the surfaces have fewer neighbours than the atoms in the bulk. Because of this lower co-ordination and unsatisfied bonds, surface atoms are less stabilized than bulk atoms. The smaller the particle, the larger is the fraction of atoms at the surface, and the higher is the average binding energy per atom. A simple thought experiment shows why nanoparticles have phenomenally high surface areas illustrated in Fig. 1.2. A solid cube of a material one centimeter on a side has six square centimeters of surface area, about equal to one side of half a stick of gum. But if that volume of one cubic centimeter were filled with cubes one millimeter on a side, that would be 1,000 millimeter-sized cubes (10 x 10 x 10), each one of which has a surface area of 6 square millimeters, for a total surface area of 60 square centimeters about the same as one side of two-thirds of a 3" x 5" note card. When the one cubic centimeter is filled with micrometer-sized cubes, a trillion (10^{12}) of them, each with a surface area of 6 square micrometers the total surface area amounts to 6 square meters, or about the area of the main bathroom in an average house.

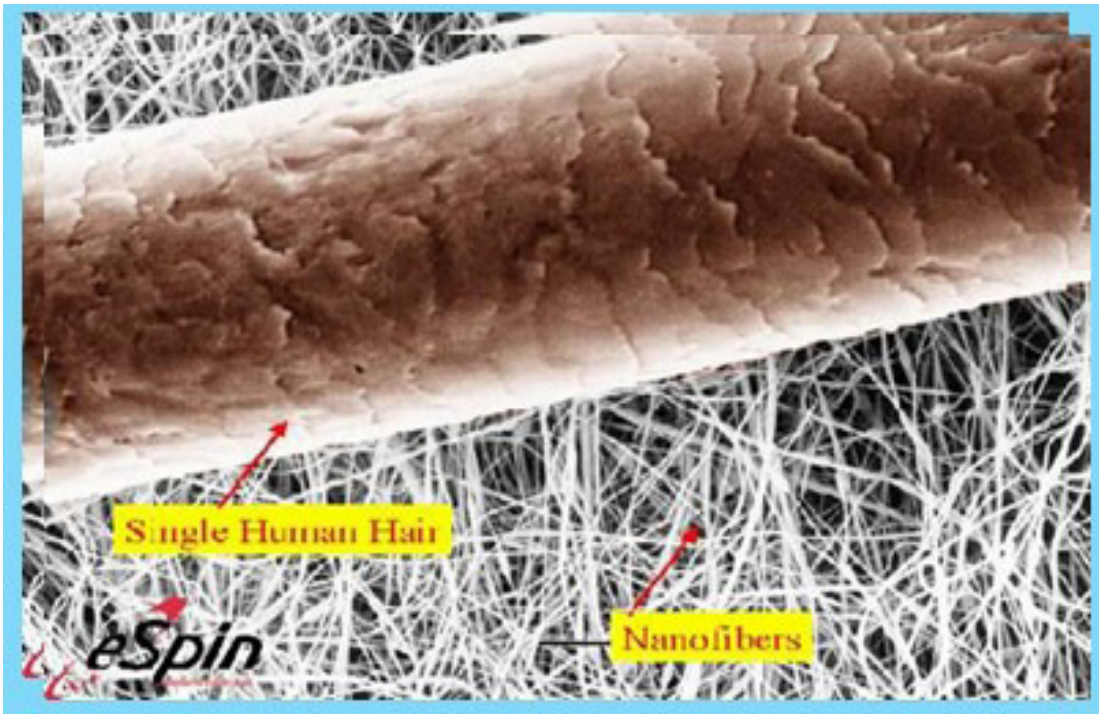

Figure 1.1: SEM image of human hair and nanofibers

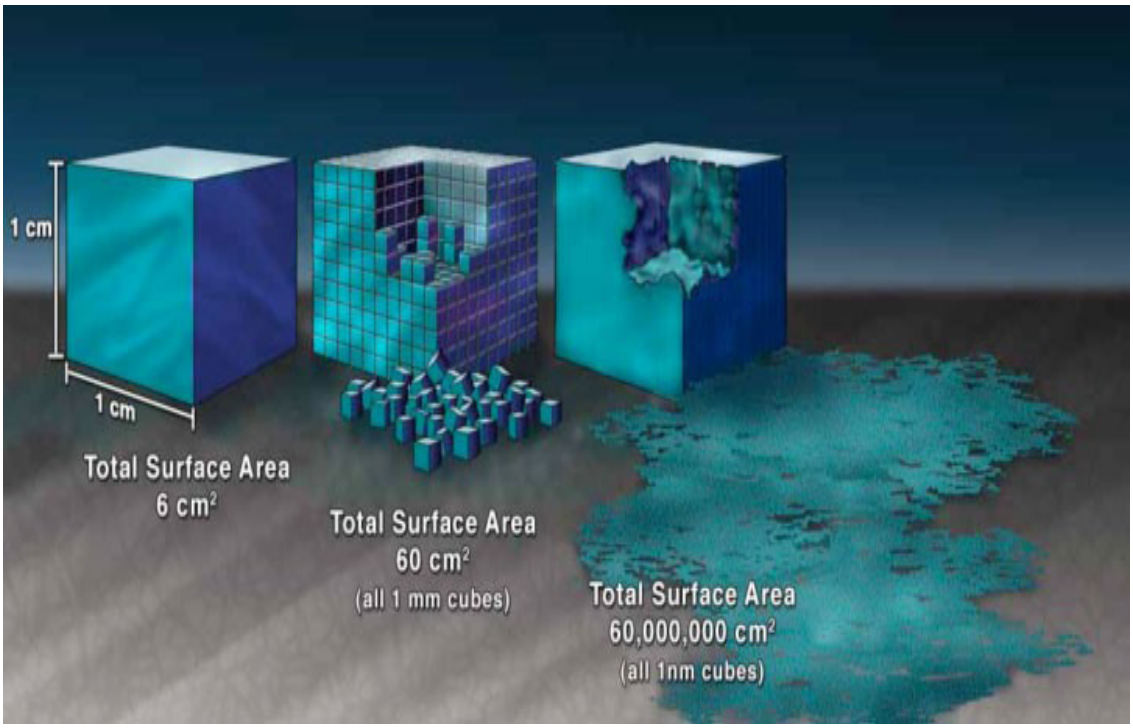

Figure 1.2: Simple example shows why nanoparticles have high surface areas

And when that single cubic centimeter of volume is filled with one nanometer sized cubes 10^{21} of them, each with an area of 6 square nanometers their total surface area comes to 6,000 square meters. In other words, a single cubic centimeter of cubic nanoparticles has a total surface area one-third larger than a football field.

The surface to volume ratio scales with the inverse size, and therefore there are numerous properties which obey the same scaling law. Among them are the melting and other phase transition temperatures. Edge and corner atoms have an even lower coordination and bind foreign atoms and molecules more tightly. Solubility of salts in pore-confined water, the melting point and even the critical point of a fluid are therefore greatly reduced. Phase transitions are collective phenomena. With fewer atoms a phase transition is less well defined, it is therefore no longer sharp. The Gibbs phase rule loses its meaning because phases and components are no longer properly distinguishable. Small clusters behave more like molecules than as bulk matter. It is therefore useful to think of different isomers which coexist over a temperature range rather than of different phases. There are numerous other concepts of thermodynamics which can break down, in particular when the system of interest consists of a single isolated cluster with a small number of atoms.

1.4. Quantum size effects

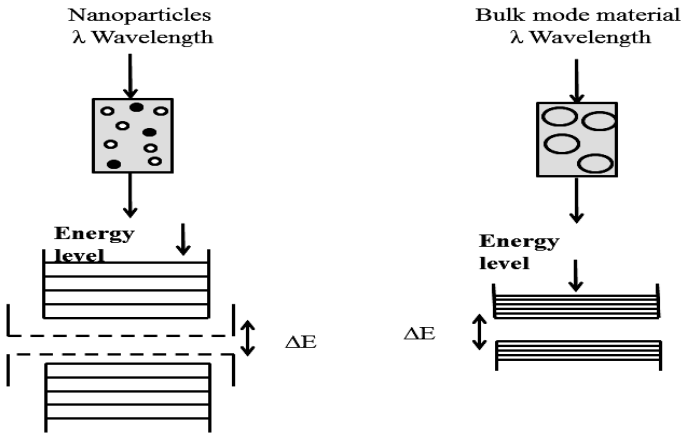

Figure 1.3: Comparison of energy levels between the nano and bulk materials

When a bulk matter is reduced to submicron size, electrons tend to accumulate onto the surface of the matter and these will cause changes in their properties, which are known as the quantum size effect. Due to this, the energy levels become discrete in nanomaterials similar to atoms as compared to continuous energy levels in bulk materials. In the case of semiconductor nanomaterials, the band gap energy increases when exciton (a bound electron-hole pair produced by a photon) is confined to a length scale comparable or smaller to its Bohr radius. These enhance the properties and hence promise a wider and better performance in applications as compared to their bulk entities. In metals and semiconductors the electronic wave functions of conduction electrons are delocalized over the entire particle. Electrons can therefore be described as 'particles in a box', and the densities of state and the energies of the particles depend crucially on the size of the box, which at first leads to a smooth size dependence [Emil 2006]. However, when more atoms are added the shells are filled up, and discontinuities occur when a new shell at higher energy starts to be populated. The HOMO–LUMO band gap of semiconductor particles and therefore their absorption and fluorescence wavelengths become size dependent. These same properties relate to the availability of electrons for forming bonds or getting involved in redox reactions. Therefore, the catalytic activity and selectivity become functions of size [Syed Amber Yousaf et al., 2008]

1.5. Nanotechnology not at all new

The interest in nanoscience is not all new. On December 29, 1959 at the California Institute of Technology, Nobel Laureate Richard P. Feynman gave a talk at the Annual Meeting of the American Physical Society that has become one of the 20th century's classic science lectures, entitled "There's Plenty of Room at the Bottom" [Feynman 1960].

Researchers have been studying the atomic properties of matter for more than a century, and fields like colloidal science have been extensively investigated in the last decades. In a sense, the study of atoms and molecules is the basis of most scientific disciplines, such as chemistry, biochemistry and physics are not all new. In recent year only researchers have been able to uncover enormous potentials of nanoscience and nanotechnology with the help of a new set of analytical and fabrication tools. In recent year only researchers have been able to uncover enormous potentials of nanoscience and nanotechnology with the help of a new set of analytical and fabrication tools. Some nano tools are not hat recent either for instance, Atomic Force Microscope (AFM) and the Scanning Tunneling Microscope (STM) techniques were first introduced to the science community in the mid-1980. Nano science is therefore an umbrella term that covers disciplines as well as new and emerging ones.

1.6. Why such scale of length is so of important?

In nanomaterials atoms at the surfaces have fewer neighbours than the atoms in the bulk atoms. The smaller a particle, the larger is the fraction of atoms at the surface, and the higher is the average. The increased surface to volume of nanomaterials impacts the material physical properties such as its melting and boiling points, as well as its chemical reactivity. Reactions that occur at the material surface are particularly affected such as catalysis reactions, detection reactions, and reactions that require the physical adsorption of certain species at the material's surface to initiate. Finally, the higher surface to volume of nanomaterials allows using less material, which has environmental and economic benefits, as well as fabricating highly miniaturized devices, which can be portable and could use less power to operate. Nanomaterials are of interest because at this scale unique optical, magnetic, electrical, and other properties emerge. These

emergent properties have the potential for great impacts in electronics, medicine, and other fields.

Five reasons are given below for why scale length is so important

1. Inside the matter the wavelike properties of electrons are influenced by changes on nanometer scale. It is possible to vary basic fundamental properties of materials by patterning matter on nanoscale without any variation in chemical composition.
2. On the nanometer length scale the systematic organization of materials is main feature of biological system. Nanotechnology promises to permit all of us to put or place art components as well as assemblies in to the cells and to produce the new materials by using self-assembled methods given by the nature. This gives us a new powerful combination of biotechnology and material science.
3. The nanoscale components are used in reacting systems, energy storage, composite materials and drug delivery because of its very richly surface field.
4. The materials with the scale of molecule i.e. finite size determines the main importance of local electromagnetic effect and surface tension which makes the material nano sized and it is less brittle & hard.
5. The nanomaterials make suitable for various applications in the field of optoelectronics.

1.7. Classification of Nanomaterials

On the basis of geometry the nanomaterials are classified into four types as:

1. Zero-dimensional (0 D)

Zero-dimensional nanostructures are tiny particles that have quasi-zero dimension. Fullerenes, quantum-dots and dendrimers are the examples of 0 D nanostructures.

2. One-dimensional (1 D)

One-dimensional nanostructures have one dimension of the particulate in the nanometer scale and mainly comprises of nanosheets, nanoclays and nanolayers.

3. Two-dimensional (2 D)

Two-dimensional nanostructures have two dimensions of particulate in nanometer scale and third dimension is in micro or macro scale. These materials form an elongated structure and comprise of nanotubes, nanorods and nanofibers.

4. Three-dimensional (3D)

The structures having all three dimensions of particulate in nanometer scale are called as three dimensional structures. They are generally comprises of nanoparticles, nanocrystals and nanogranule. They exist in single, fused, aggregated or agglomerated forms with spherical, tubular and irregular shapes.

1.8 Applications of Nanomaterials

1.8.1. Fabrics

- Making composite fabric with nano-sized particles or fibers allows improvement of fabric properties without a significant increase in weight, thickness, or stiffness as might have been the case with previously-used techniques. For example incorporating nanowhiskers into fabric used to make pants produces a lightweight water and stain repellent material.

- Nano whiskers that cause water to bead up, making the fabric water and stain resistant.
- Silver nanoparticles in fabric that kills bacteria making clothing odor- resistant.
- Nano pores providing superior insulation for shoe inserts in cold weather.
- Nano particles that provide a "lotus plant" effect for fabric used to remove dirt to rinse off in the rain.

1.8.2. Drug Delivery

One application of nanotechnology in medicine currently being developed involves employing nanoparticles to deliver drugs, heat, light or other substances to specific types of cells (such as cancer cells). Particles are engineered so that they are attracted to diseased cells, which allow direct treatment of those cells. This technique reduces damage to healthy cells in the body and allows for earlier detection of disease.

1.8.3. Strength of materials

Nano-sized particles of carbon, (for example nanotubes and balls) are extremely strong. Nanotubes and balls are composed of only carbon and their strength comes from special characteristics of the bonds between carbon atoms. One proposed application that illustrates the strength of nano sized particles of carbon is the manufacture of T-shirt weight bullet proof vests made out of carbon nanotubes.

1.8.4. Nano electronics

- Making integrated circuits with features that can be measured in nanometers (nm), such as the process that allows the production of integrated circuits with 22 nm wide transistor gates.

- Using nano sized magnetic rings to make Magnetoresistive Random Access Memory (MRAM) which research has indicated may allow memory density of 400 GB per square inch.
- Developing molecular-sized transistors which may allow us to shrink the width of transistor gates to approximately one nm which will significantly increase transistor density in integrated circuits.
- Using magnetic quantum dots in spintronic semiconductor devices. Spintronic devices are expected to be significantly higher density and lower power consumption because they measure the spin of electronics to determine a 1 or 0, rather than measuring groups of electronics as done in current semiconductor devices.
- Using silver nanowires embedded in a polymer to make conductive layers that can flex, without damaging the conductor.
- Researchers have developed organic nano glue that forms a nanometer thick film between a computer chip and a heat sink. They report that using this nano glue significantly increases the thermal conductance between the computer chip and the heat sink, which could help keep computer chips and other components cool.
- Silver nanoparticle ink was used to form the conductive lines needed in circuit boards.

1.8.5. Applications in Space

Nanotechnology may hold the key to making space flight more practical. Advancements in nanomaterials make lightweight solar sails and a cable for the space elevator possible. By significantly reducing the amount of rocket fuel required, these advances could lower the cost of reaching orbit and traveling in space. In addition, new materials combined with nanosensors and nanorobots could improve the performance of

spaceships, spacesuits, and the equipment used to explore planets and moons, making nanotechnology an important part of the 'final frontier.

1.8.6. Fuel cells

Catalysts are used with fuels such as hydrogen or methanol to produce hydrogen ions. Platinum, which is very expensive, is the catalyst typically used in this process. Companies are using nanoparticles of platinum to reduce the amount of platinum needed, or using nanoparticles of other materials to replace platinum entirely and thereby lower costs. Fuel cells contain membranes that allow hydrogen ions to pass through the cell but do not allow other atoms or ions, such as oxygen, to pass through. Companies are using nanotechnology to create more efficient membranes; this will allow them to build lighter weight and longer lasting fuel cells.

1.8.7. Solar cells

Using nanoparticles in the manufacture of solar cells has the following benefits: Reduced manufacturing costs as a result of using a low temperature process similar to printing instead of the high temperature vacuum deposition process typically used to produce conventional cells made with crystalline semiconductor material.

- Reduced installation costs achieved by producing flexible rolls instead of rigid crystalline panels. Cells made from semiconductor thin films will also have these characteristics.
- In the long term nanotechnology versions should both be lower cost and, using quantum dots, should be able to reach higher efficiency levels than conventional ones.

1.8.8. Batteries

- Reducing the possibility of batteries catching fire by providing less flammable electrode material.
- Increasing the available power from a battery and decreasing the time required to recharge a battery. These benefits are achieved by coating the surface of an electrode with nanoparticles. This increases the surface area of the electrode thereby allowing more current to flow between the electrode and the chemicals inside the battery. This technique could increase the efficiency of hybrid vehicles by significantly reducing the weight of the batteries needed to provide adequate power.
- Increasing the shelf life of a battery by using nanomaterials to separate liquids in the battery from the solid electrodes when there is no draw on the battery. This separation prevents the low level discharge that occurs in a conventional battery, which increases the shelf life of the battery dramatically.

1.8.9 Pollution control

There are two major ways in which nanotechnology is being used to reduce air pollution: catalysts, which are currently in use and constantly being improved upon nano-structured membranes, which are under development.

- Catalysts can be used to enable a chemical reaction (which changes one type of molecule to another) at lower temperatures or make the reaction more effective. Nanotechnology can improve the performance and cost of catalysts used to transform vapors escaping from cars or industrial plants into harmless gasses. That's because catalysts made from nanoparticles have a greater surface area to interact with the reacting chemicals than catalysts made from larger particles. The

larger surface area allows more chemicals to interact with the catalyst simultaneously, which makes the catalyst more effective.

- Another challenge is the removal of salt or metals from water. A deionization method using electrodes composed of nano-sized fibers shows promise for reducing the cost and energy requirements of turning salt water into drinking water.

1.8.10 Chemical sensor

Nanotechnology can enable sensors to detect very small amounts of chemical vapors. Various types of detecting elements, such as carbon nanotubes, zinc oxide nanowires or palladium nanoparticles can be used in nanotechnology-based sensors. These detecting elements change their electrical characteristics, such as resistance or capacitance, when they absorb a gas molecule. Because of the small size of nanotubes, nanowires, or nanoparticles, a few gas molecules are sufficient to change the electrical properties of the sensing elements. This allows the detection of a very low concentration of chemical vapors. The goal is to have small, inexpensive sensors that can sniff out chemicals just as dogs are used in airports to smell the vapors given off by explosives or drugs. These sensors can also be useful in industrial plants that use chemicals in manufacturing to detect the release of chemical vapours.

[www.mod.uk/linked_files/nanotech.pdf]

CHAPTER II

AIM AND LITERATURE SURVEY

2.1. Formulation of the Problem

Our water resources contaminated with the waste water released by many industries like textile industry, leather industries, hair-coloring industries, food industries and paper industries. More than ten thousand different commercial dyes and pigments exist and 7, 000, 00 tons are produced per year worldwide [Wanchanthuek et al., 2001]. Based on their chemical structure dyes are classified into number of categories like Anthraquinones, Azo, Natural, Thiazines, Triarylmethanes, Xanthenes and so on. During the processing in the industries said above, the excess dyes are making to mix up with the water resources and pollute the water. The harmfulness of the dyes crafted the stipulation to execute the removal process. There are number of methods to remove the organic dye pollutants like chemical oxidation, solvent extraction, catalytic degradation and biodegradation. Photocatalytic degradation is known as one of the cost effective as well as safe and sound method. Thus the need to degrade the different contaminant dyes paved the way for study the photo catalytic degradation of dyes.

On the basis of SciFinder data source [Malka Rochkind et al., 2015] reported in his review paper, that the production of azo group of dyes is 50% to 70% of the total dye production in global however the manuscripts on the removal of azo dyes in the presence of visible light are little. Metal oxides such as CuO, CoO, NiO, TiO_2, and RuO_2 have been proved as potential catalysts by many researchers. Drawback of these materials is their absorbance range lies in UV region. So designing a photo catalyst with the utilization of solar energy is considered as one of the most promising and clean approaches towards pollutant removal from aquatic environments. For this objective

scientific fields require materials with the absorption in visible region of the light. CuO studied as photocatalyst both in UV and visible region by many researchers [Huxia Shi et al., 2012, Kebin Zhouet al., 2006, Qingwei Zhu et al., 2011, Yu Li et al., 2010, Nillohit Mukherjee et al., 2011, Xueqin Liu et al., 2012, Behrouz Shaabani et al., 2014]. But the capability of the materials depends on experimental conditions and morphology of the materials. Lu et al suggest that optical absorption is often affected by the morphology of the crystals [Lu et al., 2005] and Pallavi Amet et al., suggest that absorbance wavelength range of coloured oxides can be expandable into visible region. [Pallavi Amet et al., 2010]

On the other hand, main concerns in the materials selection for supercapacitor electrodes are C_S, specific capacity and abundance for large scale production. Cobalt oxide (Co_3O_4) has large practical C_S (3560 Fg^{-1}) [Yang et al., 2014] but they are relatively lower abundant (<20 ppm) in the earth crust. On the other hand, materials such as MnO_2 with theoretical C_S (1370 Fg^{-1}) are largely abundant (>2000 ppm) but their practical C_S are relatively lower (<400 Fg^{-1}) [He et al., 2014, Yuan et al., 2014]. Therefore, materials of high abundance and large practical Specific capacity (C_S) are inevitable for fabrication of high performance commercial devices. Copper oxide (CuO) nanostructures gained considerable attention recently owing to its lower toxicity, relatively larger abundance environmental stability, and desirable electrochemical properties [Zhang et al., 2014]. Table 1 shows the survey on the supercapacitors using CuO electrodes.

2.2 Properties of Copper oxide (CuO)

Cupric oxide (CuO), a p-type semiconductor with a narrow band gap (1.2 eV in bulk) has been a hot topic among the studies on transition MOs due to its fascinating properties such that low band-gap energy, earth-abundant, high optical absorption, high

catalytic activity, reusability, nontoxic nature, and low-cost and promising applications [Zhou et al., 2016, Azar Sadollahkhania et al., 2014]. Among group I B elements, copper is the only element, obtained as oxide, rather as a perfect metal. It is an important covalent p-type semiconductor metal oxide. Oxygen atoms situated at the corners of a rectangular parallelogram, which forms chains by sharing.

Chemical formula	:	CuO
Molar mass	:	79.545 g/ mol
Appearance	:	Black to brown powder
Density	:	6.315 g/ cm^3
Melting point	:	1,326 °C (2,419 °F; 1,599 K)
Boiling point	:	2,000 °C (3,630 °F; 2,270 K)
Solubility	:	insoluble in water, alcohol, ammonium hydroxide
Solubility	:	insoluble in ammonium chloride, potassium cyanide
Band gap	:	1.2 eV (Bulk)
Refractive index	:	2.63
Crystal structure	:	monoclinic
Space group	:	C2/c
Flammability	:	non flammable
Chemical composition:		79.89 % of copper and 20.10 % of Oxygen
Magnetism	:	ferromagnetism

2.3 Literature survey on the morphology of CuO and surfactants used

Considering the above said, we are synthesized Copper oxide nanostructures and their sunlight driven photocatalyst properties and CV studies were discussed. A number of literatures discusses about synthesis of different morphology of CuO like nanorods, nanoribbons [Yu Ch & Hua Ch 2004], nano plates [Yueming et al., 2008], nanosheets

[Jiang et al., 2009], octahedran, sphere, strip, Dandelion [Qingwei et al., 2011, Wang et al., 2007], Cacoon shaped [Kim et al., 2015], nanowires, nano belts [Du et al., 2004], flower like [Junwu et al., 2007], Gear-like [Liutao et al., 2013] nano cubes and leaf like [Hafsa et al., 2016], peach kernel-like [Chuanyue et al., 2013] structures.

Morphology can be changed by changing pH, temperature, precursor materials, reaction conditions, preparation methods and surfactants. Surfactant is nothing but the surface reducing agents. They reduce the surface energy and control the agglomeration and thus control the particle size. Some surfactants can also acts as template (structure directing agents) and create morphology of the materials in suitable experimental conditions. Number of surfactants have been used in literatures to synthesize copper oxide materials PEG (Poly Ethylene glycol) [Minhua et al., 2004], PVA (polyvinyl alcohol) [Vijaya Kumar et al., 2001], Chitosan [Chuanyue et al 2013], SDS (sodium Dodecylsulfate), Triton X-100 [Nishtar et al., 2008], CTAB (Cetyl trimethyl-ammonium Bromide) [Zhongli & Hongdong 2015], Amino acids [Razium Ali et al., 2015], starch [Suramwar et al., 2012], glycerol [Ayekpam et al., 2014] and so on.

2.4. Survey on the various method of synthesis

Numerous methods have been recently developed to synthesize various CuO nanostructures with diverse morphologies, sizes, and dimensions using various chemical and physical strategies.

2.4.1. Sol gel method

Two major sets of reactions takes place during synthesis by sol–gel process: (i) hydrolysis of the precursor and (ii) poly condensation of the hydrolyzed products. Sol-gel process consists in the chemical transformation of a liquid (the sol) into a gel state and with subsequent post-treatment and transition into solid oxide material. Metal

salts dissolved in aqueous or organic solvents and stabilized by chelating ligands. The introduction of water into the system initiates hydrolysis. Chelating agent given the 3D network. After drying, the gel is heated to initiate pyrolysis of the organic species, resulting in agglomerated submicron oxide particle. Citric acid and acetic acid were used `as chelating agents. [Vahidshad et al., 2011, Mallick et al., 2012, Prakash Chand et al., 2011]

2.4.2. Hydrothermal method

Stoichiometric amount of precursor salt solution was transferred into a Teflon-lined stainless steel autoclave and sealed tightly. Thermal treatment was carried out at particular temperature for a period of time in an auto controlled oven. Then the autoclave was allowed to cool naturally. The precipitate was washed and dried and calcined in a vacuum. Urea [Yange Zhang et al., 2006], reducing agent [Hao-Wen et al., 2015] and surfactants [Jingang Zhao et al., 2015] can also be mixed with the precursor solution before enter into the autoclave.

2.4.3. Combustion method

Combustion synthesis provides a localized energy supply by self-generated heat for synthesis, which eliminates the continuous need for high, externally applied processing temperature to drive the reaction. [Christy et al., 2013] Stoichiometric amount of cupric nitrate was dissolved in deionized water and then citric acid was added into it. The solution was kept in the furnace at 300 °C. Initially, the solution boils and undergoes dehydration followed by decomposition with the evolution of large amount of gasses. After the solution reached the point of spontaneous combustion, it began to burn and released much heat, vaporizing the entire solution instantly. With large amount of fumes produced the combustion and gases of CO_2, H_2O and N_2 can be formed directly from the

reaction between fuel and oxidizer without the necessity of getting oxygen from outside. As a result, CuO product of loose powder was formed which was crushed and ground thoroughly. Citric acid is oxidized by nitrate and serves as fuel [Jegatha Christy et al., 2013] Combustion reaction can also be done using different fuels glycine [Guo et al., 2010], urea [Hamed Sadabadi et al., 2015].

2.4.4. Reflection condensation method

A mixture of reactants and solvent is placed in a suitable vessel, such as a round bottom flask. This vessel is connected to a water-cooled condenser, which is typically open to the atmosphere at the top. The reaction vessel is heated in order to boil the reaction mixture; vapours produced from the mixture are condensed by the condenser, and return to the vessel through gravity. The purpose is to thermally accelerate the reaction by conducting it at an elevated, controlled temperature (i.e. the solvent's boiling point) and ambient pressure. After the reaction, the system was cooled naturally to room temperature. Precipitates were collected by centrifugation and washed several times with deionized water and ethanol. The resulting precipitates were dried and calcined. [Mageshwari et al., 2015] reported the reflux condensation method using copper nitrate and ammonium hydroxide. Du et al introduced a block polymer P123 with the precursor and reducing agents and synthesized the CuO by the reflux condensation method [Xiaoqiang Du et al., 2016]. Ethylenediamine ($C_2H_8N_2$) (structure-directing agents) was used in the refluxing method by [Kim et al., 2015] to synthesize Cacoon shaped CuO nanomaterial.

2.4.5. Co- precipitation method

In this course of work, CuO nanostructures were fabricated via soft chemical method briefly, suitable molar ratios precursor salts were dissolved in distilled water as

added to these solutions as a surfactant. After complete dissolution of precursors, NaOH (1M solution) was added drop wise to adjust the pH value. After adjusting the pH values, the solutions were stirred for one hour with or without temperature to complete the reactions. The precipitates were then collected, washed and dried in electric oven. Finally, the dried precipitates were grinded and annealed some high temperature for particular period of time in order to enhance the crystalline quality of the synthesized samples. Water soluble surfactants can be used in this method [Mahdi Shahmiri et al., 2013]. CuO nanostructures were synthesized by precipitation method using copper chloride ($CuCl_2$) and copper nitrate (Cu $(NO_3)_2.3H_2O$) by [Kankanit et al 2013].

2.4.6. Sonochemical synthesis

Sonochemistry is the application of ultrasound to chemical reactions and processes. The mechanism causing sonochemical effects in liquids is the phenomenon of acoustic cavitation. A solution is made with stoichiometric amount of precursor salts, reducing agents and solvents. Sonication of the solution was performed by a sonicater until the completely precipitated product was reached. Finally, the as-precipitated powders were calcined at different temperature range [Kumar et al., 2000, Narongdet et al., 2011 performed the sonication of the copper nitrate and NaOH in the presence of polyvinyl alcohol surfactant. Synthesis of copper oxide by the sonication of Copper acetate and urea solution with temperature was reported by the [Chonghai Deng et al., 2011]

2.4.7. Thermal oxidation

Thermal oxidation of pristine copper was carried out in muffle furnace Copper metal powder (99.99 %) purity, was used as the starting material. The copper powder was loaded into the crucible, which was then placed in a conventional muffle furnace for

thermal oxidation under open conditions and higher temperatures. After heating, the copper powder gets converted into gray/black material that was collected and stored for further characterization. Here the powder can be treated with any surfactants [Uma Nerle & Rabina 2013] reported the (EDTA and amine treated copper powder grinded with surfactants) thermal oxidation of copper to synthesis of copper oxide.

2.4.8. Solid state reaction method

The solid-state reaction route is the most widely used method for the preparation of polycrystalline solids from a mixture of solid starting materials. The selection of reactant chemicals depends on the reaction conditions and expected nature of the product. After the reactants have been weighed out in the required amounts, they are mixed. For manual mixing of small quantities, usually an agate mortar and pestle are employed. Sufficient amount of some volatile organic liquid preferably acetone or alcohol is added to the mixture to aid homogenization. This forms a paste which is mixed thoroughly. For the subsequent reaction at high temperatures, paste is kept in oven in a container which is chemically inert to the reactants under the heating conditions used. Copper precursor salt and NaOH in a 1: 2 molar ratio were mixed and ground in an agate mortar in order to get the best possible homogeneity. The color of the mixture immediately transferred from sky-blue to dark at room temperature after 20 min [Jia Dianzeng et al.,1998] surfactants assistant method can be employed by grinding the effective surfactant with the precursor [Wang et al., 2001]

2.4.9. Microwave irradiation

Conventional heating usually involves the use of a furnace or oil bath, which heats the walls of the reactor by convection or conduction. Acting as internal heat source, microwave absorption is able to heat the target compounds without heating the entire

furnace or oil bath, which saves time and energy. It is also able to heat sufficiently thin objects throughout their volume (instead of through its outer surface), in theory producing more uniform heating. Different compounds convert microwave radiation to heat by different amounts. This selectivity allows some parts of the object being heated to heat more quickly or more slowly than others (particularly the reaction vessel).

Stoichiometric amount mixture of precursor salt reducing agent, surfactant and solvent was placed in a domestic microwave oven and irradiation was carried at particular percentage of power time. The solution mixture boils in about 10 seconds of microwave irradiation. Therefore, it was cooled in an ice bath after every 10 seconds and heating was continued till the dark-green precipitate was formed at the end of the reaction. After cooling to room temperature the precipitate was centrifuged, washed with de-ionized water repeatedly and finally with absolute ethanol, dried in a hot air oven [Felix et al., 2015]. It is found to be a fast, convenient, mild, energy-efficient and environmentally friendly route to produce CuO nanoparticles in only one step [Hui wang et al., 2002].

2.5. Survey on the applications of CuO nanomaterials

2.5.1. Fuel cell (Electro catalyst)

With the increase demand for clean fuel and consciousness of environmental issues, the use of hydrogen (H_2) gas as a clean, efficient and portable fuel has become one of the attractive alternatives for energy consumption. Therefore, there is a great need to develop a more active, efficient, stable, and cheap electro catalysts for water splitting that would offer low over potentials for the hydrogen and oxygen evolution reactions. The oxygen evolution reaction (OER) on oxide surfaces is in the focus of electrochemical research for more than three decades mainly because it is the main source of over potential in the industrial water electrolysis. There is an extensive work in

the literature addressing the development and characterization of suitable anodic materials for the applications in water electrolysis and batteries technology. As alternative to precious metals, metal oxide-based electrodes, particularly Ni and Co oxides, have long been used as electrocatalysts for the OER in alkaline electrolyzers due to their great stability and high activity [Tao Hong et al., 2016, Yuanyuan et al., 2015]

2.5.2. Photocatalytic applications

Organic dyes are extensively used for various industrial applications including textile dyeing, photographic, coating and photochemical industries. Most of the dyes used as coloring materials are toxic to aquatic organisms. The pollutants can be effectively removed from wastewater by the photocatalytic process using semiconductor photocatalysts. Among several metal oxides, CuO is one of the suitable photocatalysts for this purpose, because of its photocatalytic activity, reusability, nontoxicity and other properties. It is used to degrade many dyes and chemicals.

2.5.3. Lithium ion Battery electrodes

Lithium-ion batteries (LIBs) are currently the dominant power sources for portable appliances such as mobile phones and notebook computers. In order to meet the increasing demand in high energy density of LIBs that could be employed in vehicles and next generation of portable electronic devices, the exploration of new electrode materials of superior rate capacity and higher safety is a key issue in LIB development. The copper oxide among transition-metal oxides is of particular interest for its huge specific capacity, inexpensiveness and nontoxicity [ke et al., 2009]. Morales and coworkers have prepared nanostructured CuO thin films by spray-pyrolysis method, and found that the nanostructured CuO electrodes could deliver a reversible capacity as high as 625 mAh g^{-1} up to 100 cycles [Morales et al., 2005]. Chen et al. demonstrated that the

electrode of CuO with dandelion-like hollow microspheres could release a reversible capacity more than 600 mAh g^{-1} up to 50 cycles [Guanhua Chen et al., 1989].

2.5.4. Supercapacitors

Electrochemical capacitors, also known as supercapacitors (SCs) or ultra capacitors are promising energy storage systems as they bridge the gap between traditional dielectric capacitors and chemical batteries. Supercapacitors are particularly useful in applications requiring fast charge/discharge rates such as power backup for electronic devices, cell phone cameras, regenerative braking and hybrid electric vehicles. Metal oxides often exhibit higher specific capacitances and electrochemical stability than most conductive polymers, so they are preferred electrode materials for building high-energy supercapacitors. Copper oxide (CuO) is a promising candidate due to its, easy preparation in various shapes at the nanoscale and good electrochemical performance. For example, Wang et al., 2001 synthesized nanosheet arrays of CuO on nickel foam with a high specific capacitance of 569 F/g in KOH electrolyte; however, the method employed is relatively complex and the yield is quite low. 3D porous gear-like CuO has been reported on a Cu substrate with the specific capacitance of 348 F/ g.

2.5.5. Bio sensors (glucose sensors)

Accurate and rapid determination of glucose is important in various areas such as biotechnology, clinical diagnostics and the food industry. In recent years, the development of electrochemical glucose sensor has attracted much attention, significantly developing some non-enzymatic glucose sensors to solve the problems of the enzyme electrodes such that the (1) the lack of stability due to the intrinsic nature of the enzymes; (2) the lack of simplicity and reproducibility due to the difficulty of the method for enzyme immobilization and (3) the cost and susceptibility In addition, the

high cost of the electrode materials might limit their commercial applications, since the ability to produce glucose sensors in large numbers at low cost is a major market requirement. Nanostructured CuO is promising in the development of nonenzymatic glucose sensor because of its highly specific surface area and good electrochemical activity [Zhang et al., 2012, Wang X et al., 2010]

2.5.6. Antimicrobial activities (Cytotoxicity)

Copper oxide nanoparticles appeared to have greater cytotoxicity compared to their bulk counterpart and to other metal oxides nanoparticles. Copper ions released by the nanoparticles may attach to the negatively charged bacterial cell wall and rupture it, thereby leading to protein denaturation and cell death. Copper ions inside the bacterial cells may bind to deoxyribonucleic acid molecules and become involved in cross-linking within and between the nucleic acid strands, resulting in the disorganized helical structure. In addition, copper ion uptake by the bacterial cells has also been found to damage important biochemical processes, there by leading to an overall diminishing in their growth rate. [Oberdo rster et al., 2005, Sun T et al., 2012, Ren et al., 2009]

2.5.7. Gas sensors

Air pollution problems are drawing more and more people's attention with the development of the modern industry. Gas sensors that can detect a variety of volatile organic gases (VOCs) or toxic gases are of great importance. Metal oxide semiconductor gas sensor have attracted people's attention because of its high sensitivity, low manufacturing cost and simple means of measurement and signal characteristics. But most commercial products still use sensing materials based on SnO_2, WO_3 and ZnO which are n-type semiconductors, for VOCs or toxic gas detection. When exposed to reducing VOCs, the bulk resistance of n-type semiconductor oxide gas sensor is reduced,

while a p-type semiconductor oxide gas sensor bulk resistance becomes larger. Therefore, it is very important to study the p-type oxide semiconductor gas sensing device. However, the research on the p-type oxide semiconductor gas sensor is less. Cupric oxide (CuO) is one of the most important p-type oxide semiconductors as it exhibits a stable narrow band gap (1.2-1.9 eV). Nano CuO and its composite oxides have potential applications in the field of sensor because of their large surface-area-to-volume ratio. Various nanostructured CuO materials, Low operating temperature, a cost effective option, offers stability to the active sensing materials and becomes an automatic choice for sensing application. [Yueming Li et al., 2008, Das et al., 2013, Sergiu et al., 2006]

2.5.8. Anticancer agent

The anticancer activity of CuO had reported by the report they said that nanostructures depends on the level of reactive oxygen species (ROS) production which is dependent on the presence of defects sites in the metal oxide crystal structure. The white light can generate electron hole pair in CuO by exciting the valance band electrons to conduction band. These holes in the valance band are migrated to the surface of the nanostructures and interacted with water molecules which lead to generate hydroxyl radicals (OH). On the other hand, the photo-generated electrons are reached the surface which interacts with adsorbed oxygen molecules to form oxygen radicals after interacting with H^+ ions and generate H_2O_2. These free radicals induce damage to the cellular components like DNA, lipids and proteins of the cancer cells and cause their death through apoptosis [Tariq Jan et al., 2015]

2.5.9. Solar cell observers

In the context of the developing of energy saving technologies, much attention has been devoted to the selective absorbers of electromagnetic radiation and the related

alternative energy sources, in particular, to thermal converters of solar energy, which employ coatings based on such selective absorbers. The selective solar energy absorbers must obey certain requirements. These materials should possess a large absorption coefficient (α) and a small reflection coefficient (R) in the photon energies E > 0.5 eV, on the one hand, and exhibit low emission or high reflection in the IR spectral range at E < 0.5 eV. In other words, a selective monoabsorber (i.e., an absorber based on a single component) must exhibit a strong absorption of radiation of the given source at a minimum level of the energy reradiated to the atmosphere in the IR range. These conditions could be satisfied by solar energy absorbers with an optical gap width of Eg ~ 0.5 eV and a small refractive index n in the IR range. It was suggested to use various copper compounds as selective absorbers of solar energy operating at T < 500°C. [Sukhorukov et al., 2006]

2.5.10. Superconductors

Among the eight families of high-Tc superconductors, the copper oxides (Cuprates) stand out in their high Tc values, and are only family that achieved Tc well above the liquid nitrogen temperature. High-Tc superconductivity (HTS) in the cuprates was discovered by Bednorz and Müller in 1986. Adjacent Cu spins have a tendency to be opposite when separated by a normal 02- but tend to repolarize parallel (ferromagnetic) when separated by an oxygen hole (O^-). As the conduction electron (0- hole) moves from site to site, it tends to leave behind a wake where adjacent copper spins are ferromagnetically paired. As a second conduction electron is scattered, it is favorable to be scattered into the wake of the first electron, since there is already ferromagnetic polarization of the copper spins, leading to a favorable interaction. The net result is an attractive interaction between conduction electrons which leads to superconductivity. [Tranquada et al., 1995, Guanhua Chen et al., 1989].

Table 2.1: Survey on the supercapacitors using CuO electrodes.

S.No	Method	Morphology	Electrolyte	Voltage window	Specifi-capacitance (F/g)	Cell Configuration	Reference
1	Electro spun	nanowires	6M KOH	-1.2 to 0V	149	3E	BaijuVidyadharan et al., 2015
2	Hydrothermal method	Nano petals	Ionic liquids	-0.6 to 0.3 V	133	3E	Awale et al., 2016
3	Micro emulsion	leaf-like	2M KOH	0.1 V to 0.4 V	45.3	3E	Bello et al., 2014
4	One-pot water bath method	Nanoribbons Nanoflowers	6 M KOH	-0.1 – 0.6	132 120	3E	BojunHeng et al., 2013
5	CBD	Hierarchical nanosheets	1M Na_2SO_4	-0.1 – 0.6	411	3E	Dubaletal., 2013 (B)
6	CBD	Multilayer nanosheets	1 M Na_2SO_4	0.1 to 0.7 V	43	3E	Dubaletal., 2010
7	Potentiodynamic deposition	cauliflower	1 M Na_2SO_4	-0.6 – 0.2	179	3E	Dubaletal., 2013(A)
8	Chemical Precipitation	Flower Nanosheets globular	6M KOH	0 – 0.4	133.6 72.7 26.4	3E	Zhang H et al ., 2008
9	Wet Chemical	Sheet Bundle flower	6M KOH	0- 0.4	88.5 49.2 68	3E	Yu Xin Zhang et al., 2008

10	CuO from Cu Solution method	Nano rod plates Flowers	1 M Na_2SO_4	-0.6 - 0	72 145 158	3E	Momeni et al., 2014
11	Crystallaisation of Cu foil	hierarchical nanostructures	1 M Na_2SO_4	-0.8 – 0.1	94	3E	Krishna Moothyetal., 2013
12	Liquid solid reaction	Lotus like	5M NaOH		278	3E	Yu Kuei Hsuetal., 2012
13	Hard template	3D ordered nanoporous	3M KOH	0 – 1.4	431 72.4	3E 2E	SeyyedEbrahim et al., 2015
14	Hydrothermal method	Array of nano sheets	LipF6/EC/DCE	0 - 2	343	-	Honghong Nan etal 2014
15	Cathodic deposition	Cauliflower	1 M Na_2SO_4	-1 – 0	36	3E	Patakeetal., 2009
16	Oxidation	Nano flakes	1M KOH	-0.6 – 0	190	3E	Endutetal., 2013
17	Cathodic deposit	Granular	1 M Na_2SO_4	-0.7 – 0.1	62	3E	Ghadgeetal., 2015
18	Chemical synthesis	Hierarchical	1 M KOH	0 – 0.7	498	3E	Shindeetal., 2015
19	Template free growth	Nano sheet	KOH		569	3E	Guiling wangetal., 2011
20	Wet chemical method	3D Gear like	0.1 KOH	-0.5 – 0	348	3E	LiutaoYuetal., 2013
21	Chemical Precipitation	Nano sheets Nano flowers	6M KOH	0- 0.4	133.6 26.4	3E	HongxiaZhangetal., 2013

2.6 Formulation of the Materials and Methods

Numerous methods have been discussed in literature survey to synthesize various CuO nanostructures with diverse morphologies, sizes and dimensions using various chemical and physical strategies. In this work, we have prepared Cupric oxide nanostructures by wet chemical method. Since CuO is inexpensive material, we have chosen a cost effective and simple to synthesize the materials wet chemical method one which doesn't need any special equipment. Cupric nitrate tri hydrate [Cu $(NO_3)_2 \cdot 3H_2O$] (Himedia 99.5% purity and sodium hydroxide pellets [NaOH] (Nice chemicals) are the chemicals used in this experiment.

Wet chemical method of synthesis involves following steps: (i) Hydrolysis of Precursors (Copper nitrate solution and Sodium hydroxide solution) and adding of reducing agent (NaOH) until the particular pH level.

The reaction scheme is

$$Cu(NO_3)_2 + 2\,NaOH \rightarrow Cu(OH)_2 + NaNO_3 \quad \text{---------- (2.1)}$$

According to the eqn (2.1) the molar ratio of Cu $(NO_3)_2$ and NaOH is selected as 1:2 ratio. Synthesis of copper oxide have the possibility of producing three phases such that Cu $(OH)_2$, CuO, Cu_2O. We are interested to synthesis the most stable form CuO. According to Zayyoun et al., 2016, Nikam et al., 2014 pure CuO phase was formed at high pH range. After that, Visalakshi et al., 2017 proved that the absorption edges of the CuO is blue shifted as the pH increased. To get the phase pure CuO for designing visible light photocatalyst pH range is fixed as 11. Corresponding reactions takes place in the synthesis can be expressed as follows [Cudennec et al., 2003]

$$Cu^{2+} + 2OH^{-} = Cu(OH)_2 \quad \text{---------- (2.2)}$$

$$Cu(OH)_2 + 2OH^{-} \leftrightarrow Cu(OH)_4^{2-} \quad \text{---------- (2.3)}$$

$$Cu(OH)_4^{2-} \leftrightarrow CuO + 2OH^{-} + H_2O \quad \text{---------- (2.4)}$$

Thus the synthesized CuO was without any surfactant materials. In the present case, effort is taken to change the morphology of CuO, by changing the concentration of surfactant. Since the synthesize method is selected as wet chemical method, we have decided to choose water soluble surfactants. Polyethylene glycol (PEG) is mostly used cheapest and low toxic surfactant in the nano research field. We wish to know, the monomer of this PEG can treat as a surfactant. So we have chosen Ethylene glycol and Polyethylene glycol-400 as surfactant for our current project. Then we have chosen Polyvinyl Pyrrolidine K_{30}cause we wish to study the effect of very long chain polymer. Then we have chosen Cetyltrimethyl ammonium bromide since it gives good morphological changes. Then we want to study the surfactant effect of Igepal since it was not reported earlier for CuO synthesis. Igepal is not water soluble surfactant so that we have chosen a solid state reaction method to use Igepal surfactant.

2.7 Outline of the Work

Nanomaterial Synthesis

- Wet chemical synthesis

  (Using EG, PEG-400, PVP $K_{30,}$ CTAB)
- Solid state reaction method

  (Using Igepal-210)

Characterization studies

- X-Ray diffraction (XRD) analysis
- Fourier transform of Infrared (FTIR) studies
- Particle size determination
- Scanning electron microscope (SEM) studies
- UV-Visible Diffusion reflection spectroscopy

- Impedance analysis
- Dielectric properties studies

Applications

- Photocatalysts

  (Sun light driven photocatalytic properties using Congored dye)

- Supercapacitors

  (CV studies carried out using symmetric CuO electrodes)

.

CHAPTER - III
EXPERIMENTAL TECHNIQUES

3.1. Introduction

This chapter discusses about the various experimental techniques that are used in the characterization of nanomaterials and nanostructures. The research contains three major characterization categories. They are

1. Structural and Morphological studies
2. Vibrational studies
3. Optical characterization studies
4. Electrical characterization studies

The structural and morphological parameters like the particle size, lattice parameters, unit cell volume, crystalline phase and the morphology of the synthesized nanoparticles are analyzed through X-ray powder diffraction spectrum analysis (XRD), scanning electron microscope images (SEM) and Particle size analyzer.

Vibrational studies of the synthesized materials were carried out using Fourier Transform Infra Red Spectroscopy. The optical characterization of the synthesized nanoparticles is carried out using UV-Vis Diffuse reflectance spectroscopy. The band gap energy analysis of the samples is also carried out using UV – Vis spectral analysis.

Impedance Spectroscopy (IS) has become a major tool for investigating the electrical properties. The synthesized nanoparticles electrical parameters like the dielectric constant, dielectric loss, AC conductivity, activation energy and impedance characterizations are studied through impedance spectroscopy.

3.2 X-Ray powder Diffraction (XRD) analysis

3.2.1 Introduction

X-ray diffraction (XRD) is a powerful nondestructive technique for characterizing crystalline materials. It provides information on structures, phases, preferred crystal orientations (texture), and other structural parameters, such as average grain size, crystallinity, strain, and crystal defects. Consequently, the X-ray diffraction pattern is the fingerprint of periodic atomic arrangements in a given material. X-ray diffraction is pertaining to the fields of pharmaceuticals, forensic science, geological applications, microelectronics, and glass manufacturing.

3.2.2. Theory

X-ray diffraction peaks are produced by constructive interference of a monochromatic beam of X-rays scattered at specific angles from each set of lattice planes in a sample. The peak intensities are determined by the distribution of atoms within the lattice. These X-rays are generated by a cathode ray tube, filtered to produce monochromatic radiation, collimated to concentrate, and directed toward the sample. The interaction of the incident rays with the sample produces constructive interference (and a diffracted ray) when conditions satisfy as shown in Fig. 3.1 Bragg's law:

$$n\lambda = 2d\ sin\theta \qquad \text{---------- (3.1)}$$

Where n is an integer

λ is the wavelength of the X-rays

d is the interplanar spacing generating the diffraction and

` θ is the diffraction angle.

This law relates the wavelength of electromagnetic radiation to the diffraction angle and the lattice spacing in a crystalline sample. These diffracted X-rays are then detected, processed, and counted. By scanning the sample through a range of 2 θ angles,

all possible diffraction directions of the lattice should be attained due to the random orientation of the powdered material. Conversion of the diffraction peaks to d-spacings allows identification of the compound because each compound has a set of unique d-spacings. Typically, this is achieved by comparison of d-spacings with standard reference patterns.

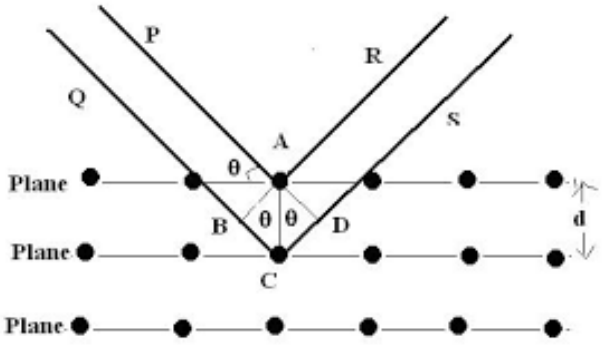

Figure 3.1: Geometrical explanation of X- ray diffraction

3.2.3 Instrumentation

The schematic and instrument diagram of the X-rat diffractometer was shown in Fig.3.2. X-ray diffractometer consists of the following components.

(i) X-ray tube

(ii) Goniometer and optical path

(iii) Sample holder

(iv) Detector

(v) Signal processor and readout.

When an atom is bombarded with sufficiently high energy electrons, electrons of the atom are knocked out from their shell (excited state, unstable) leads to transition of electrons to fill up the vacancy (ground state, stable). Each electron transition generates X-rays of a specific energy (with wave length in the range from 0.1Å to 100Å)

equivalent to that shell. Wavelength of commonly used X-rays from copper source is given below [Hölzer et al., 1997]

$CuK\alpha_1$ = **1.540598**

$CuK\alpha_2$ = **1.544426**

$K\alpha_1/K\alpha_2$ = **2**

CuK_β =**1.392250**

Most recent values are from Diffractometer circle is also known as goniometer circle. Goniometer is the central component of an x-ray diffractometer and contains the specimen holder. It has arm to which the x-ray source and detector are mounted. Usually goniometer is vertically mounted but those used for thin film studies are horizontally mounted. A goniometer is an instrument that either measures angle or allows an object to be rotated to a precise angular position.

In the diffractometer, the intensity of the diffracted beam is measured directly by an electronic X-ray detector. They are many types of detectors (sometimes called counters), but they all convert the incoming x-rays into surges or pulsed of electric current which are fed into various electronic components for processing. The electronics counts the number of current pulses per unit of time, and this number is directly proportional to the intensity of the X-ray beam entering the detector.

3.2.4 Working

X-rays (usually, K radiation of wavelength 1.5418 Å emitted from copper) required for diffraction are monochromatized by filtering with the help of foils or crystal monochrometers. These X - rays are collimated and directed onto the sample. In powder form a significant number of the crystallites can be expected to be oriented to fulfill the Bragg condition for reflections from every possible interplanar spacing. Thus, the sample and detector are rotated and the intensity of the reflected X- rays are recorded. A detector

records and processes this X - ray signal and converts the signal to a count rate which is then output to a printer or computer monitor. The goniometer is designed such that the sample rotates in

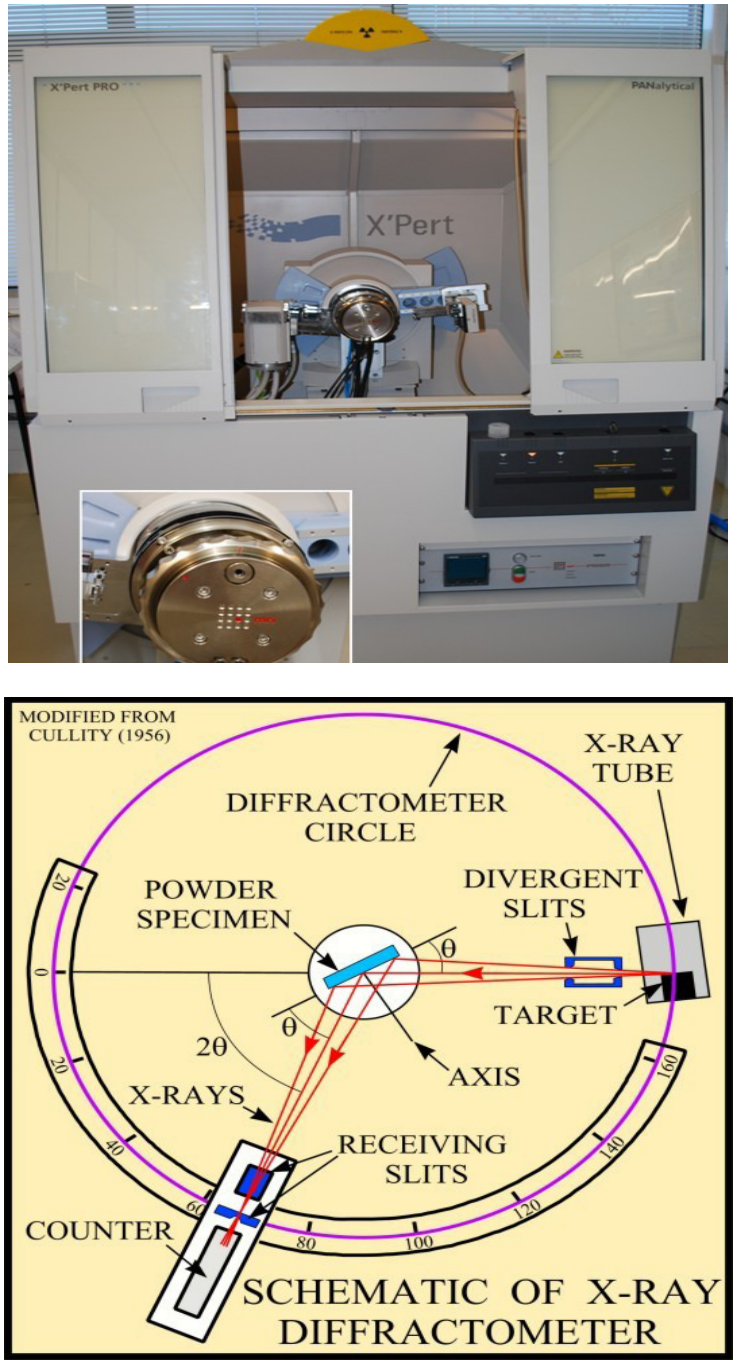

Figure 3.2: X-Ray Diffractometer: Instrument and schematic diagram

the path of the collimated X - ray beam at an angle while the X - ray detector on an arm to collect the diffracted X - rays rotates at an angle of. For typical powder patterns, data is collected for a range of 5° to 70° at scan speed of 2° min1. The position of a diffraction peak is dependent only on the size and shape of the unit cell. Each peak represents a certain lattice plane and can therefore be characterized by a Miller index.

3.3 Fourier Transform of Infrared spectrum (FTIR)

3.3.1 Introduction

Infrared spectroscopy deals with the interaction of infrared light with matter. Molecules and crystals can be thought of as systems of balls (atoms or iron) connected by springs (chemical bonds).These systems can be set into vibration, and vibrate with frequencies determined by the mass of the balls (atomic weight and by the stiffness of the springs (bond strengths). Bond lengths and bond angles are continuously changing due to this vibration. All the motions can be described in terms of two types of molecular vibrations, namely stretch and bend. Stretching is rhythmic movement along the line between the atoms. Inter atomic distance may be either increasing or decreasing. Stretching may be symmetric or asymmetric. Bending is the second type of vibration which makes a change in bond angle. Bending can occur in the plane of the molecule or out of plane. The bending and stretching of molecules are shown in Fig. 3.3.

3.3.2 Principle

The mechanical molecular and crystal vibrations are at very high frequencies ranging from 10^{12} to 10^{14} Hz, which is in the infrared (IR) regions of the electromagnetic spectrum. The sample is bombarded with infrared radiation. When the frequency of infrared radiation matches the natural frequency of the bond the amplitude of the vibration increases, and the infrared is absorbed. Thus the absorption frequencies represent excitations of vibrations of the chemical bonds and thus are specific to the type of bond and the group of atoms involved in the vibration.

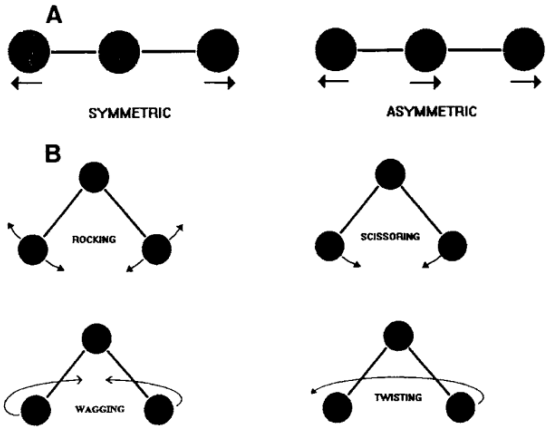

Figure 3.3: Types of molecular vibrations: a) Stretching vibrations; b) Bending vibrations.

3.3.3. Instrumentation and working

The schematic diagram of an FT-IR is shown in Fig. 3.4. The FTIR uses an interferometer to process the energy sent to the sample. In the interferometer, the source energy passes through a beam splitter, a mirror placed at a 45° angle to the incoming radiation, which allows the incoming radiation to pass through but separates it into two perpendicular beams, one undeflected, the other oriented at a 90° angle. The beam, which is oriented at 90° goes to a stationary or fixed mirror and is returned to the beam splitter. The undeflected beam goes to a moving mirror and is also returned to the beam splitter. The motion of the mirror causes the path length that the second beam traverses to vary. When the two beams meet at the beam splitter, they recombine, but the path length differences (differing wavelength content) of the two beams cause both constructive and destructive interferences. The combined beam containing these interference patterns are called the interferogram. The intensity-time output of the interferometer is subjected to a Fourier transform to convert it to the familiar spectrum of intensity vs frequency spectrum.

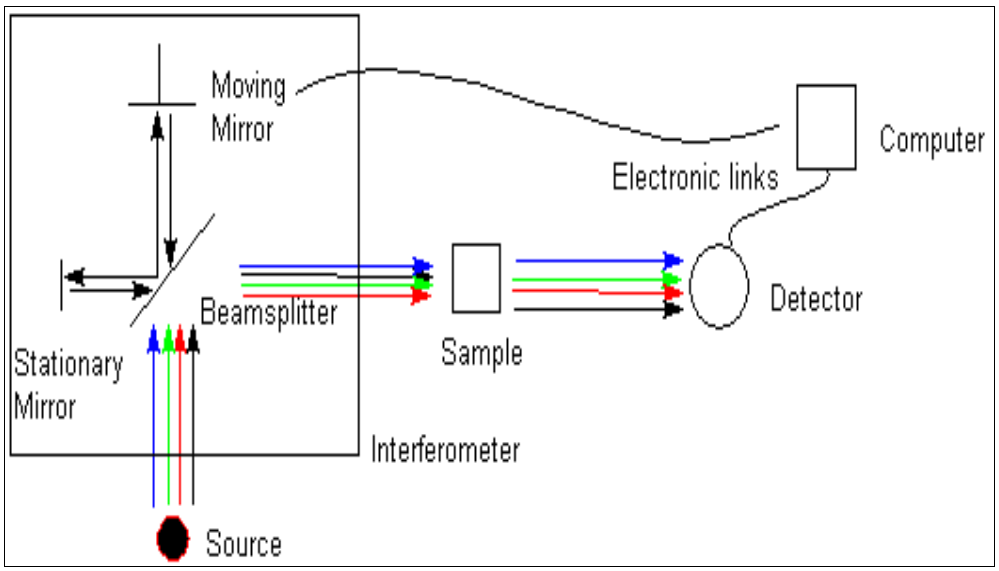

Figure 3.4: FT-IR spectrometer: Instrument and schematic diagram

3.4. Particle size Analyzer

3.4.1 Introduction

The Particle size analyzer (Nano Plus Particulate systems) is a unique instrument that utilizes photon correlation spectroscopy to determine particle size. Dynamic Light Scattering (DLS) is also known as Photon Correlation Spectroscopy (PCS). DLS is used to size particles from below 5 nm to several microns.

3.4.2 Principle

DLS analysis the hydrodynamic diameter is measured through optical detection of the Brownian molecular motion of particles in a liquid. The thermally agitated liquid molecules collide with the particles causing a random movement or diffusion. The movement (diffusion) of these particles is described by the Stokes-Einstein equation

$$D = \frac{k_B T}{6\pi\eta R} \qquad \text{---------- (3.2)}$$

Where the diffusion (D) is equal to the product of Boltzman's constant (k$\boldsymbol{B}$) divided by the hydrodynamic radius of the particle (R) of the particle and the shear viscosity of the solvent ($\boldsymbol{\eta}$). According to the Stokes-Einstein equation the diffusion velocities are inversely proportional to the size of the particles. Larger particles have a slower velocity and will have smaller coefficients of diffusion than larger particles.

3.4.3 Instrumentation and working

Fig. 3.5 shows the instrument and schematic diagram of a DLS instrument. In most DLS systems a laser (i.e. He-Ne) of known wavelength passes through a dilute sample in solution and the intensity of scattered light is collected by a detector and de-convoluted by algorithms to determine the particle size distribution of the sample. The amount of scattered light collected is dependent on the molecular weight, size, and shape of a particle as well as the refractive indices of the particle and solvent. Before reaching the detector

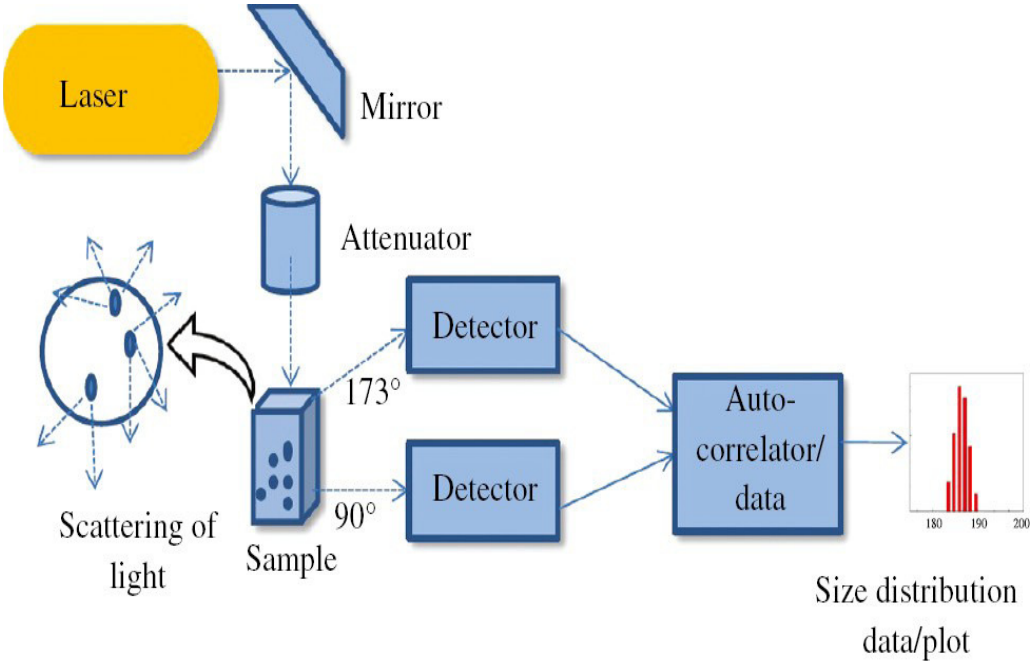

Figure 3.5: Particle size analyzer: Instrument and Schematic diagram

the scattered light from individual particles experiences interference from those scattered by other particles all of which are moving randomly due to Brownian motion. This results in random fluctuations in time. Fig. 3.6 shows a typical intensity Vs time plot for three differently sized particles diffusing in solution. The time scale of the fluctuations shown in the figure is dependent on the particle diffusivity and size of the particles. Smaller particles will jitter about more quickly than larger particles. The figure shows representative time Vs intensity plots for “small” (3a), “medium” (3b) and “large” (3c) particles

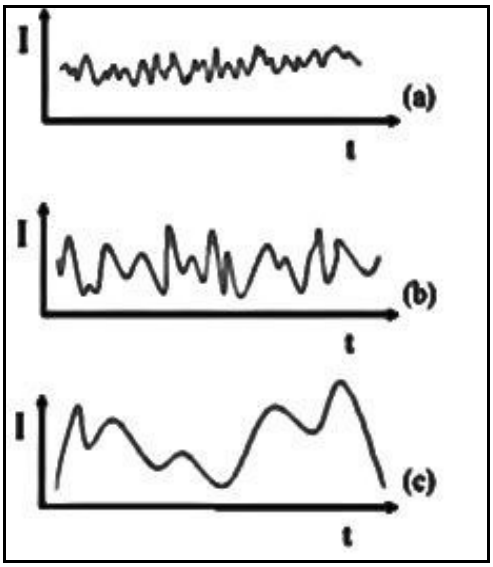

Figure 3.6: Plot of Intensity Vs time for three differently sized particles.

To determine the numerical size of the particles it is necessary to correlate intensity to the diffusion coefficient of the particles. This is done using an autocorrelation function or ACF This function examines the changes in scattered intensity over periods of time for a volume of particles. In the case of a simple mono disperse particle size distribution (PSD) the ACF is a single decaying exponential function (eqn. 2.4). After a series of calculations a decay constant (t) is found that is inversely proportional to the diffusivity of a particle as shown in equations where K is a

constant called the “scattering wave vector”. This constant relates the time scale of the diffusion process to the distance scale set by the laser wavelength. K is dependent on the wavelength of the laser (λ), q is the angle of detection and the index of refraction of the solvent.

$$Ct' = < I(t) * I(t - t') > \quad \text{---------- (3.3)}$$

$$C(t') = Aexp\left(\frac{-t'}{\tau}\right) + B \quad \text{---------- (3.4)}$$

$$\frac{1}{\tau} = 2DK^2 \quad \text{---------- (3.5)}$$

$$D = \left(\frac{1}{2K^2}\right)\left(\frac{1}{\tau}\right) \quad \text{---------- (3.6)}$$

$$k = \left(\left(\frac{4\pi\eta}{\lambda}\right)\frac{sin\theta}{2}\right) \quad \text{---------- (3.7)}$$

Once the coefficient of diffusion is known the hydrodynamic radius can be determined using the Stokes-Einstein equation.

3.5 Scanning electron microscopy (SEM)

Scanning electron microscopy (SEM) uses a finely focused beam of electrons in order to produce a high resolution image of a sample. SEM images have a three dimensional appearance, which is very useful when examining the surface structure of a sample.

3.5.1 Principle

When a specimen is hit with a beam of the electrons known as the incident beam, it emits X-rays and three kinds of electrons: primary backscattered electrons, secondary electrons and Auger electrons. The SEM uses primary back scatter electrons (BSE) and secondary electrons. An electron recorder picks up the rebounding electrons and records their imprint. This information is translated onto a screen which allows three-dimensional images to be represented clearly. One of the SEM's greatest advantages is its ability to reproduce textual information in a consistent and coherent manner.

3.5.2 Construction

Essential components of SEM are

- Electron Source ("Gun")
- Electron Lenses
- Sample Stage
- Detectors for all signals of interest
- Display / Data output devices

It consists of an electron gun to produce high energy electron beam. A magnetic condensing lens is used to condense the electron beam and a scanning coil is arranged in-between magnetic condensing lens and the sample. The electron detector (Scintillator) is used to collect the secondary electrons and can be converted into electrical signal. These signals can be fed into CRO through video amplifier as shown in Fig. 3.7

3.5.3 Working

The electron gun produces an electron beam when tungsten wire is heated by current. This beam is accelerated by the anode. The beam travels through electromagnetic fields and lenses, which focus the beam down toward the sample. A mechanism of deflection coils guides the beam so that it scans the surface of the sample in a rectangular frame (raster pattern). When the beam touches the surface of the sample, it produces Secondary electrons (SE) and Back scattered electrons (BSE). The emitted SE is collected by Secondary electron detector (SED) and converted into signal that is sent to a screen which produces final image. Additional detectors collect these X-rays, BSE and produce corresponding images.

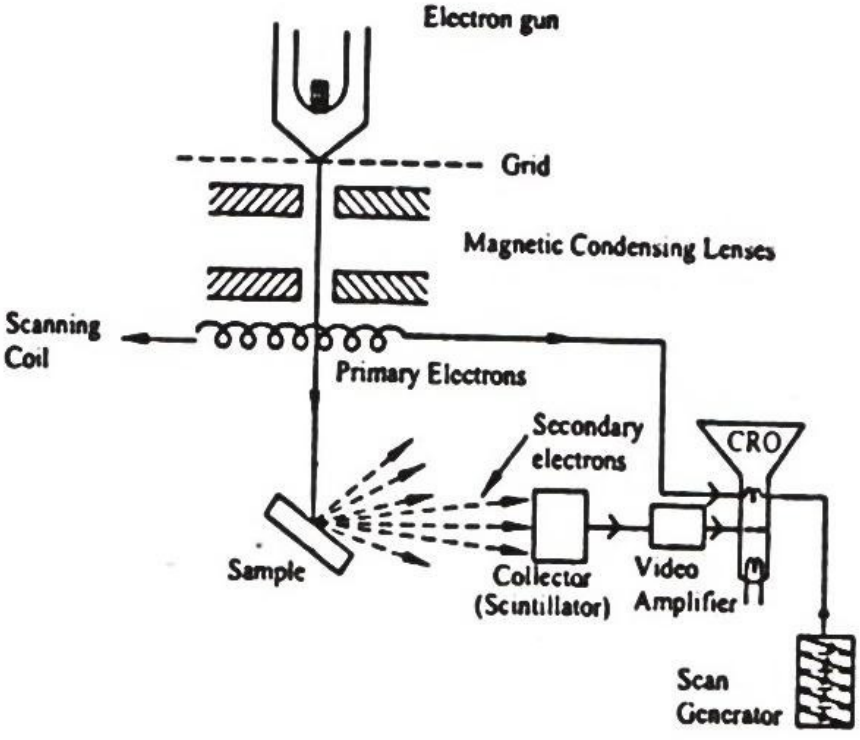

Figure 3.7: SEM: Instrumentation and Schematic diagram

3.6 Diffuse reflection spectroscopy

3.6.1 Introduction

DRS is the more convenient technique to characterize unsupported nanomaterials than UV-Vis absorption spectroscopy, since it takes advantage of the enhanced scattering phenomenon in powder materials. UV-VIS most often refers to absorption spectroscopy, measured by transmission, whereas DRS specifically refer to diffuse reflection spectroscopy. Normally, the former is used for solutions/suspensions or thin films, whereas the latter is used for solids - optically rough films or powders Effects of light scattering in the absorption spectra of powder samples dispersed in liquid media can be avoided using DRS. If the absorption peak is not well resolved, even the use of derivative of absorption spectra does not guarantee the exact estimation of E_g, and can lead erroneous conclusions. Finally, the DRS technique does not require a powder sample to be dispersed in any liquid medium, so the material is not contaminated or consumed [Carmichael et al., 1996]. Reflectance, which is the base quantity that characterizes the process of reflection, is defined as the ratio of the reflected radiant flux to the incident radiant flux (or power). Reflectance is introduced by Kubelka–Munk scientists. Reflectance can be measured wide wavelength range from 250-950 nm. Reflectance is characteristic for each of drug molecules, solid samples and paints

3.6.2. Theory

Reflectance spectroscopy is very closely related to UV/Vis spectroscopy, in that both of these techniques use visible light to excite valence electrons to empty orbitals. The difference in these techniques is that in UV/Vis spectroscopy one measures the relative change of transmittance of light as it passes through a solution, whereas in diffuse reflectance, one measures the relative change in the amount of reflected light off of a surface. Specular reflectance refers Mirror like reflectance from a surface with well-

defined angle of reflection whereas diffuse reflectance refers to the Reflected radiant energy that has been partially absorbed, transmitted and partially scattered by a surface, with no defined angle of reflection.

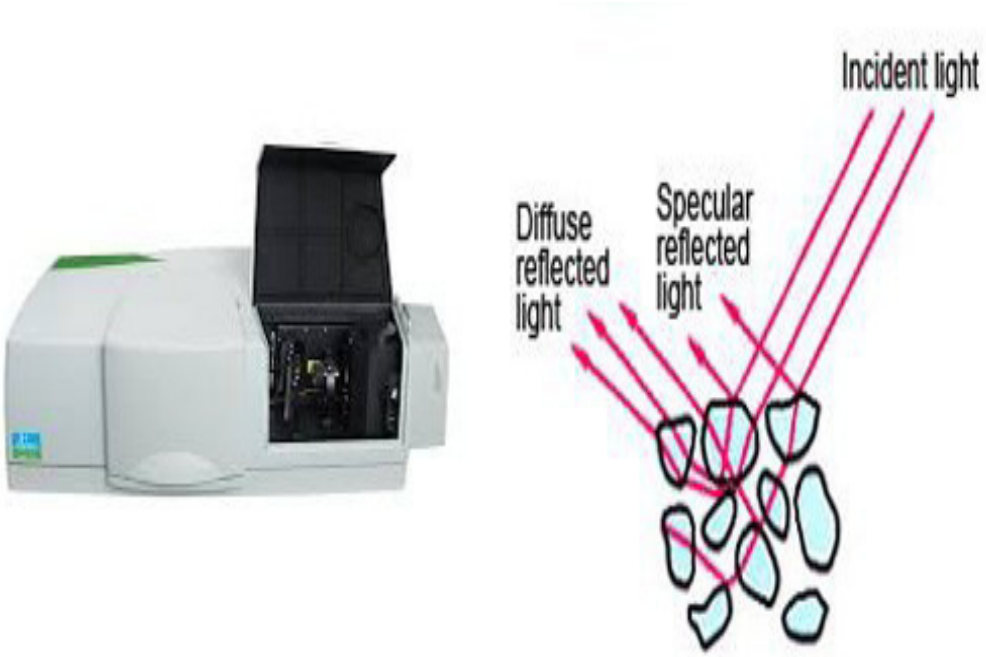

Figure 3.8: (a) UV-vis Diffuse reflectance spectrometer (b) diffuse reflectance

3.6.3 Instrumentation

UV-Vis diffuse reflectance spectrophotometer that consist mainly following components.

1. Light source
2. Integrating sphere
3. Sample holders
4. Detectors

An integrating sphere is an optical device used to collect and measure electromagnetic radiation. An integrating sphere (also known as an Ulbricht sphere) is an optical component consisting of a hollow spherical cavity with its interior covered with a

diffuse white reflective coating, with small holes for various coating material for integrating sphere are MgO, $BaSO_4$ and PTFE (poly tetra fluoro ethylene) compounds.

3.6.4 Working

When light shines onto a powder sample, it is reflected in all directions, as shown in Fig. 3.8 (b). Some of the light undergoes specular reflection at the powder surface. Due to the variety of powder shapes, it is reflected in many directions, unlike light reflected from a mirror. The remainder of the light is refracted as it enters the powder, where it is scattered due to internal reflection, reflection from the surfaces of other powder grains, or repeated refraction entry into the powder. Some of this scattered light is emitted back into the air. As the diffuse reflected light is reflected or passes through the powder, it becomes weaker if absorption by the powder occurs. This results in a diffuse reflected spectrum, similar to the transmission spectrum. However, in regions where the powder exhibits strong absorption, most of the diffuse reflected light in long light paths is absorbed, such that only the diffuse reflected light from short light paths is emitted back into the air. Conversely, in bands of weak absorption, some light is not absorbed even in long light paths and this diffuse reflected light is emitted to the air, resulting in stronger peaks than the transmission spectrum. In such a diffuse reflectance spectrum, the absorbed wavenumber positions are the same as the transmission spectrum. However, the relative intensity between peaks differs from the transmission spectrum because the weak peaks in the transmission spectrum become comparatively stronger in the diffuse reflectance spectrum. The so called K-M function ($f(R_\infty)$) derived by Kubelka-Munk is used for comparison to transmission spectra or quantitative analysis.

$$F(\alpha) = \frac{(1-R)^2}{2R} = \frac{K}{S} \qquad \text{---------- (3.8)}$$

Where, R is the absolute reflectance, K is the absorption coefficient, and S is the scattering coefficient. In order to resolve the excitonic or inter band (valence conduction band) transition, which allows to calculate the band gap (E_g) energies were estimated from the plot of the Kubelka-Munk remission function (converted from the diffuse reflection values) vs. energy (in eV) spectra. Here (R) is the absolute value of reflectance and F(R) is equivalent to the absorption coefficient (α) used in Tauc's plot.

3.7. Electrochemical impedance spectroscopy

3.7.1 Introduction

Electrochemical impedance spectroscopy (EIS) is a well-established powerful technique for investigating many electrical properties of materials and their interfaces. This technique has been used for studying corrosion processes, interfacial reaction mechanisms, and dynamics of mobile charge in bulk or interfacial regions of any material. The flow rate of charged particles and current depends on the ohm'ic resistance of the electrodes and the electrolyte. Large number of parameters can be deduced from EIS data; the material properties such as conductivity, dielectric properties relaxation frequency and the interfacial properties such as adsorption-reaction rate constants, interface capacitance, diffusion coefficient. From the theoretical point of view, the impedance and the dielectric are quantities that are interesting to measure. The Z-View software is used to find out the electrical circuit model responsible for the electrical behavior of the synthesized nanoparticles. In this project, the synthesized nanoparticles electrical parameters like the impedance characterizations, dielectric AC conductivity, activation energy, dielectric constant and dielectric loss are studied through impedance spectroscopy.

3.7.2 Impedance theory

Electrochemical impedance is usually measured by applying an AC potential to an electrochemical cell and then measuring the current through the cell. Assume that we apply a sinusoidal potential excitation. The response to this potential is an AC current signal. This current signal can be analyzed as a sum of sinusoidal functions. A method of measuring the electrical impedance of a substance as a function of the frequency of an applied electrical current

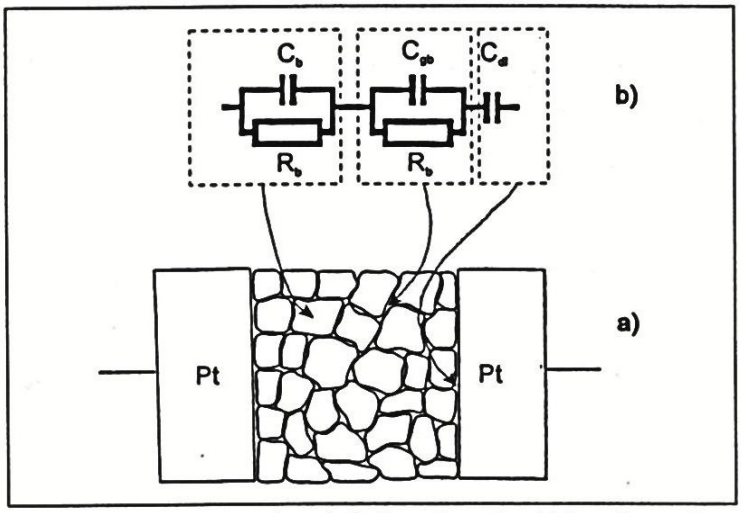

Figure 3.9: Regions of exchange of interaction between current and sample

When the pelletized sample is sandwitched between two electrodes , there are three basically different regions inside the grains (bulk) , at grain boundaries, surface of the electrodes for the exchange interactions between current and sample as shown in Fig. 3.9. The term impedance refers to the frequency dependent resistance to current flow of a circuit element (resistor, capacitor, inductor, etc.).

Impedance: $Z_\omega = E_\omega / I_\omega$ ---------- (3.9)

E_ω = Frequency-dependent potential

I_ω= Frequency-dependent current

This is equivalent to the Ohm's Law: R = E/I, where R = impedance at the limit of zero frequency. The impedance is expressed as a vector, where the raw data at each measured frequency consists of the real and imaginary components of the applied potential and measured current.

The impedance can be written as

$$Z = Z' + j\,Z'' \qquad \text{---------- (3.10)}$$

Where $j = \sqrt{-1}$

$$Z' = |Z| \cos\theta \qquad \text{---------- (3.11)}$$

$$Z'' = |Z| \sin\theta \qquad \text{---------- (3.12)}$$

The measured impedance data can be represented in the other three forms, using the inter relations as follows

Complex Admittance $\mathbf{Y^* = Y' + jY'' = 1/Z^*}$ ---------- (3.13)

Complex permittivity $\mathbf{\varepsilon^* = \varepsilon' - j\varepsilon'' = 1 / j\omega C_0 Z^*}$ ---------- (3.14)

3.7.3 Representation of Impedance Data

The expression for Z(ω) is composed of a real and an imaginary part. If the real part is plotted on the X-axis and the imaginary part is plotted on the Y-axis of a chart, one can get a "Nyquist Plot". In this plot the Y-axis is negative and that each point on the Nyquist Plot is the impedance at one frequency and low frequency data are on the right side of the plot and higher frequencies are on the left. One major disadvantage of Nyquist plot is that information on frequency is lost. On the Nyquist Plot the impedance can be represented as a vector (arrow) of length |Z|. The angle between this vector and the X-axis, commonly called the "phase angle. The shape of the curve provides insight into possible mechanism or governing phenomena.

- An ideal Debye type single relaxation time is represented by the perfect semicircle with one time constant as centre as shown in Fig. 3.10 (a)

- If a symmetrical distribution of relaxation times occur about a mean relaxation time, then a depressed semicircle is found in the Nyquist plot of impedance Fig. 3.10(b)
- The skewed arc shaped curve is characteristic of a non- uniform distribution of relaxation mechanisms, where the distributions on the higher frequency side of the principal relaxation time decreases more rapidly than those on the low frequency side was shown in Fig. 3.10 (c).

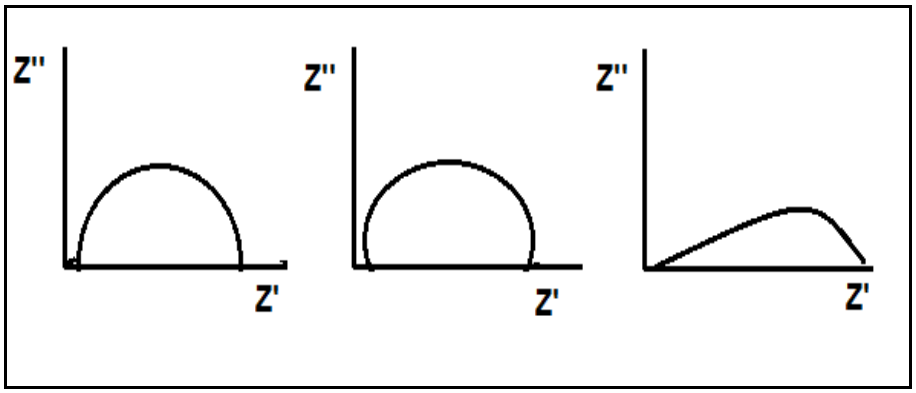

Figure 3.10: The Nyquist plot models (a) semicircle,

(b) depressed semicircle, (c) Skewed arc shaped curve

There is a strong correlation between the frequency response and the temperature dependence of electrical conductivity of the materials. The temperature dependence of σ_{ac} shows the presence of single or multiple relaxations in the material. In bulk materials two types of ac conductivity phenomena occurs; (a) long range ac conductivity and (b) localized transport oxygen vacancies

3.7.4 Conductivity studies

The ac conductivity (σ_{ac}) is calculated using the formula,

$$\sigma_{ac} = \epsilon_0 \epsilon_r \, \omega tan\delta \qquad \text{---------- (3.15)}$$

Where ϵ_0 is the permittivity of free space, ϵ_r is the relative permittivity, ω is the angular frequency and tan δ is the dielectric loss. Electrical conductivity of nanoparticles as a function of frequency can generally be described as frequency independent, (σ_{dc}) dc conductivity, and a strongly frequency dependent components. A typical frequency dependence of conductivity spectrum shown the Fig. 3.11 exhibits three regions

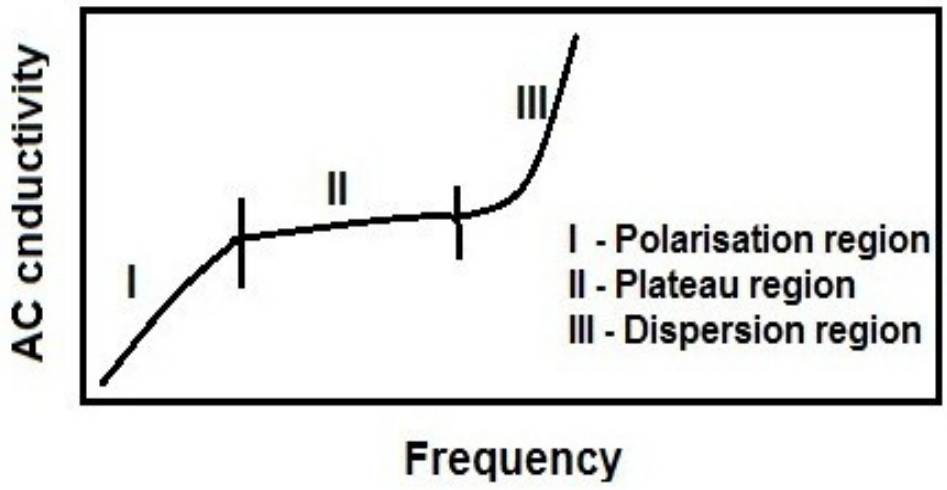

Figure 3.11: Model plot of log conductivity Vs frequency

1. Low frequency dispersion
2. An intermediate frequency plateau
3. An extended dispersion at high frequency.

The variation of conductivity in the low frequency region is attributed to the polarization effects. As the frequency reduces, more and more charge accumulation occurs at the electrode and electrolyte interface and hence, drops in conductivity. In the intermediate frequency plateau region, conductivity is almost found to be frequency independent and is equal to dc conductivity σ_{dc}. In the high frequency region, the

conductivity increases with the frequency. The conduction mechanism in this range of frequency corresponds to the well-localized hopping motion. The frequency dependence of conductivity is related by a simple expression given by Jonscher's power law.

$$\sigma(\omega) = \sigma_{dc} + A\omega^{n} \quad \text{---------- (3.16)}$$

Where, $\sigma(\omega)$ is the AC conductivity, σ_{dc} is the limiting zero frequency conductivity, A is a pre-exponential constant, $\omega = 2\pi f$ is the angular frequency and n is the power law exponent.

3.7.5 Dielectric studies

Dielectric property is a characteristic of a short range electrical conduction of a material under the influence of an applied electric field. When a field is applied across a material, the applied field V displaces the charges within the material and results in the accumulation of charges at the interface, creating dipoles with a moment $\mu = Q\delta$, where δ is the separation distance between the charges and Q is the charge.

$$Q = CV \quad \text{---------- (3.17)}$$

Where C is the capacitance of the material is given by

$$C = C_0\, \varepsilon/\varepsilon_0 \quad \text{---------- (3.18)}$$

C_0 is the vacuum capacitance and is given by $C_0 = \varepsilon_0 A/t$, where ε_0 is the permittivity of free space, A is the area of cross section and t is the thickness of the material. In a material, if field V varies with time, then the induced charge is given by

$$Q = \varepsilon^* V_0 \exp(j\omega t) \quad \text{---------- (3.19)}$$

Where ε^* is the complex dielectric constant and it is defined as

$$\varepsilon^* = \varepsilon' - i\varepsilon'' \quad \text{---------- (3.20)}$$

Where ε' is the real or relative permittivity or dielectric constant, ε'' is the imaginary or dielectric loss. ε^* can be represented as

$$\varepsilon^* = 1/(j\omega C_0 Z^*) \quad \text{---------- (3.21)}$$

ω is the angular frequency and C_0 is the capacitance of free space.

$$\varepsilon = \frac{t}{\omega \varepsilon_0}\left(\frac{Z'}{Z'+Z'^2}\right) \quad \text{--------- (3.22)}$$

$$\varepsilon' = \frac{t}{\omega \varepsilon_0}\left(\frac{Z'}{Z'+Z'^2}\right) \quad \text{--------- (3.23)}$$

From the Fig. 3.12(a) the increase in ε' with decreasing frequency can be attributed to the contribution of charge accumulation at the interface.

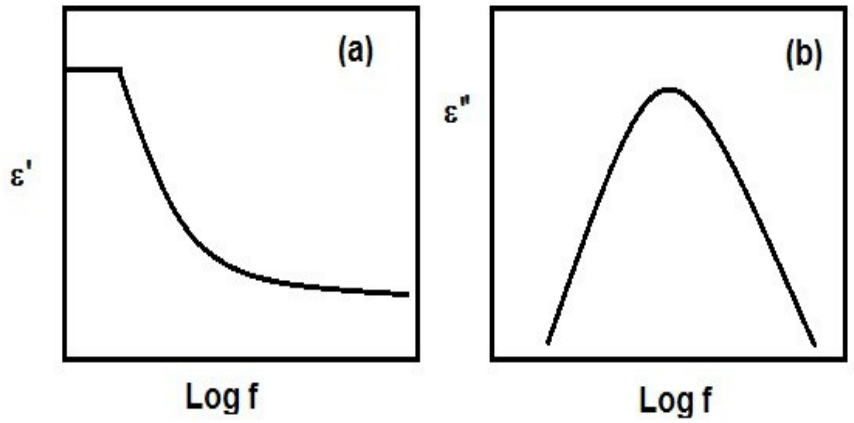

Figure 3.12: Model plots of the Dielectric parameters

(a) ε' b) ε'' as a function of log f

This leads to a net polarization of the ionic medium, which contributes to ε'. whereas at high frequencies, the periodic reversal of the field takes place so rapidly such a way that there is no charge accumulation in the interface, resulting in constant ε' value. Fig. 3.12(b) shows the ε'' as a function of frequency exhibit symmetric Debye behaviour with a loss tangent maximum at its characteristic frequency f_{max}. Many materials show a non-Debye dielectric behaviour characterized by a broader asymmetric loss peak and by a constant loss tangent at a frequency higher than the loss peak, where the relaxation effects of the sample begin. Electrochemical work station instrument was shown in Fig. 3.13.

Figure 3.13. Bio logic sp-300 electrochemical work station

3.8 Experimental

The XRD pattern was recorded by XPERT-PRO diffractometer using Cu-Kα radiation (λ=1.54 Å). FTIR spectrum was recorded by KBr pellet technique from 400 cm^{-1} to 4000 cm^{-1} using spectrum RXI Perkin Elmer spectrometer. UV visible spectrum was recorded using Perkin Elmer spectrophotometer from the wavelength of 200 to 1200 nm. SEM analysis was carried out using scanning electron microscope Carl Zeiss EVO 18. Particle size of the Copper oxide nanostructures were analyzed using Particulate systems Nano plus analyzer. Impedance of the pelletized samples was measured using biologic SP-300 electrochemical workstation using stainless steel plates as electrodes. The measurement was taken in the frequency range from 1 Hz to 7 MHz and the temperature range varies from room temperature to 80° C.

CHAPTER - IV

SYNTHESIS AND CHARACTERIZATION OF CuO NANOSTRUCTURES USING ETHYLENE GLYCOL AS SURFACTANT

4. 1. Properties of Ethylene glycol

Formula	:	$C_2H_6O_2$
Appearance	:	colorless, odorless, viscous liquid
Molar mass	:	62.07 g/mol
Boiling point	:	197.3 °C
Density	:	1.11 g/cm³
Melting point	:	-12.9 °C
IUPAC ID	:	Ethane-1, 2-diol
Molecular structure	:	

4. 2. Synthesis of CuO Nanoflakes using EG as surfactant

. Cupric nitrate tri hydrate [$Cu(NO_3)_2 \cdot 3H_2O$] (Himedia 99.5% purity) and sodium hydroxide pellets [NaOH] (Nice chemicals), Ethylene glycol [CH_2OH CH_2OH] (Nice chemicals 99%) were analytical reagent grade chemicals used in this synthesis without further purification. 0.1 M of cupric nitrate solution and 0.2 M of NaOH solutions were made separately using deionized water. With the blue coloured cupric nitrate solution, ethylene glycol (EG) was added and allowed to stir for an hour. Freshly prepared sodium hydroxide solution was added drop by drop with continuous stirring until the solution

reached pH 11. Meanwhile blue color precipitation was formed and turned into black. [Prakash et al., 2015]

Then the black colored precipitation was washed several times by deionized water and ethanol using suction funnel. Washed samples were dried at room temperature for 24 hrs. Then it was kept in oven at 120° C for 10 hrs. A similar procedure was adapted to prepare surfactant assistant CuO nanomaterials with the addition of different concentrations of ethylene glycol 0.05 M, 0.1 M and 0.2 M. Ethylene glycol was added such that the molarity of surfactant is lower, equal and higher than the molarity of precursor salt. The prepared nanoparticles named as NS-W, EG-1, EG-2 and EG-3 respectively.

4.3. Characterizations

4.3.1 XRD analysis

Fig. 4.1 shows the XRD pattern of the Copper oxide nanoflakes. The formation of crystalline Copper oxide nanostructures were confirmed by XRD pattern. The crystallite sizes have been calculated for highest four peaks of all the samples using Debye Scherrer's equation,

$$D = \frac{0.9\,\lambda}{\beta \quad cos\,\theta} \qquad \text{---------- (4.1)}$$

[Cullity & S.R. Stock 1978] Where K is constant (shape factor, about 0.89), λ is x-ray wavelength used (1.54 Å), β is full width at half maximum (FWHM). Average crystallite size and the crystallographic parameters were calculated using UNITCELL software and tabulated in Table 4.1. It shows that the particle sizes of the samples are almost same except EG-3. EG-3 has the smallest crystallite size when compared with the other prepared nanomaterials. It reveals that appropriate amount of EG only can reduce the particle size. It is observed that all the peaks in the XRD patterns are consistent with

the JCPDS (Joint Committee on Powder Diffraction Standards) data (80-1916) of the Copper oxide. No other impurity peaks were identified.

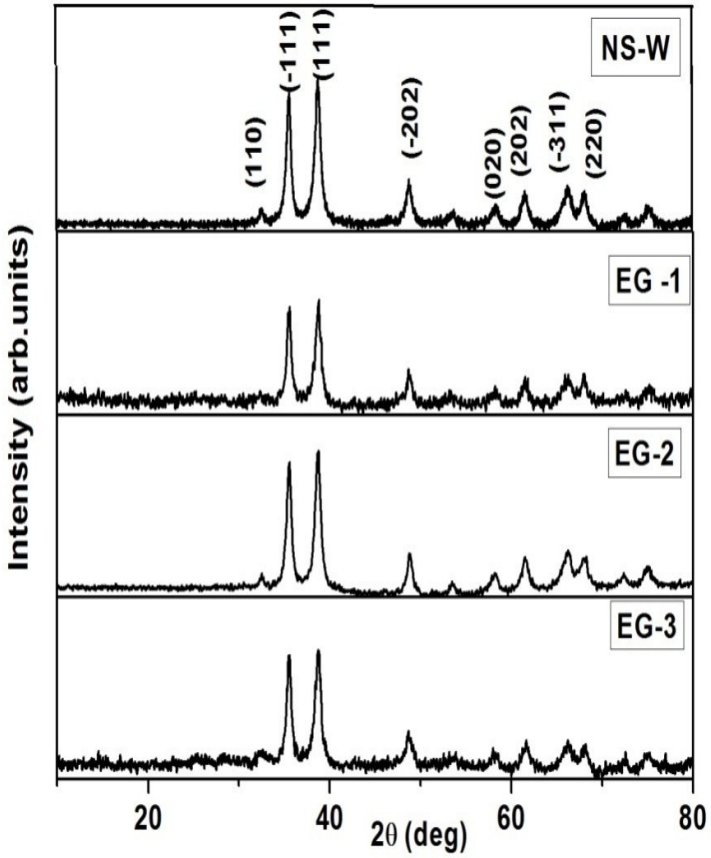

Figure 4.1: XRD pattern of the CuO nanostructures synthesized using EG surfactant

Table 4.1: Crystallographic parameters of the NS-W, EG -1, EG -2 and EG-3

Materials	a	b	c	Beta (Degree)	Cell volume $(Å)^3$	Crystallite size (D) (nm)
	(Å)					
NS-W	4.689	3.420	5.119	99.49	80.99	21
EG-1	4.811	3.197	5.129	99.79	80.23	23
EG-2	4.796	3.210	5.119	99.66	80.13	25
EG-3	4.76	3.324	5.101	99.67	81.02	16

4.3.2 FTIR Analysis

Fig. 4.2 shows the FTIR spectrum and Table 4.2 shows the corresponding peaks of the CuO nanomaterials NS-W, EG -1, EG -2 and EG-3. FTIR Spectrum shows bands around at 600, 520 and 425 cm^{-1}, which can be assigned to the vibrations of Cu-O bonds in CuO phase. The high-frequency mode at 600 cm^{-1} may be due to Cu–O stretching along the ($\bar{1}11$) direction and the mode at 520 cm^{-1} may be Cu–O stretching along (111). Moreover, no other infrared active modes (such as Cu_2O, appearing at 615 cm^{-1}) [Likun Zheng et al., 2007] can be observed. Thus, FT-IR analysis also confirms that the as-obtained product is pure CuO phase. The broad absorption peak around at 3430 cm^{-1} is caused by the adsorbed water molecules since the nano crystalline materials exhibit a high surface to volume ratio and thus absorbs moisture [Asha et al., 2014].

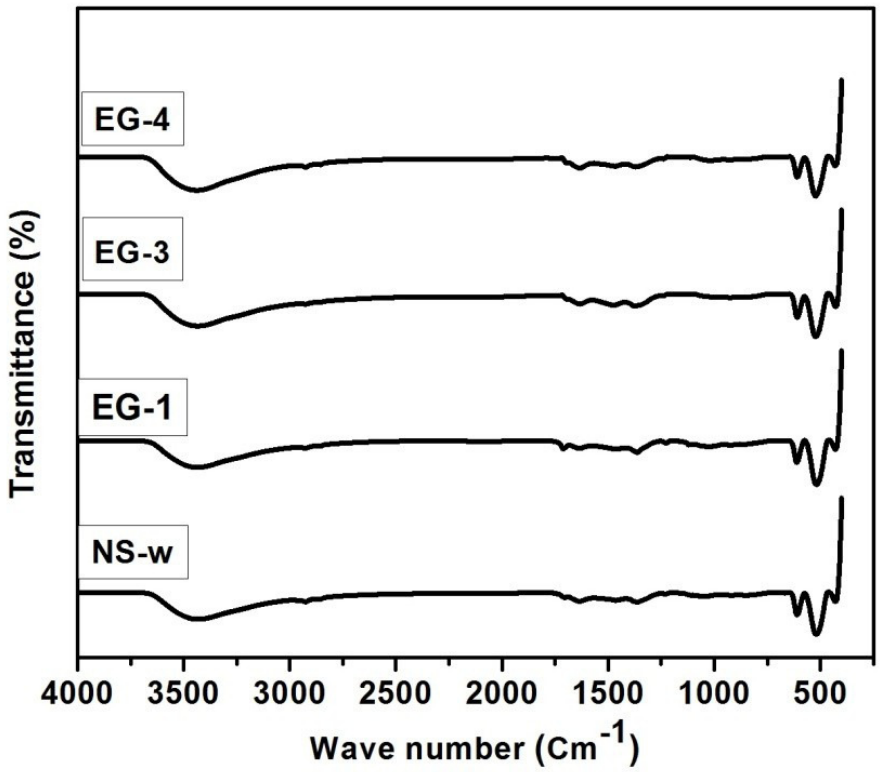

Figure 4.2: FTIR spectrum of the CuO nanostructures synthesized using EG surfactant

Table 4.2: Major FTIR absorption bands and possible assignments for NS-W, EG-1, EG-2, EG-3

Wave number (cm^{-1})				Peaks assigned
NS-W	**EG-1**	**EG-2**	**EG-3**	
429	430	428	431	Cu-O
609	608	606	606	Cu-O
520	519	523	523	Cu-O
3434	3443	3434	3434	O-H bending

4.3.3 SEM analysis

Fig. 4.3 shows the SEM images of (a) NS-W, (b) EG-1, (c) EG-2 and (d) EG-3 Copper oxide nano flakes. SEM images shows that all the samples have flake like morphology. The morphology of the nanomaterials was not affected by the surfactant EG. This may due to the elapse of structure directing properties of EG in the high alkaline (pH=11) experimental condition [Liu et al., 2012]. But the size of flakes is affected by the surfactant. Fig. 4.3 (d) shows the smaller size flakes than other samples. This resembles the result confirmed in XRD.

4.3.4 UV- Vis DRS spectrum analysis

Optical Properties of the synthesized CuO nanostructures was studied by UV-visible diffuse reflection spectrum (DRS). In practice diffuse reflectance spectrum was recorded as the ratio of the reflection from the sample to the intensity of reflection from a standard sample. Fig. 4.4 (a) shows the UV-vis diffuse reflectance spectra of the EG capped CuO nanostructures. The spectrum of the CuO nanostructures exhibits the absorption in the visible region from 400 to 800 nm regions. The absorption of NS-W sample was observed at 880 nm and EG-1 was observed at 537 nm. The absorption edges of all other samples are red shifted when compared with NS-W (EG-2 at 844 nm and EG-3 at 847 nm).

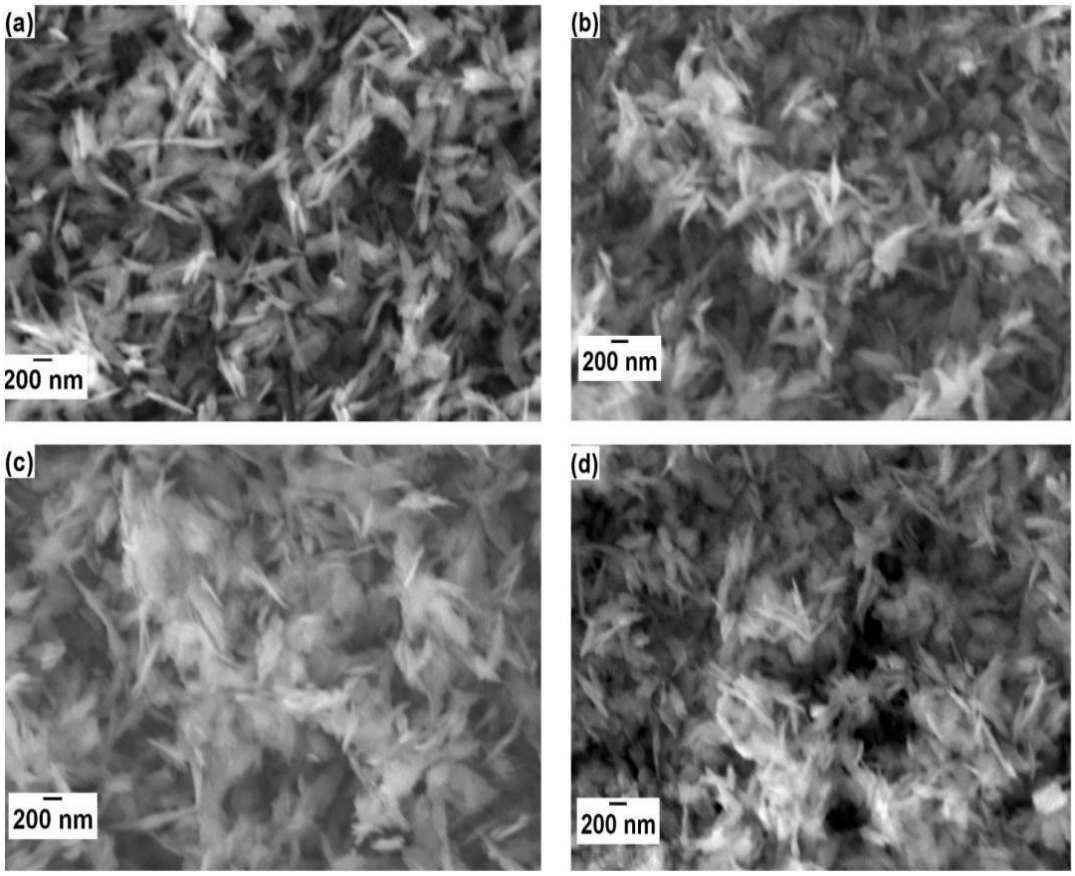

Figure 4.3: SEM images of CuO Nanostructures

(a) NS-W, (b) EG-1, (c) EG-2, (d) EG-3

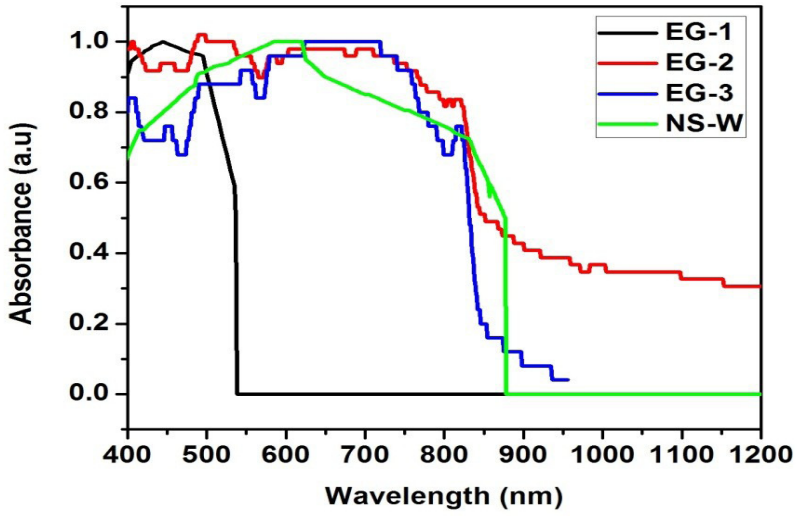

Figure 4.4 (a): UV-Vis diffusion reflection absorption spectrum of CuO nanostructures synthesized using EG surfactant

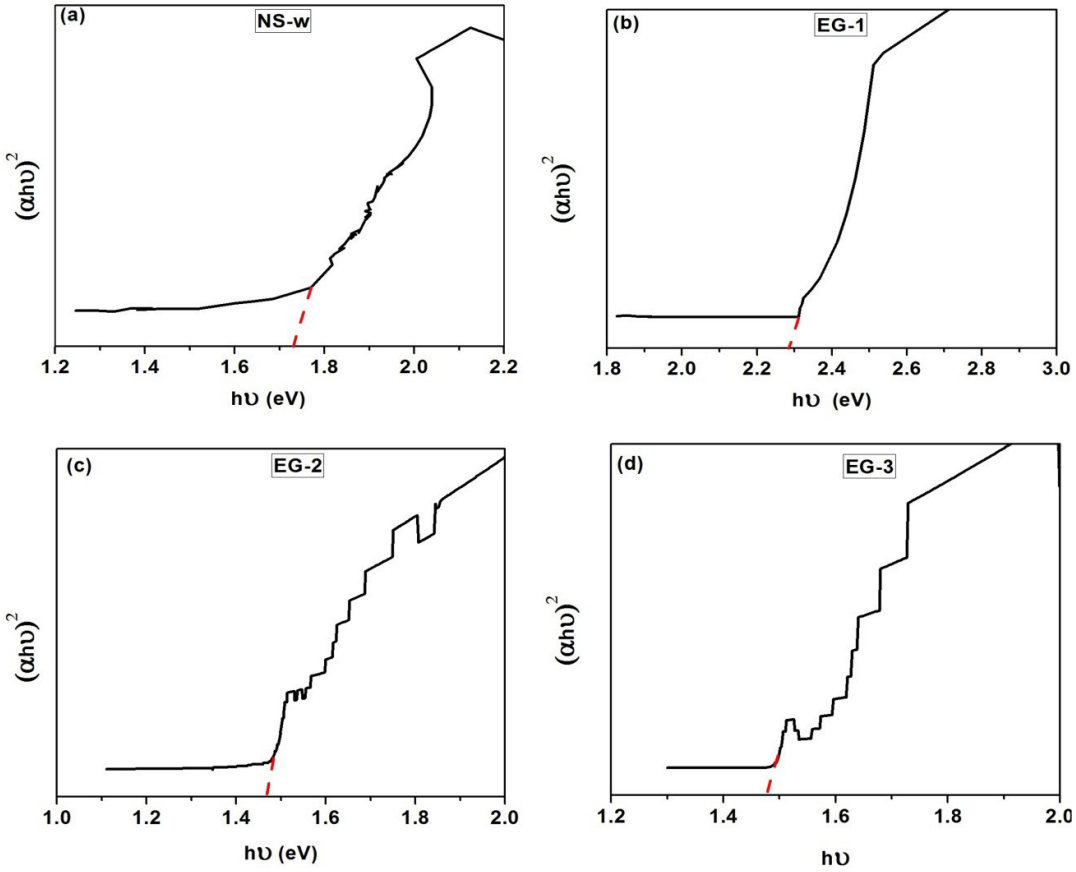

Figure 4.4(b): Plot of $(\alpha h\nu)^2$ vs hν for the samples
(a) NS-W, (b) EG-1, (c) EG-2, (d) EG-3

Fig. 4.4 (b) shows the $(\alpha h\nu)^2$ Vs hν plot for the EG capped nanostructures. Here, α is calculated by the Kubelka-Munk theory $\alpha = (1- R)^2 / 2R$, where R is the reflection, α is the absorption coefficient. Band gap calculated by extrapolating the straight line in the plot of $(\alpha h\nu)^2$ Vs hν at α =0. Band gap of the CuO materials are 1.73, 2.29, 1.47, 1.48 eV for NS-W, EG -1, EG -2, EG-3 respectively. The band gap value of EG-3 is lower than NS-W eventhough with the smaller crystallite size of EG-3. The band gap value of EG-3 is red shifted due to the surface defects [Sukhorukov et al., 2006, Ovchinnikov et al., 2007, Rehman et al., 2011]

4.3.5 Electrical properties

4.3.5.1. Impedance analysis

The real and imaginary part of impedance plot (Nyquist plot) was shown in Fig. 4.5 for the samples (a) NS-W (b) EG-1 (c) EG-2 and (d) EG-3. It reveals that Nyquist plot of all the samples shows a depressed semicircle pattern without any spike, which follows the equivalent circuit of parallel combination of a resistance and a capacitance [Tanmaya et al., 2014]. This indicates that the conductivity of the CuO nanostructures predominated by electrons than the ions. Nyquist plot shows that, impedance decreases with the increase of temperature which inferred that the materials having the behavior of negative temperature coefficient of resistance (NTCR) like semiconductors [Priyanka et al., 2013].

Fig. 4.6 shows the variation of Z″ with respect to the frequency. It shows the characteristic frequency maxima (ω_{max}) peak varies with the temperature. It reveals that the relaxation presented in Copper oxide nano flakes is the temperature dependent. The peaks appear when the hopping frequency of localized charge carriers becomes approximately equal to the applied electric field frequency. In Fig. 4.6(c) and (d), the peak position of Z″ shifts towards higher frequency side with the increase in temperature.

Because hopping frequency of charge carriers increase with the increase in temperature. Relaxation time (τ) was calculated for sample NS-W and EG-2 using the relation

$$\omega_{max}\tau = 1 \qquad \text{---------- (3.4)}$$

$$\tau = \frac{1}{\omega_{max}} \qquad \text{---------- (3.5)}$$

ω_{max} was predicted by fitting Z″ vs log ω plot using Lorentian fit. Relaxation time was calculated and given in Table 4.3 for NS-W and EG-2 samples.

Table 4.3: Relaxation time of the samples NS-W and EG-2 at various temperatures

Temperature (° C)	Relaxation time (μS)	
	NS-W	EG-2
34	4.56	4.62
40	3.31	5.22
50	1.53	2.71
60	0.568	1.32
70	0.401	0.409
80	0.273	0.203

4.3.5.2. AC and DC conductivity studies

Fig. 4.7 shows the temperature and frequency dependent conductivity of the samples NS-W, EG-1, EG-2 and EG-3. It indicates that the conductivity variation shows similar trend for all the temperatures. It has two regions such that low frequency plateau region and high frequency dispersion region. In plateau region applied field frequency is lower than the hopping frequency (frequency at which change in slope of the pattern occurs is known as hopping frequency). At low frequency region, a conductance spectrum is almost independent of frequency. This is due to the occurrence of random hopping of charge carriers [Prakash et al., 2014].

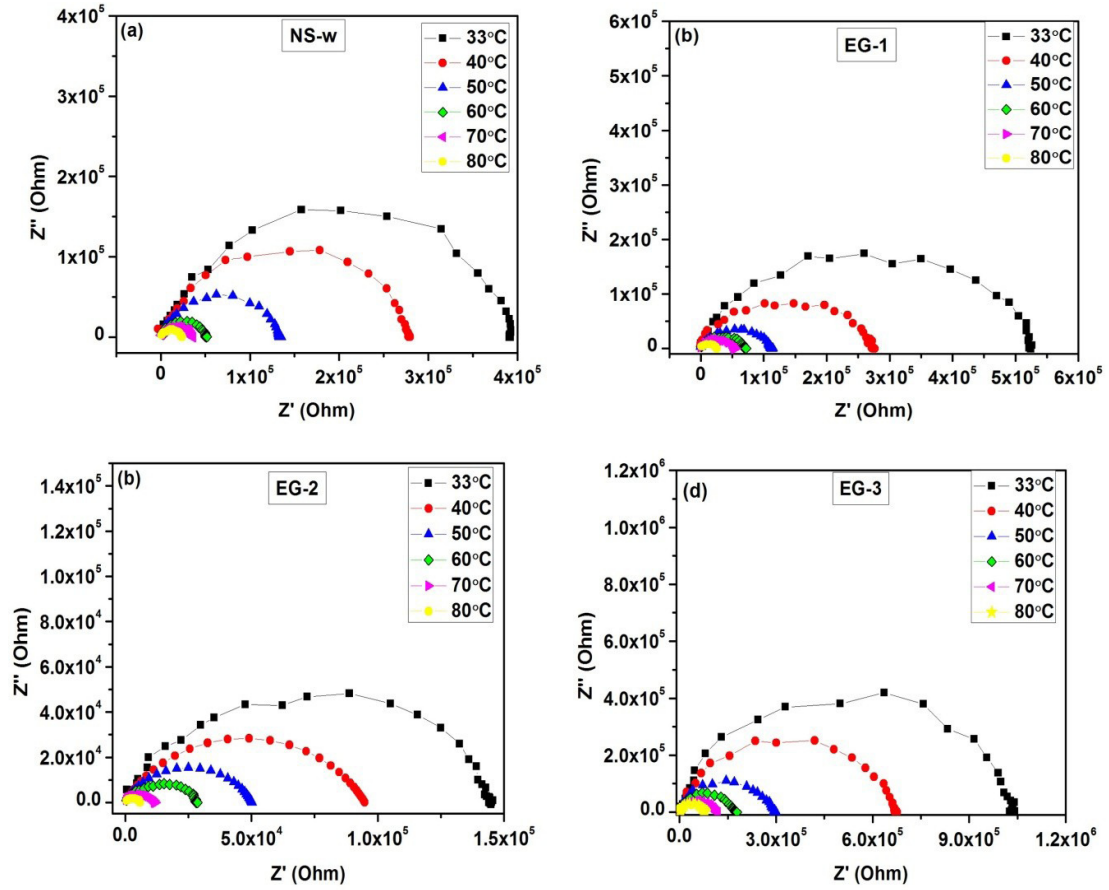

Figure 4.5: Nyquist plot for the samples (a) NS-W, (b) EG-1, (c) EG-2 and (d) EG-3

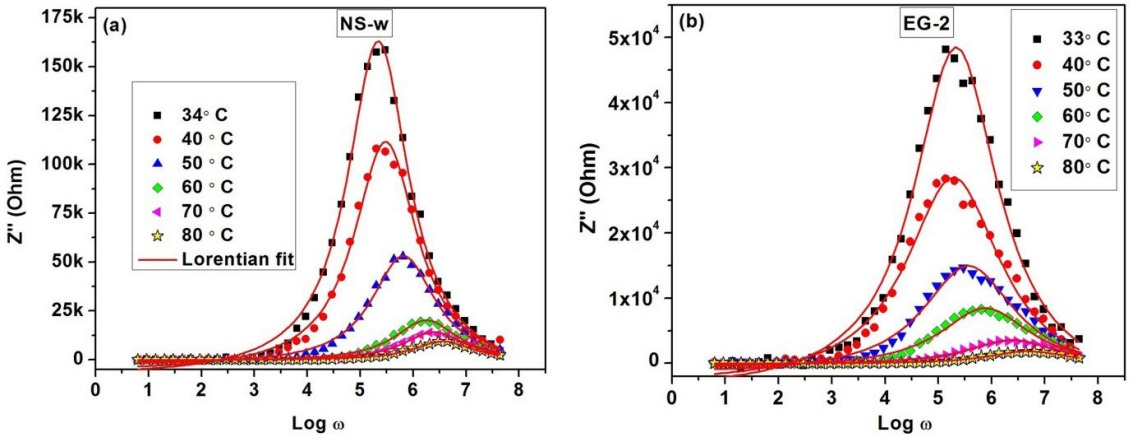

Figure 4.6: Variation of Z'' with frequency and temperature for (a) NS-W and (b) EG-2

If the applied AC frequency is higher than hopping frequency the conductivity suddenly increases. As the frequency increases the localized states also (defects) increases, so that the conductivity reaches maximum at higher frequencies. This indicates Conductivity originates from hopping of charge carriers between two sites [Suresh et al., 2015]. DC conductivity of the synthesized materials was detected from the plateau region of the conductance plot as in Table 4.4. It exhibits lower electrical conductivity in EG-3 with respect to other samples. The least electrical conductivity was observed in EG-3, the higher conductivity was observed in EG-2. It is noticed that, EG-3 has the lowest particle size and EG-2 has the highest particle size among all the samples. It may be due to quantum confinement effect.

Table 4.4: DC Conductivity of CuO nanoflakes EG (0), EG (0.05), EG (0.1), (EG (0.2)

Temperature ° C	Conductivity in S/cm			
	NS-W	EG-1	EG-2	EG-3
33	3.40 E-07	1.49 E-07	6.08 E-07	9.37 E-08
40	4.75 E-07	2.82 E-07	9.23 E-07	1.44 E-07
50	9.84 E-07	6.87 E-07	1.72 E-06	3.27 E-07
60	2.56 E-06	1.09 E-06	3.10 E-06	5.48 E-07
70	3.65 E-06	1.43 E-06	7.70 E-06	8.28 E-07
80	5.52 E-06	3.07 E-06	1.52 E-05	1.22 E-06

At high frequency, conductance spectra merge irrespective of temperature. Total conductivity due to hopping mechanism is governed by johnschr's power law [Daries Bella et al., 2015].

$$\sigma_{total} = \sigma_{dc} + \sigma_{ac} = \sigma_{dc} + A\omega^{s}. \quad \text{---------- (3.5)}$$

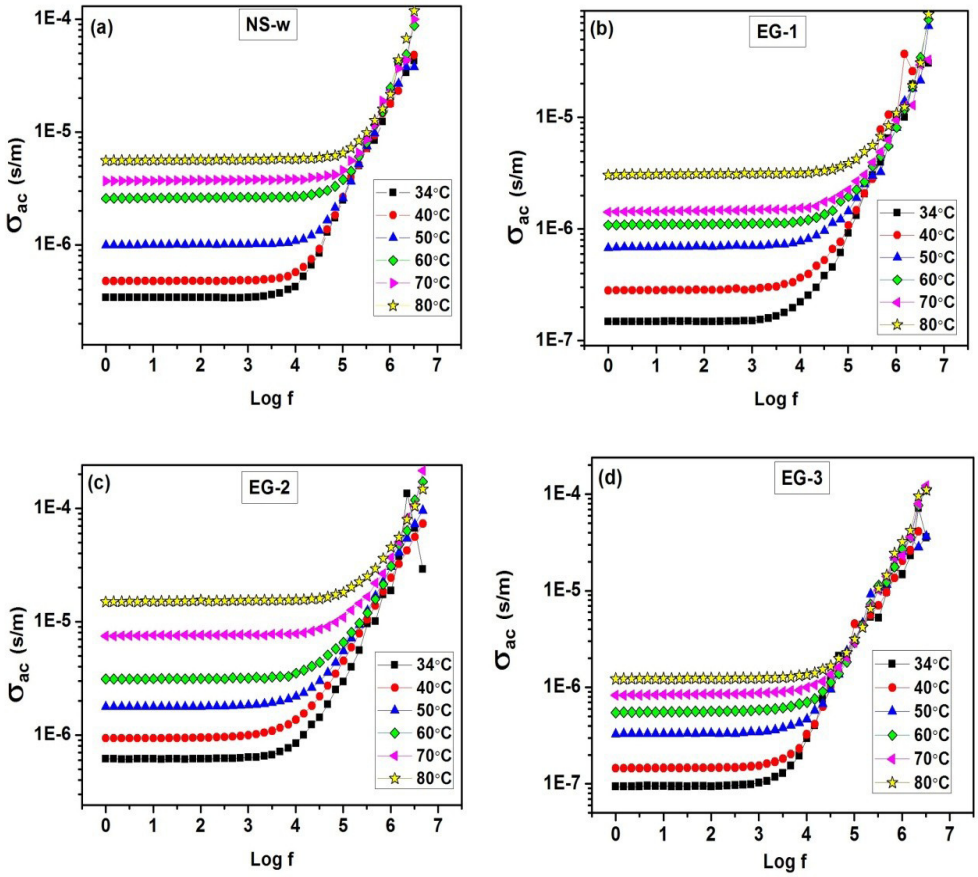

Figure 4.7: Variation of AC conductivity with frequency and temperature for (a) NS-W, (b) EG-1, (c) EG-2 and (d) EG -3

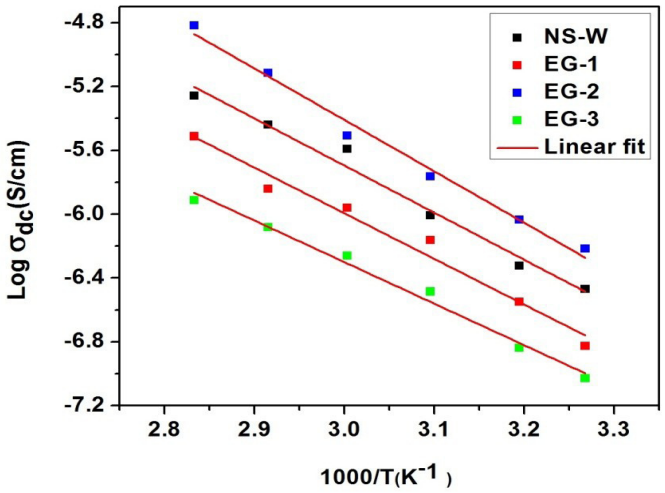

Figure 4.8: Arrhenius plot of dc conductivity for the samples NS-W, EG-1, EG-2 and EG-3

A is temperature dependent constant. S is frequency exponent. Fig. 4.8 shows Arrhenius plot i.e the variation of dc conductivity with temperature. The dc conductivity of the Copper oxide nanoflakes increases with the increase in temperature which is due to the electrical conduction is thermally activated. The variation is linear with temperature and it's obeying Arrhenius relation [Karthick et al., 2014]

$$\sigma_{dc} = \sigma_0 \exp\left(\frac{-E_a}{K_B T}\right) \quad \text{---------- (3.5)}$$

where, σ_o = pre-exponential factor, E_a is activation energy and K_B= Boltzmann constant. Activation energy represents a sum of energy required for vacancy creation and motion of carriers into vacancies [Das et al., 2007]. The activation energy is 0.59, 0.57, 0.63 and 0.51 eV for the samples NS-W, EG-1, EG-2 and EG-3 respectively.

4.3.5.3 Dielectric studies

Figure 4.9 (a) and (c) shows the variation of dielectric constant with frequency at various temperatures for NS-W and EG-2 respectively. Variation of dielectric constant with the concentration of EG follows the same trend as that of conductivity studies. i.e., the sample EG-2 which has highest conductivity and it possess highest dielectric constant. The dielectric constant increases with the decrease of frequency for both the samples as shown in Fig. 4.9. The dielectric constant is larger at low frequencies and at high temperatures, which is normal in oxides and this cannot be taken as an indication for spontaneous polarization [Vijay kumar et al., 2009]. All the polarizations are active in the lower frequencies and the dielectric constant is high in this regions. Frequency increases the polarizations becomes inactive step by step and at higher frequencies dielectric constant has the constant value. The dielectric constant increases with the increase in temperature as shown in Fig.4.9. The reason for this increase in dielectric constant is explained by many authors on the basis of the phenomenon that as the temperature increases, the dipoles relatively become free and they respond to the applied electric field and orient themselves. Consequently the orientation polarization increased

and hence dielectric constant also increases with the increase in temperature [Suresh et al., 2015, Suman et al., 2005]. But Deepthi et al., discussed, for semiconductors the increment of conduction electron and holes density creates additional dipole moment and so increment of dielectric constant [Deepthi et al., 2013].

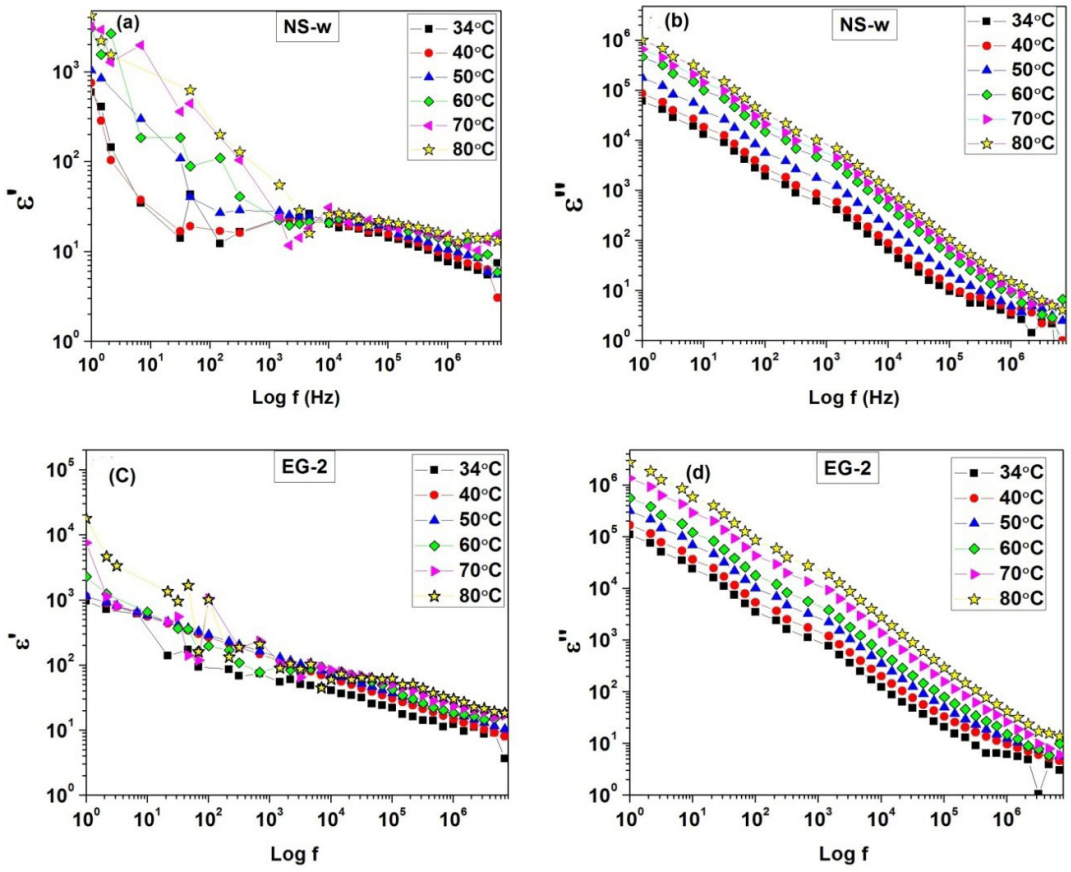

Figure 4.9 (a&b): Variation of ε′ and ε″ with frequency and temperature for NS-W(c&d): Variation of ε′ and ε″ with frequency and temperature for EG-2

In the present case, dielectric constant of both the samples decreases upto 100 KHz after that it reaches the frequency independent nature. NS-W has dielectric constant value in the range 10^2 to 10^3 and EG-2 lies in the range 10^3 to 10^4 at low frequencies. This is comparable with the values reported by Sarkar et al., 2006 and Deepthi et al., 2013. From that they concluded, CuO is a giant dielectric material. These giant dielectric properties may be due to result of array of semiconducting grains and insulation boundary barriers [Sarkar et al., 2006. Deepthi et al., 2013].

Fig. 4.9 (b) and (d) shows the dielectric loss graph of NS-W and EG-2 at different frequencies and at various temperatures. It is noticed that for both the samples having high dielectric loss at low frequencies and the dielectric loss linearly decreases with the increase in frequency. Dielectric loss occurs due to the absorption current which is produced by in- homogeneities, defects and space charge formation. It may the reason for more dielectric loss and also the reason for higher conductivity behavior. Dielectric loss value lies in the range 10^5 to 10^6 for the measured temperatures. There is no dielectric loss peak observed in the working region.

4.4 Conclusions

Copper oxide nanoflakes were synthesized using simple wet chemical method using ethylene glycol as surfactant with three different concentrations. XRD results confirmed the crystalline nature of the materials and confirmed the monoclinic structure of copper oxide. The Crystallite sizes are 21, 23, 25 and 16 nm for NS-W, EG-1, EG-2 and EG-3 respectively. FTIR spectrum confirms the presence of CuO phase groups for all the samples. SEM images elucidated the nanoflakes morphology of synthesized Copper oxide materials. DRS spectrum explains the absorption range of the synthesized material is in the visible region and band gap of the materials also calculated. Structural and electrical properties confirmed that effective changes were produced in the material due to the change of the concentration of Ethylene glycol. Impedance studies shown that, sample EG-2 which was prepared by adding equal molarity of ethylene glycol with the cupric nitrate (0.1: 0.1) enhances the conductivity and dielectric properties. At the same time, if we increase the molarity of surfactant more than nitrate salt, it decreases the electrical properties. Dielectric studies revealed that synthesized materials act as giant dielectric materials and it can be used in microelectronic industries.

CHAPTER - V

SYNTHESIS AND CHARACTERIZATION OF CuO NANOSTRUCTURES USING PEG -400 AS SURFACTANT

This chapter deals with the properties of CuO nanostructures synthesized using Poly Ethylene Glycol (PEG-400) as a surfactant

5.1. Properties of PEG-400

- PEG 400 is a low-molecular-weight grade of polyethylene glycol.
- It is a clear, colorless, viscous liquid.
- Due in part to its low toxicity, PEG 400 is widely used in a variety of pharmaceutical formulations.
- PEG 400 is soluble in water, acetone, alcohols, benzene, glycerin, glycols, and aromatic hydrocarbons, and is slightly soluble in aliphatic hydrocarbons.
- Density : 1.13 g/cm³
- Formula : $C_{2n}H_{4n+2}O_{n+1}$, n=8.2 to 9.1
- Melting point : 4 to 8 °C (39 to 46 °F; 277 to 281 K)
- Viscosity : 90.0 cSt at 25 °C, 7.3 cSt at 99 °C
- Molar mass : 380-420 g/mol
- Molecular structure:

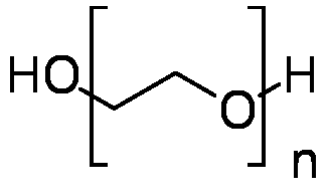

5.2. Synthesis of CuO nanostructures using PEG-400 surfactant

CuO nanostructures were synthesized by wet chemical method using copper nitrate (Cu $(NO_3)_2.3H_2O$) and sodium hydroxide. First precursor was dissolved in 100 ml deionized water to form 0.1 M concentration solution. PEG-400 of (0.05M, 0.1M and 0.2M) was added with copper nitrate solution and allowed to stir for 30 minutes. Then NaOH solution (0.2 M) was slowly dropped under vigorous stirring until the pH reaches 11. During this time blue precipitation was formed and turn into Black color. The precipitation was repeatedly washed by deionized water and absolute ethanol for several times till the pH reaches 7. Subsequently, the washed precipitates were dried at room temperature for 24 hrs. Finally, the dried material is calcinide at 120 °C for 10 hrs. Thus three samples were synthesized using PEG surfactant and coded as PEG-1(0.05 M of PEG), PEG-2 (0.1M) and PEG-3 (0.2M).

5.3. Characterizations

5.3.1 XRD Analysis

The typical XRD pattern of the CuO nanomaterials was shown in Fig.5.1. The peak positions of the sample exhibited the monoclinic structure of CuO. No other impurity peak was observed in the XRD pattern, showing the single phase sample formation. The crystalline size was calculated using the Scherrer's formula given eqn. no. (4.1) Crystallite size calculated by the Scherrer's formula and Lattice parameters of unit cell calculated using 'UNITCELL' software were shown in Table 5.1. These values are in good agreement with the standard values reported by the JCPDS Card No 80-1916. Table 5.1 shows that Crystallite size decreases with the increase of concentration of surfactant. This shows that PEG-400 can reduce the particle size at the current experimental conditions.

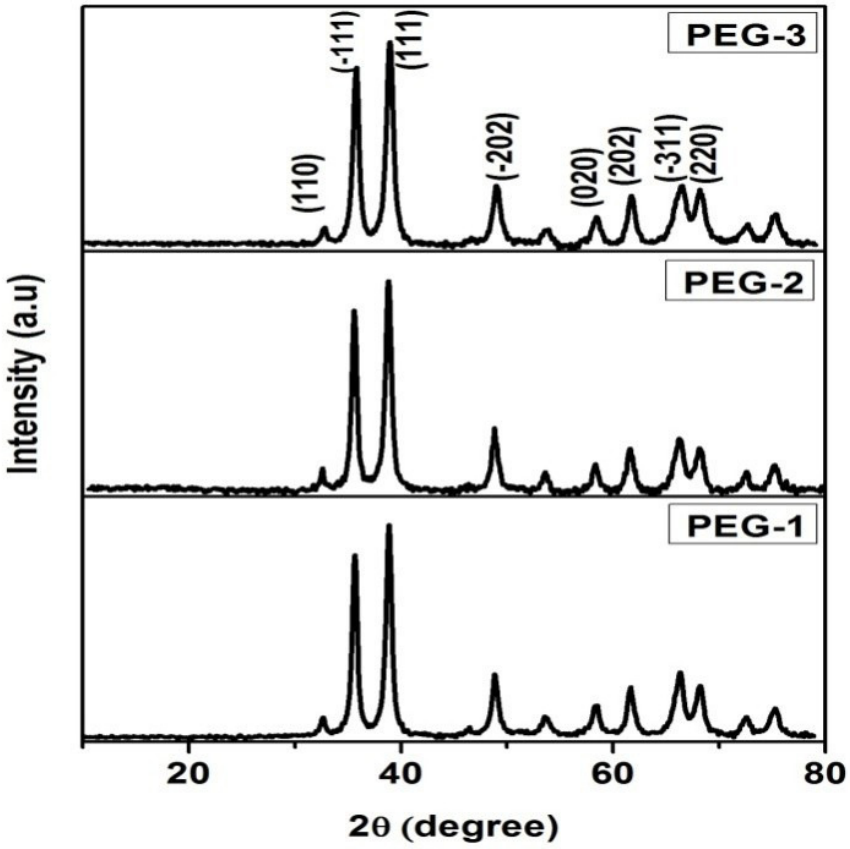

Figure 5.1: XRD patterns of the CuO nanostructures using PEG surfactant

Table 5.1: Crystallographic parameters of the CuO nanostructures synthesized using PEG surfactant

Materials	a	b	c	Beta (degree)	Cell Volume $(Å)^3$	Crystallite size (D) nm
	(Å)					
PEG-1	4.26	3.50	5.92	99.77	87.15	40.4
PEG-2	4.25	3.49	5.95	100.01	86.89	37.3
PEG-3	4.25	3.47	5.923	99.86	85.97	35.7

5.3.2. FTIR analysis

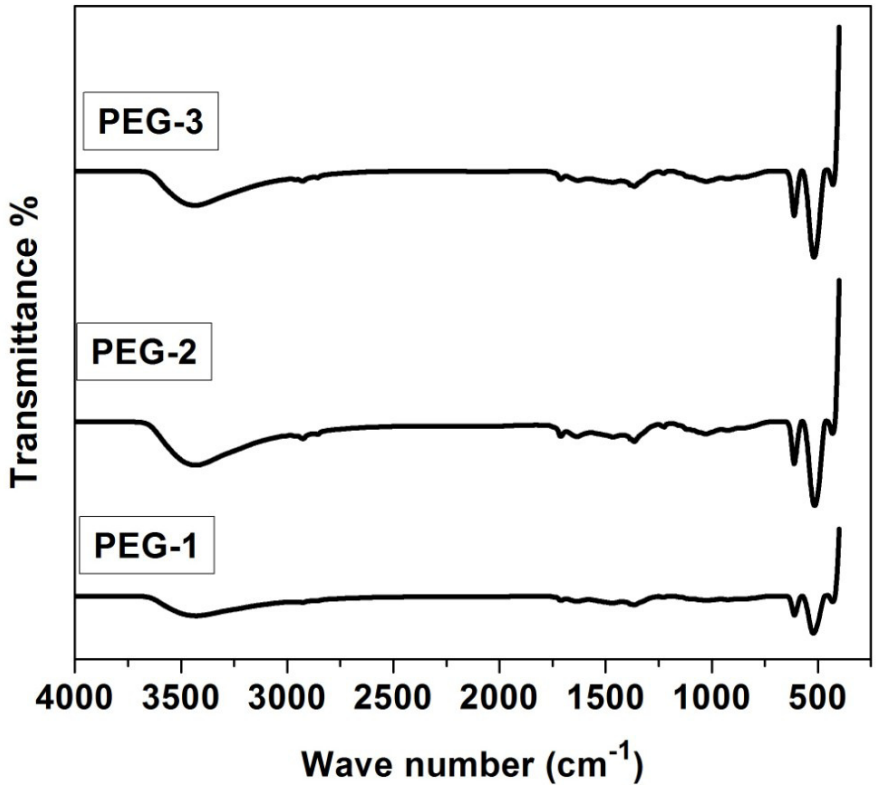

Figure 5.2: FTIR spectrum of the CuO nanostructures using PEG surfactant

Fig. 5.2 displays the FTIR spectrum and Table 5.2 shows the corresponding peaks assigned for synthesized Copper oxide samples using different concentration of surfactant. Three characteristic bands observed around 430 cm^{-1}, 520 cm^{-1}, 610 cm^{-1} associated with Cu-O stretching modes. Some low intense absorption peaks noticed in the region of 1200 to 1700cm^{-1} may be attributed to O–H bending vibrations combined with copper atoms [Dubal et al., 2010]. The broad peak observed at 3435 is assigned to O-H which due to physorption of water molecule in the surface of the material. Formation of Copper oxide compound is confirmed by FTIR study.

Table 5.2 : FTIR peaks for the CuO nanostructures PEG-1, PEG-2 and PEG-3

Wave Number (cm^{-1})			Peaks assigned
PEG-1	**PEG-2**	**PEG-3**	
430	429	431	Cu-O
521	519	516	Cu-O
611	612	612	Cu-O
3435	3434	3443	O-H bending

5.3.3. SEM Analysis

SEM photographs of the CuO nanostructures PEG-1, PEG-2, and PEG-3 were shown in Fig.5.3 (a), (b) and (C) respectively. Fig.4.3 depicts that PEG-1 have the leaf like morphology, PEG-2 have flake like and PEG-3 have flake and rod mixed morphology. High concentration of PEG splits the CuO leaves and CuO nanorods was formed. This SEM images confirms that various concentration of PEG changes the morphology and particle size.

5.3.4. UV-Vis DRS spectrum analysis

Fig. 5.4 shows UV-Vis diffuse reflectance spectra of PEG-1, PEG-2 and PEG-3. The CuO nanostructures have shown absorption spectrum in the visible region from 400-800 nm regions with the maximum point at 528, 441 and 440 nm for the samples PEG-1, PEG-2 and PEG-3 respectively. The absorption occurs in the visible region, so the synthesized CuO materials can be used as sunlight photo-catalysts. From the Fig.5.4 (a), it is noticed that the spectrum is red shifted as the concentration of PEG increases. α value was calculated according to Kubelka-Munk theory to the synthesized materials. Fig 5.4(b) shows the plot of $(\alpha h\upsilon)^2$ Vs hυ. Extrapolation of the linear portion of curve cuts at X-axis is taken as the band gap. The band gap of the materials was calculated as 1.68, 2.00, 2.23 eV for PEG-1, PEG-2 and PEG-3 respectively. It is observed that the band gap of the materials increases with the

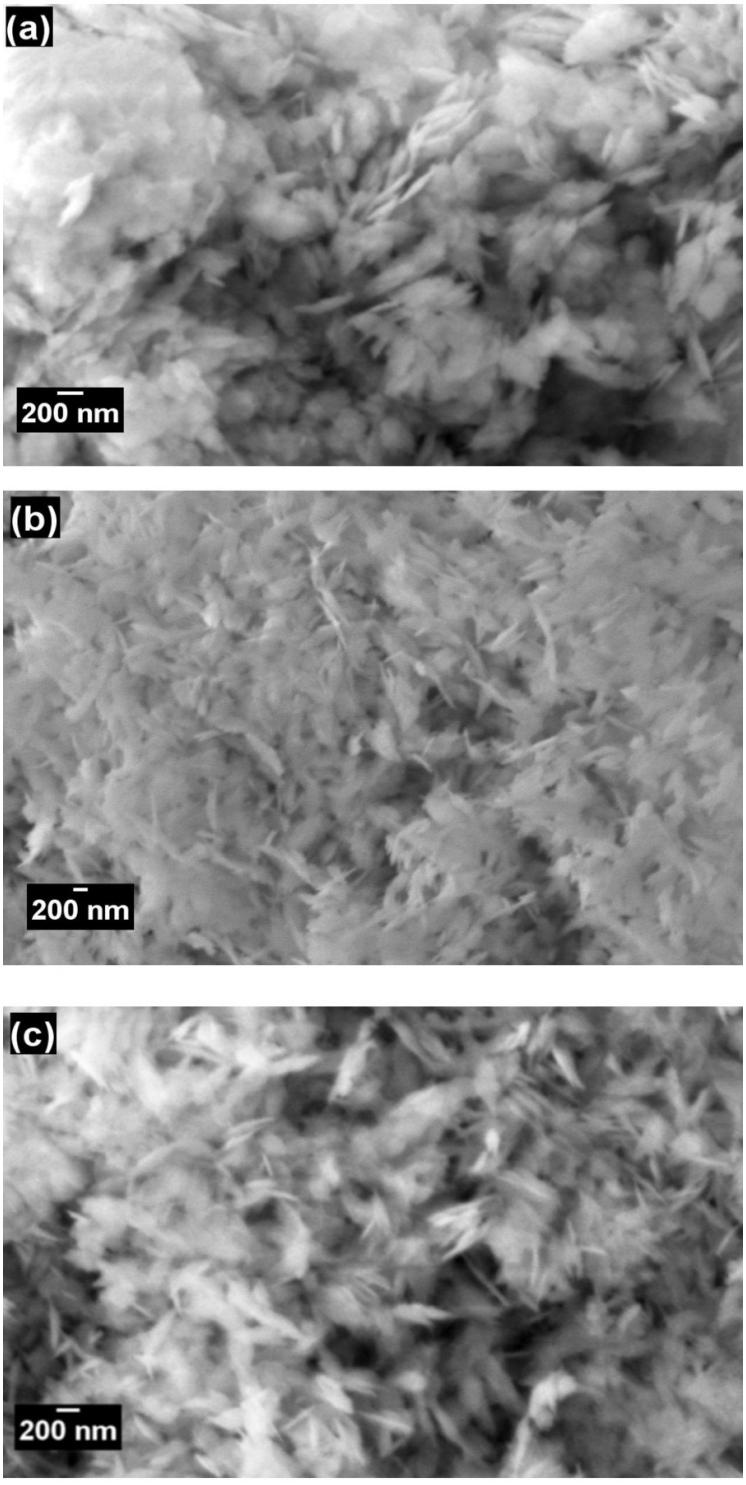

Figure 5.3: SEM images of the CuO nanostructures (a) PEG-1 (b) PEG-2 (c) PEG-3

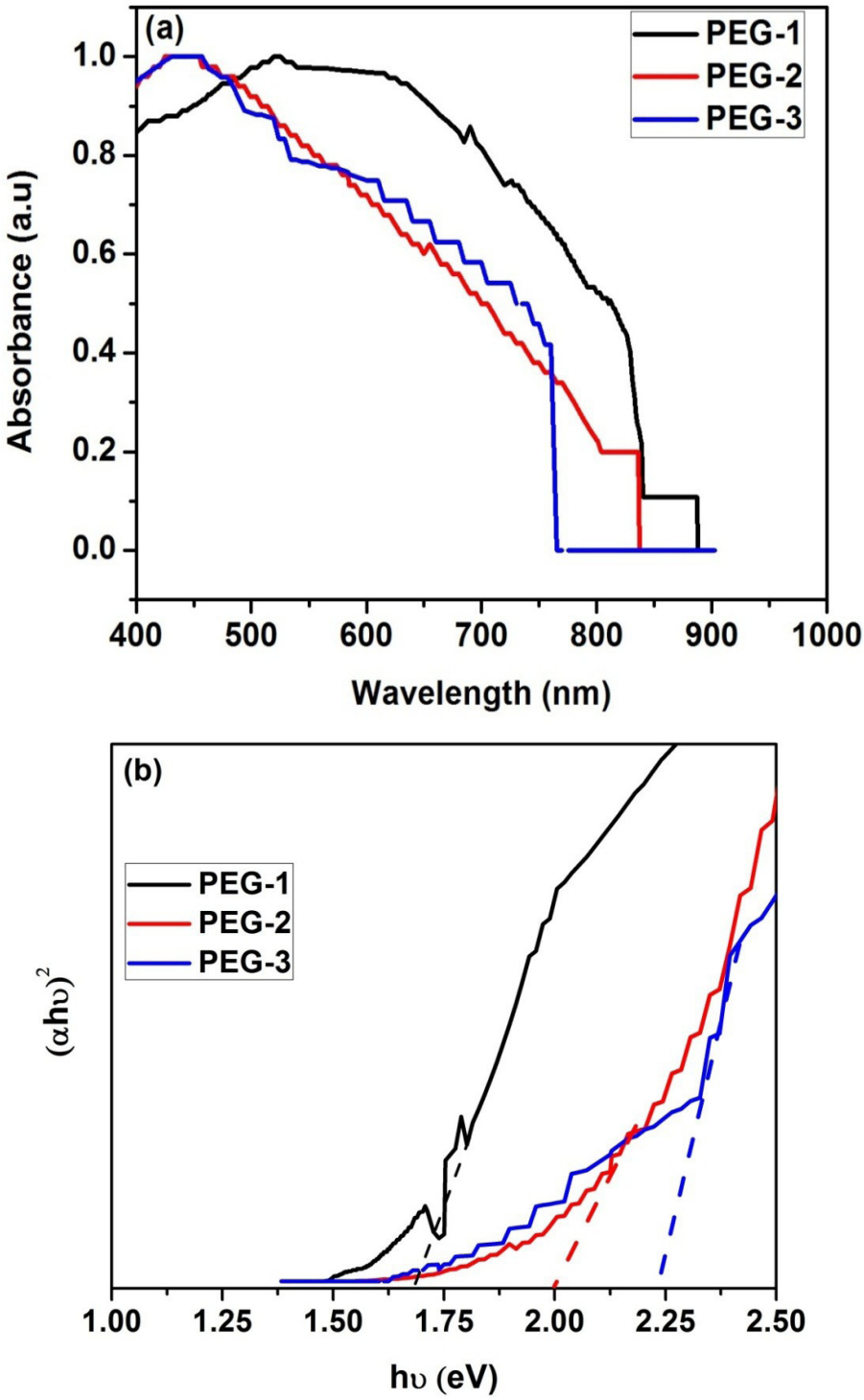

Figure 5:4 (a) UV- Vis Diffuse reflectance absorption spectra (b) Plot of plot of $(\alpha h\nu)^2$ Vs hν for the samples PEG-1, PEG-2, PEG-3

concentration of the PEG whereas the crystallite size of the materials gets decreased. The increase in band gap value may due to the quantum confinement effect [Mallick & Sahu, 2012]. The word confinement means to confine the motion of randomly moving electron to restrict its motion in specific energy levels (discreteness). The decrease in confining dimension makes the energy levels discrete and this increases or widen up the band gap and ultimately the band gap energy also increases

5.3.5. Electrical Properties

5.3.5.1 Impedance analysis

Fig. 5.5 (a-c) shows the Nyquist plot (real part of impedance vs imaginary part of impedance) of the CuO nanomaterials PEG-1, PEG-2 and PEG-3 at various temperatures. For all the three samples, the impedance spectrum is characterized by the appearance of a single semicircular shape whose radii decreases with increase in temperature. Single semicircle shape predicts that the grain properties are predominant in the material [Sen et al., 2006]. All the samples exhibit depressed semicircle due to the distribution of relaxation time [Tanmaya et al., 2014]. The intercepts of the semicircular arc with the real axis (Z') give us an estimate of bulk resistance (R_b) of the material. It has been observed that bulk resistance decreases with increase in temperature for all the three samples. The result interpreted the negative temperature coefficient of resistance behavior of a semiconductor [Ashok kumar et al., 2006].

Fig. 5.6 represents the imaginary part Z'' with various frequencies (impedance loss spectra) at different temperatures for higher conductivity sample PEG-1. Impedance loss spectrum is characterized by the appearance of peaks at a particular frequency for each temperature. The appearance of peak in the loss spectrum is an indication of the presence of electrical relaxation in the material at the measured temperature range (<80°C).

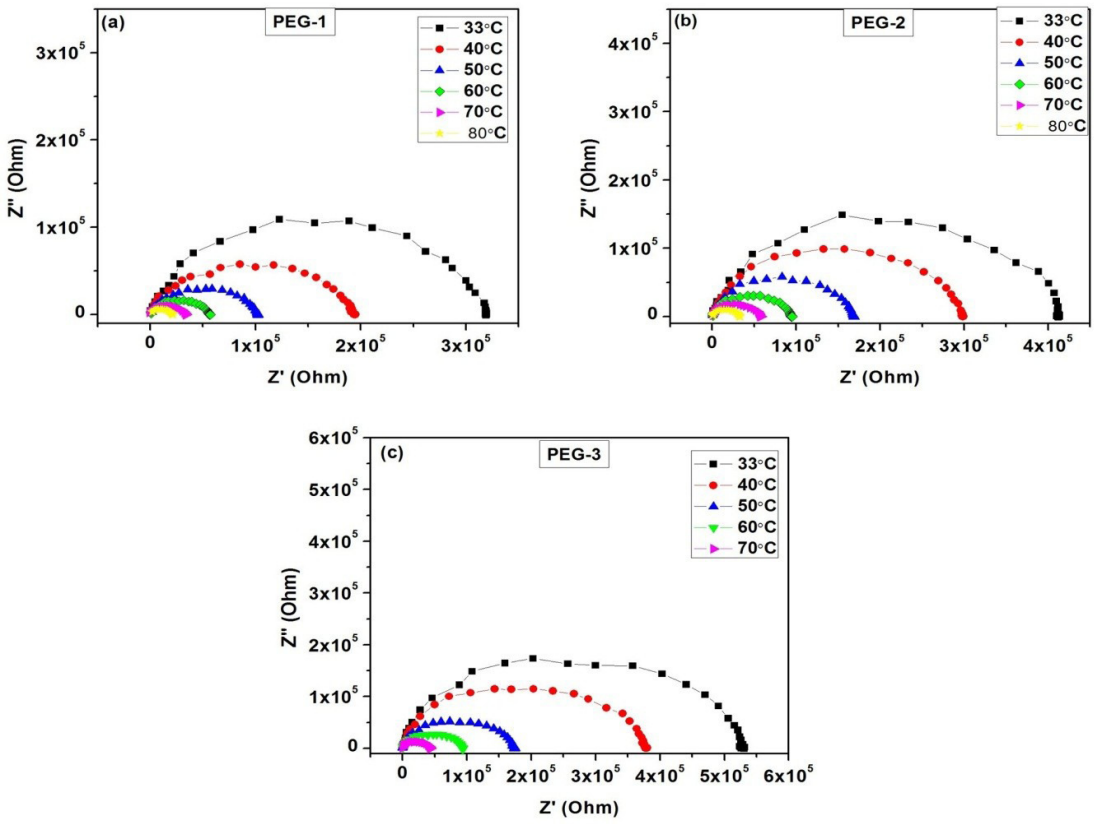

Figure 5.5: Nyquist plot for the CuO nanostructures

(a) PEG-1, (b) PEG-2 and (c) PEG-3

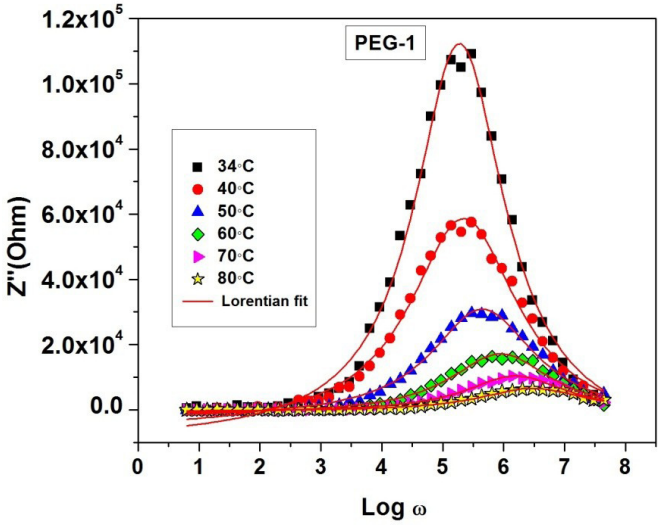

Figure 5.6: Variation of Z'' with frequency and temperature for PEG-1

For both the samples, peaks are asymmetric and their position shifting towards the higher frequency side with the increase in temperature. The shifting of peaks towards high frequency side is attributed to a phenomenon associated with a minimum capacitive effect [Ashok kumar et al., 2006]. The impedance loss spectra has been used to evaluate the relaxation time (τ) of the electrical phenomena in the material at different temperatures in accordance with the relation $\omega_{max}\tau = 1$. Relaxation time was calculated and given in Table 5.3 for PEG-1. The relaxation time is steadily increasing with respect to the temperature.

Table 5.3: Relaxation time for PEG-1 at various temperatures

Temperature(° C)	Relaxation time (μS)
	PEG-1
34	5.30
40	4.53
50	2.23
60	1.12
70	6.34
80	3.38

5.3.5.2 AC and DC conductivity.

Fig.5.7 shows the variation of ac conductivity (σ_{ac}) as a function of frequency at different temperatures for PEG-1, PEG-2 and PEG-3. The conductivity spectrum shows low frequency plateau and high frequency dispersion with the change in slope. In the low frequency region, conductivity shows frequency independent behavior and it is sensitive in the high-frequency region. For all the temperatures, conductivity becomes narrow at high frequencies and the patterns merge into a single curve. The frequency at which

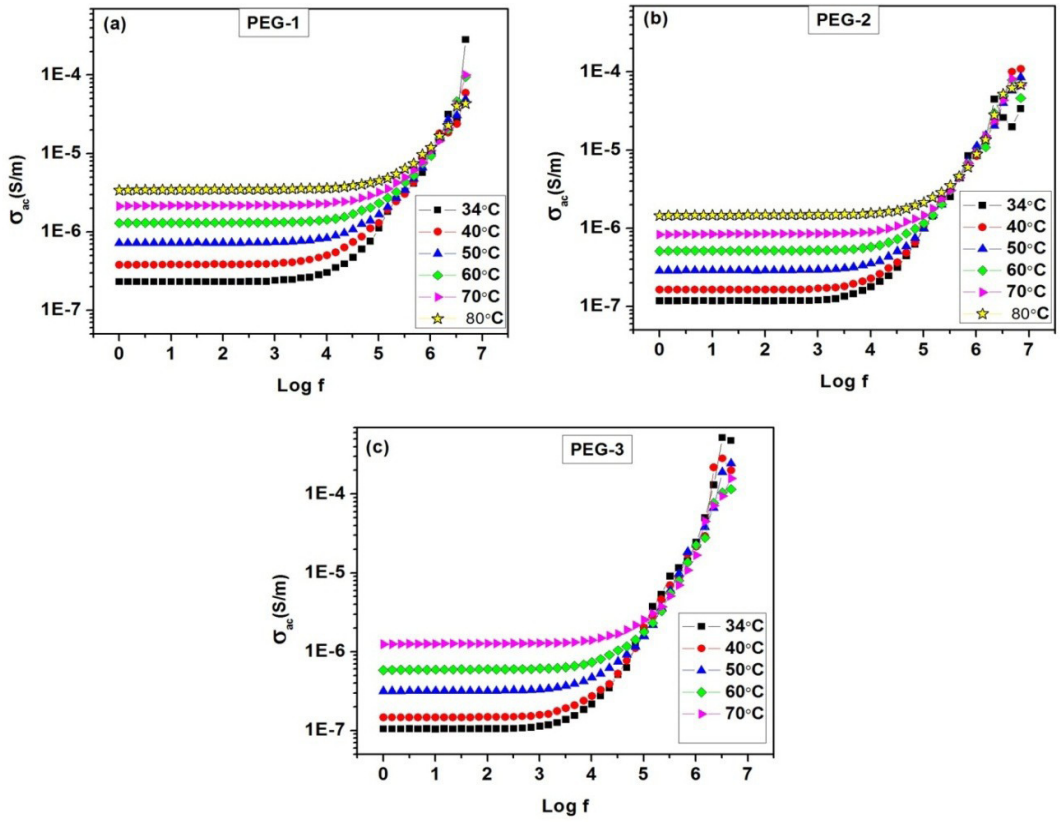

Figure 5.7: Variation of AC conductivity with frequency and temperature for (a) PEG-1, (b) PEG-2 and (c) PEG-3

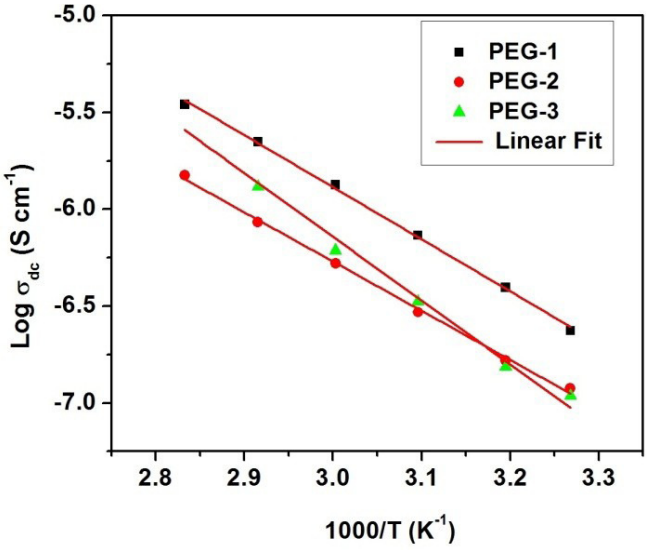

Figure 5.8: Arrhenius plot of dc conductivity for the samples PEG-1, PEG-2 and PEG-3

change in slope of the pattern occurs is known as hopping frequency (ω_p). The patterns also explained that, the hopping frequency shifts towards higher frequency side with increasing temperature.

These results suggest that electrical conduction in the material takes place via hopping mechanism governed by the Jonscher's universal power law: $\sigma_{ac} = \sigma_{dc} + A^{\omega}$, where A is a thermally activated constant depending upon temperature.

Table 5.4: Dc conductivity of the samples PEG-1, PEG-2 and PEG-3

Temperature °C	Conductivity (S/cm)		
	PEG-1	PEG-2	PEG-3
34	2.36 E-07	1.19 E-07	1.09 E-07
40	3.95 E-07	1.66 E-07	1.54 E-07
50	7.34 E-07	2.94 E-07	3.35 E-07
60	1.34 E-06	5.25 E-07	6.13 E-07
70	2.23 E-06	8.60 E-07	1.31 E-06
80	3.48 E-06	1.50 E-06	-

DC conductivity of the samples were observed from the conductance plot and shown in Table 5.4. Table shows that, dc conductivity decreases with increase in concentration of PEG at room temperature. As the temperature increases, conductivity increases linearly for all the samples. Conductivity of PEG-3 is high in the range 40°C- 80°C when compared with PEG-2. The Results show that, after 40°C thermally activated carriers increased in PEG-3.

Fig. 5.8 shows the variation of dc conductivity with respect to the temperature. For all the samples Fig. 5.8 shows the linear response and it can be explained by a thermally activated transport process of Arrhenius type. The nature of these plots follows

the Arrhenius relation. Activation energy was calculated from Arrhenius plot and the values are 0.65, 0.50, 0.53 eV for PEG -1, PEG-2 and PEG-3 respectively.

5.3.5.3 Dielectric properties.

Fig. 5.9 (a) and (b) shows the dielectric graph of PEG-1 for various frequencies at different temperatures. Dielectric constant decreases with respect to the frequency and increases with the temperature. This is due to the fact that at lower frequencies the four polarizations namely space charge, dipolar, ionic and electronic polarization are contributing, whereas at higher frequencies only the electronic and ionic polarizations are active. Broadly speaking, the graph exemplifies the fact that both the dielectric constant and dielectric loss are inversely proportional to the frequency. Due to interfacial polarization, the dielectric constant decreases and reaches the constant value with the increase in frequency. On the other hand ε increases with temperature. The dipoles become comparatively free with increase in temperature and they respond to the applied electric field. Thus polarization increases and hence dielectric constant increases with the increase in temperature.

At low frequencies the dielectric constant lies in the range 10^2- 10^3 for various temperatures. Dielectric constant (ε) decreases linearly in the frequency region 1 Hz to 1 KHz and above 1 KHz it decreases slowly. Dielectric loss also linearly decreases with frequency and increases with temperature. At low frequencies, ε'' is in the range 10^5 to 10^6 for the measured temperatures.

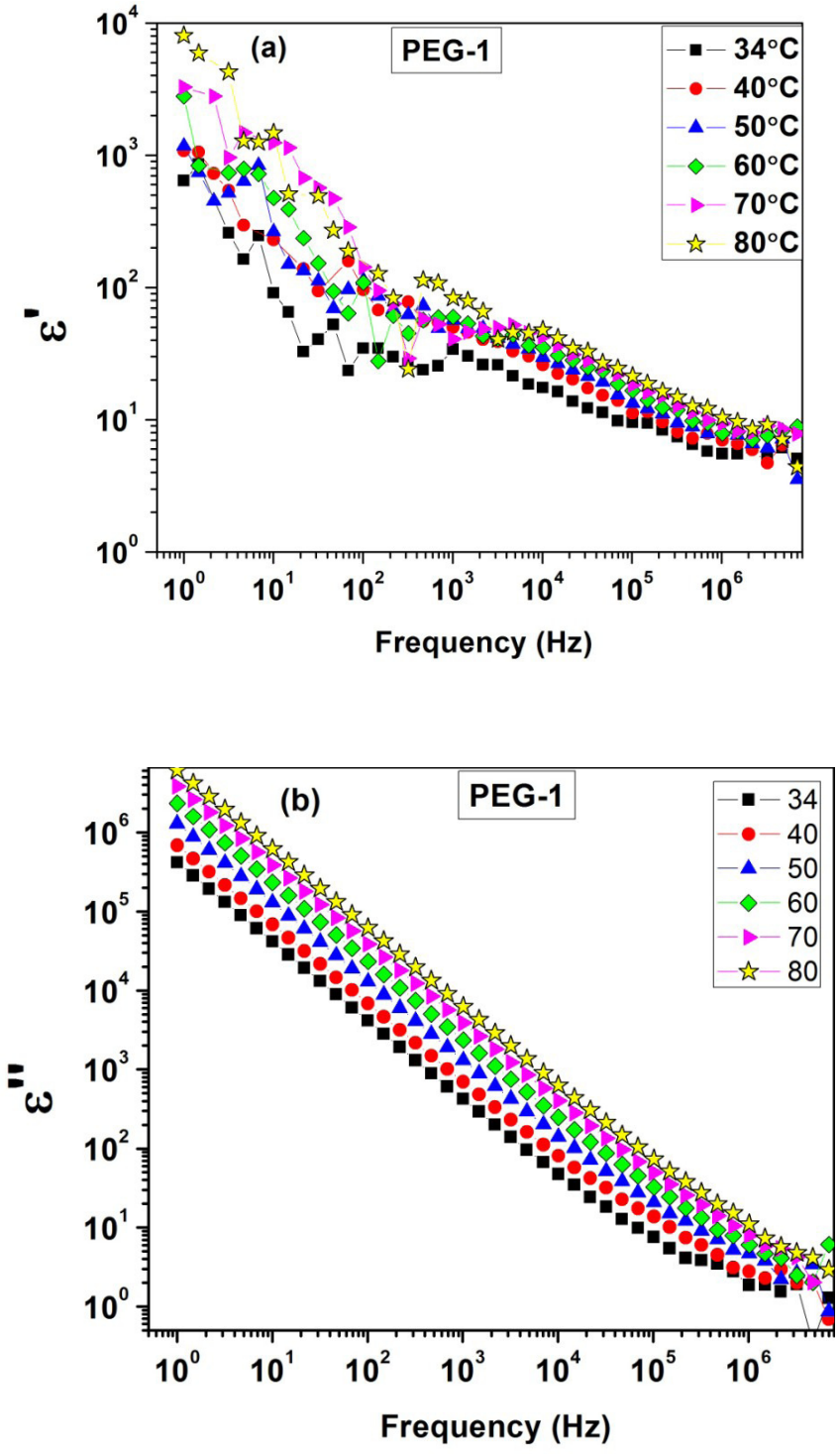

Figure 5.9: Variation of (a) Dielectric constant and (b) Dielectric loss with frequency and temperature for PEG-1

5.4. Conclusions

Copper oxide nanomaterials have been synthesized by wet chemical method using PEG-400 surfactant. Using different concentrations of surfactant three samples were synthesized named as PEG-1 PEG-2 and PEG-3. Here the XRD confirms the monoclinic structure and phase purity of the materials. The calculated crystallite sizes are 40.4, 37.3 and 35.7 nm for PEG-1 PEG-2 and PEG-3 respectively. The crystallite size decreases with the increase in concentration of surfactant. FTIR confirms the formation of CuO and also the purity of the materials. SEM images elucidated the morphological changes of the materials due to PEG. Diffuse reflection spectrum shows the absorption of the materials is in the visible range. The band gap values are 1.68, 2.0, 2.23 eV for PEG-1 PEG-2 and PEG-3 respectively. DC conductivity decreases with the increase in concentration of PEG-400. For the high conductivity sample PEG-1, relaxation time and dielectric properties were studied.

CHAPTER - VII

SYNTHESIS AND CHARACTERIZATION OF CuO NANOSTRUCTURES USING CTAB SURFACTANT

7.1. Properties of the CTAB

CTAB	:	Cetyl trimethyl ammonium bromide
Chemical formula	:	$C_{19}H_{42}BrN$
Molar mass	:	364.45 g/mol
Appearance	:	white powder
Melting point	:	237 to 243 °C (459 to 469 °F; 510 to 516 K) (decomposes)
Type	:	cationic detergent
Solubility	:	Water soluble and readily soluble in alcohol

Molecular structure

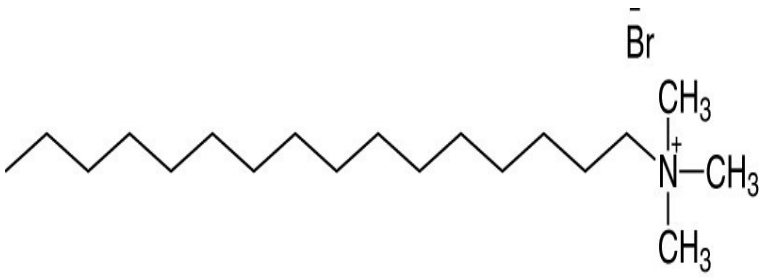

7.2. Synthesis of copper oxide nanostructures

Copper nitrate solution of 0.1 M and NaOH solution of 0.2 M were separately prepared using deionized water. CTAB surfactant was mixed with copper nitrate solution and allowed to stir with the warm heat until it dissolves. After that, freshly prepared sodium hydroxide solution was added drop by drop with the continuous stirring until the pH becomes 11. During this time, dark blue precipitation was formed and it turned into black. Then, the black precipitation was washed several times by deionized water and ethanol using suction funnel. Washed samples were dried at room temperature for a day. Then it was kept in oven at 120° C for 10 hrs. Following the procedure said above, four

samples were synthesized using different concentrations of the surfactant such as 0.001 M, 0.005 M, 0.01 M and 0.05 M. The samples are named as CT-1, CT -2, CT-3 and CT-4.

7.3. Characterizations

7.3.1. XRD analysis

Fig 7.1 shows the XRD patterns of CT-1, CT-2, CT-3 and CT-4. High intense and broad peaks are noticed in the XRD patterns which confirm the nanocrystalline nature of the materials. Assigned peaks belong to the monoclinic crystal system and the peaks are well agreed with the JCPDS card no. 80-1916 except CT-4. It is seen that some extra peaks are present in CT-4 which may due to the excess of surfactant. It is concluded that, CTAB can be used in the wet chemical method of synthesis only up to 0.01 M otherwise impurity peaks are observed. The crystallite size was calculated using the Scherrer's formula and the cell parameters are calculated using the UNIT CELL software and the results are shown in Table 7.1. It described that the crystallite size decreases with the increment of surfactant ratio. CT-1 has the highest crystallite size among the above synthesized samples. This may due to the lower concentration of surfactant.

7.3.2. FTIR analysis

Fig.7.2 (a) shows the FTIR spectrum and Table 7.2 depicts Major FTIR absorption bands and possible assignments of CT-1, CT-2, CT-3 and CT-4. Well defined absorption bands were observed at 427, 511 and 605 cm^{-1} is assigned to the metal – oxygen bonds. The above peak confirms the existence of Cu-O stretching bond in the synthesized materials. The broad band at 3423 $cm^{-1}$is assigned to symmetric vibration of O-H and less intense band at 1632 cm^{-1} is assigned to bending vibration H-

OH which may due to hydration of water molecules [Behrouz Shaabani 2014]. FTIR pattern of CT-4 consists of extra peaks in the region of 680 to 800 cm^{-1} and 3500 cm^{-1} and the achieved peaks are similar to CTAB; it concludes that the sample has residue surfactant.

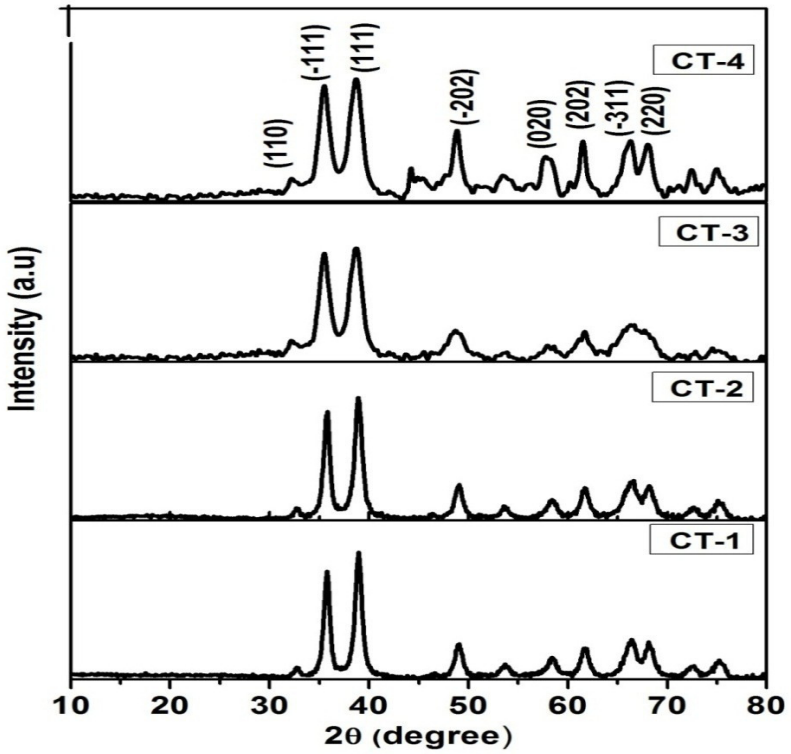

Figure 7.1: XRD pattern of the CuO nanostructures synthesized using CTAB surfactant

Table 7.1: Crystallographic parameters of the synthesized Copper oxide nanostructures

Samples	a	b	c	β	Volume	crystallite
	Å			(degree)	$(Å)^3$	size (nm)
CT-1	4.69	3.41	5.05	99.56	79.63	32.8
CT-2	4.69	3.41	5.06	99.22	79.77	19.2
CT-3	4.70	3.42	5.11	99.64	81.15	17.9
CT-4	4.68	3.44	5.12	99.29	81.60	7.7

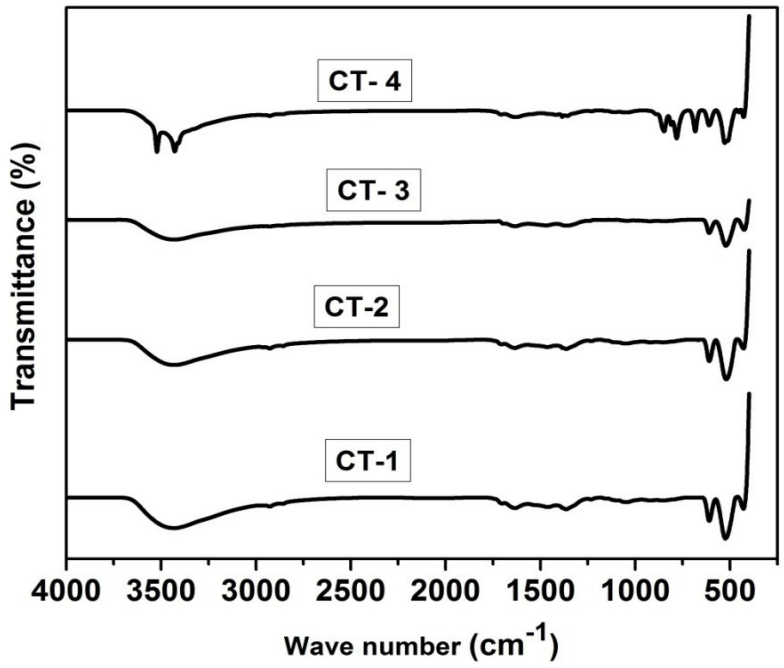

Figure 7.2 (a): FTIR spectra of the CuO nanostructures synthesized using CTAB surfactant

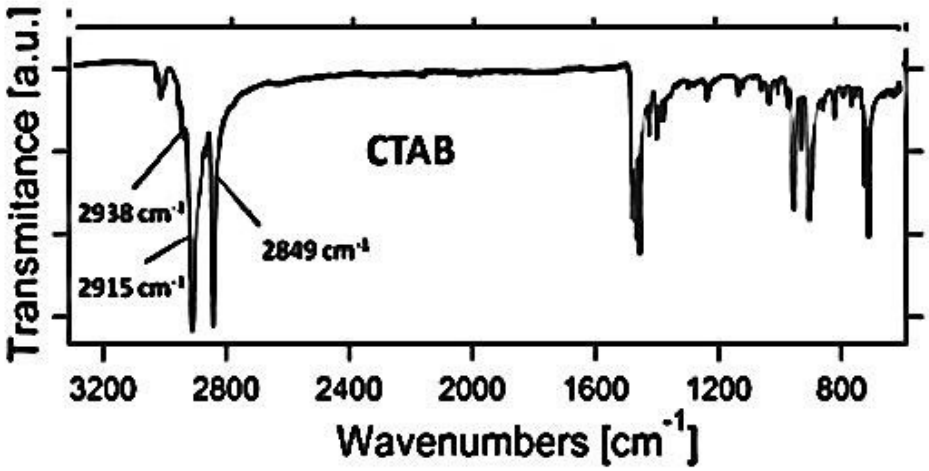

Figure 7.2 (b): FTIR pattern of the CTAB

Table 7.2: FTIR peaks of the CuO nanostructures using CTAB surfactant

Wave number (cm^{-1})				Peaks assigned
CT-1	CT-2	CT-3	CT-4	
429	429	425	439	Cu-O
524	520	521	534	Cu-O
610	610	610	599	Cu-O
3425	3424	3432	3425	O-H bending

7.3.3. Particle size Analyzer

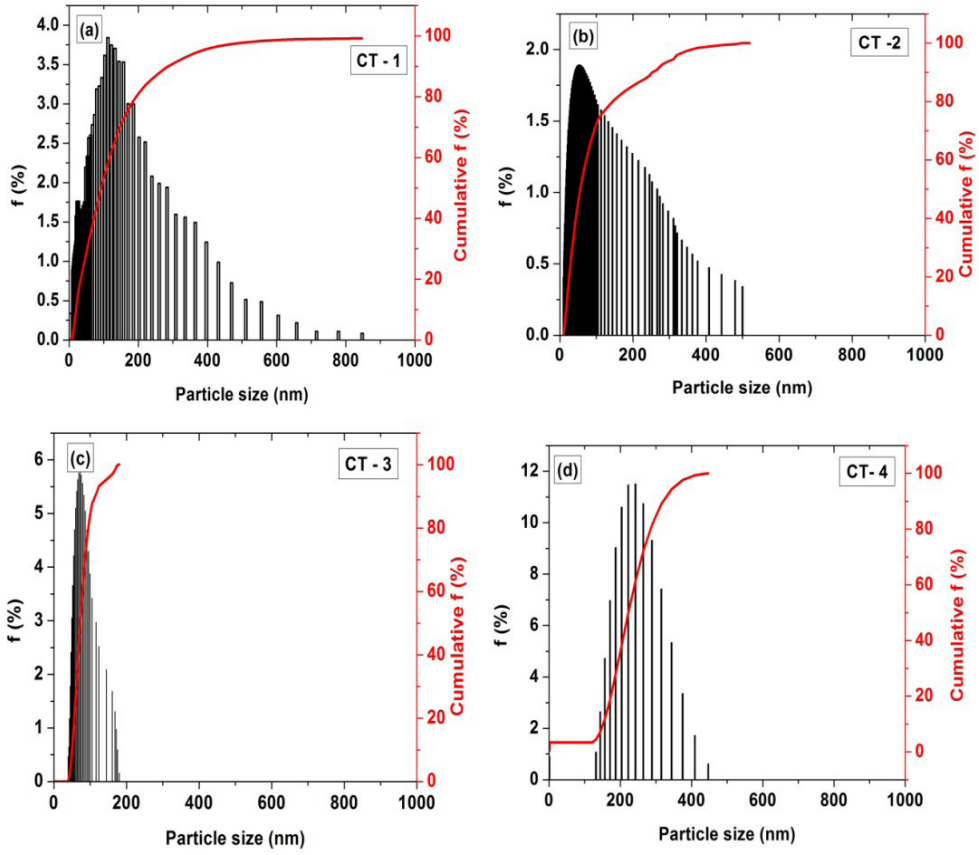

Figure 7.3: Particle size histograms of a) CT-1 b) CT-2, C) CT -3 and d) CT -4

Particle size Histograms which gives the particle size frequency percentage and cumulative frequency percentage as shown in Fig 7.3. Mean particle size calculated by the particle size analyzer for CT-1, CT-2, CT-3 and CT-4 and the respective values are 123, 120, 85 and 216 nm. Here particle size decreases with the concentration of CTAB up to CT-3 and then the particle size increases. This may due to the excess of surfactant the same is supported by the XRD and FTIR results. Histogram of CT-3 depicts that the sample have relatively uniform distribution whereas CT-1 has the distribution from 1 to 800 nm. These results suggest that the particle size distribution affected by the concentration of surfactant for the current experimental conditions.

7.3.4. SEM Analysis

Morphological studies of copper oxide materials using Scanning Electron microscope (SEM) images are shown in Fig. 7.4. CT-1, CT-2, CT -3 and CT-4 have flake, leaves, flower and sheets like morphologies. Concentration variation of CTAB can modify morphology in high alkaline condition which is supported by this study. Many authors used CTAB in the hydrothermal method. But the current study proves that CTAB can be used as the surfactant for wet chemical method too.

7.3.5. UV- Visible DRS spectrum analysis

UV-DRS absorption spectrum of synthesized materials was shown in Fig. 7.5 (a). It clearly shows that the samples having strong absorbance in the visible region. The absorption peaks are 655, 603, 594 and 478 nm for CT-1, CT-2, CT-3 and CT-4 respectively. The absorption is red shifted with the increment of CTAB. Since the absorption occurs in the visible region, synthesized nanomaterials can be used as the sunlight photocatalysts. The band gap of the materials was calculated using the plot of $(\alpha h\nu)^2$ Vs $h\nu$. Where, α is calculated using Kubelka- Munk theory [Wei Changa et al., 2015].

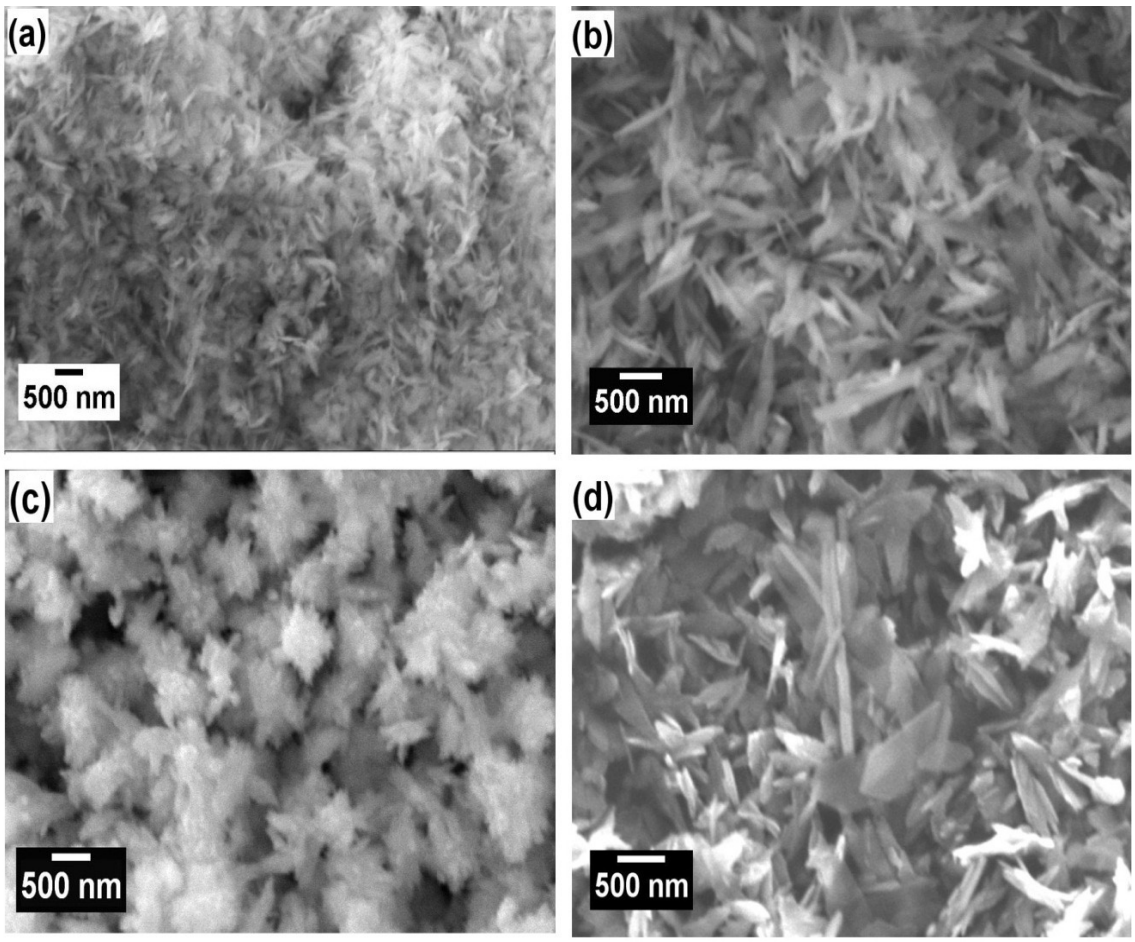

Figure 7.4 : SEM pictures of a) CT-1 b) CT-2, C) CT -3 and d) CT -4

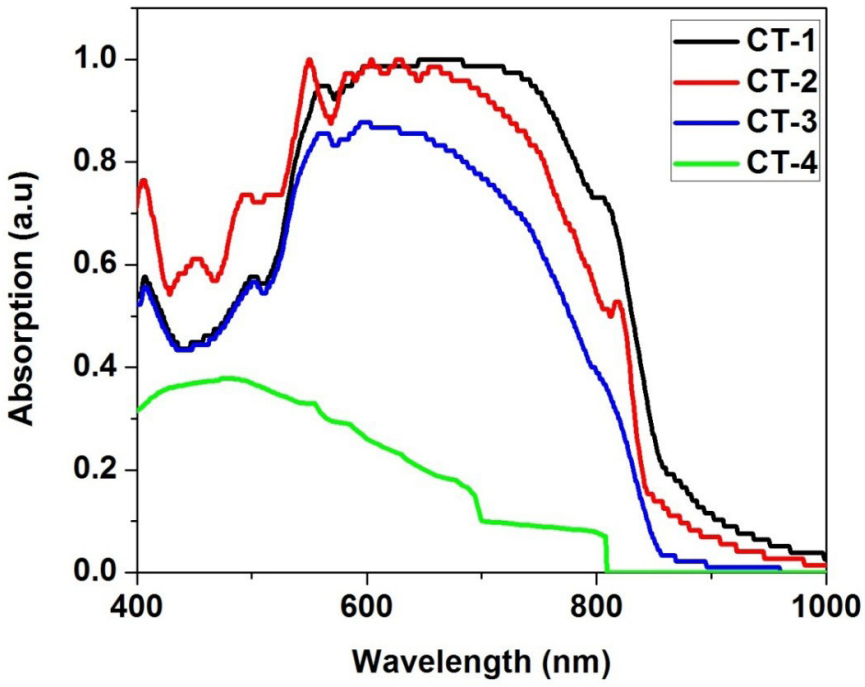

Figure 7.5 (a): UV-Vis Diffusion reflectance absorption spectra of copper oxide nanostructures synthesized using CTAB surfactant

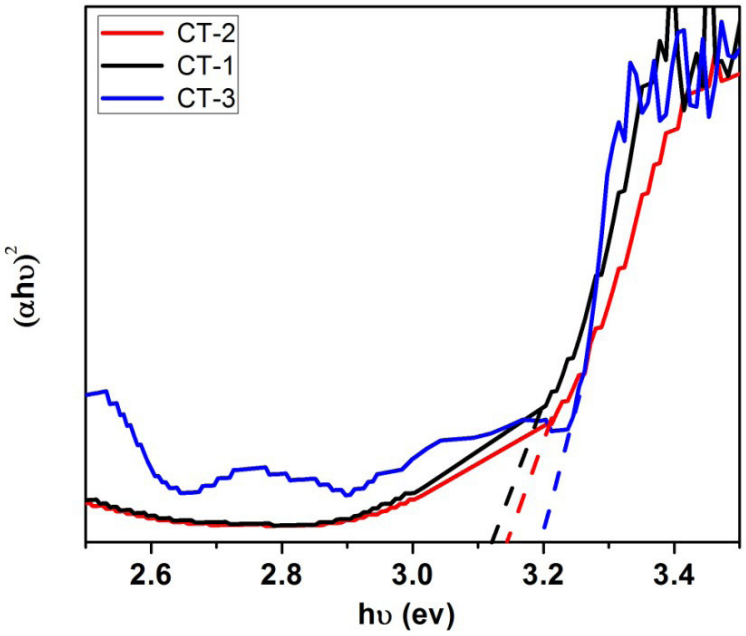

Figure 7.5 (b) Plot of $(\alpha h\nu)^2$ Vs hν for copper oxide nanostructures CT-1, CT-2, CT-3 and CT-4

Fig 7.5(b) shows the Tauc's plot of the synthesized materials. Calculated band gap values are 3.12, 3.16 and 3.2 eV for the synthesized nanomaterials. The obtained results are obviously blue-shifted with respect to the bulk CuO (E_g=1.2 eV). If the sizes of semiconductor materials are reduced to nanoscale range, their valence band and conduction band are altered due to the quantum confinement effect [Xinyuan Zhao et al., 2004].

7.3.6. Electrical properties

7.3.6.1. Impedance analysis

Fig.7.6 shows the Nyquist plot for the materials a) CT-1, b) CT-2, C) CT-3 and d) CT-4. It is observed that Nyquist plot exhibits the single semicircular nature which denotes the bulk properties of the materials are dominated than the grain boundaries. CT-1 has comparatively perfect semicircle, but CT-2 and CT-3 has arc shaped semicircles. The skewed arc shaped curve is the characteristic of non- uniform distribution in relaxation mechanism. Where the distributions on the higher frequency side of the principal relaxation time decreases more rapidly than those on the low frequency side. As the temperature increases radius of the semicircle decreases for all the samples which confirms the NTCR behavior of the samples.

Fig.7.7 shows how the imaginary impedance of CT-1 and CT-3 varied with the frequency and temperature. As the frequency increases Z'' produces the peak. As the temperature increases, the peak height decreases and the peak shifted to the higher frequency side. Relaxation time was calculated from the peak, using the relation $\omega_{max}\,\tau=1$ and given in the Table 7.3.

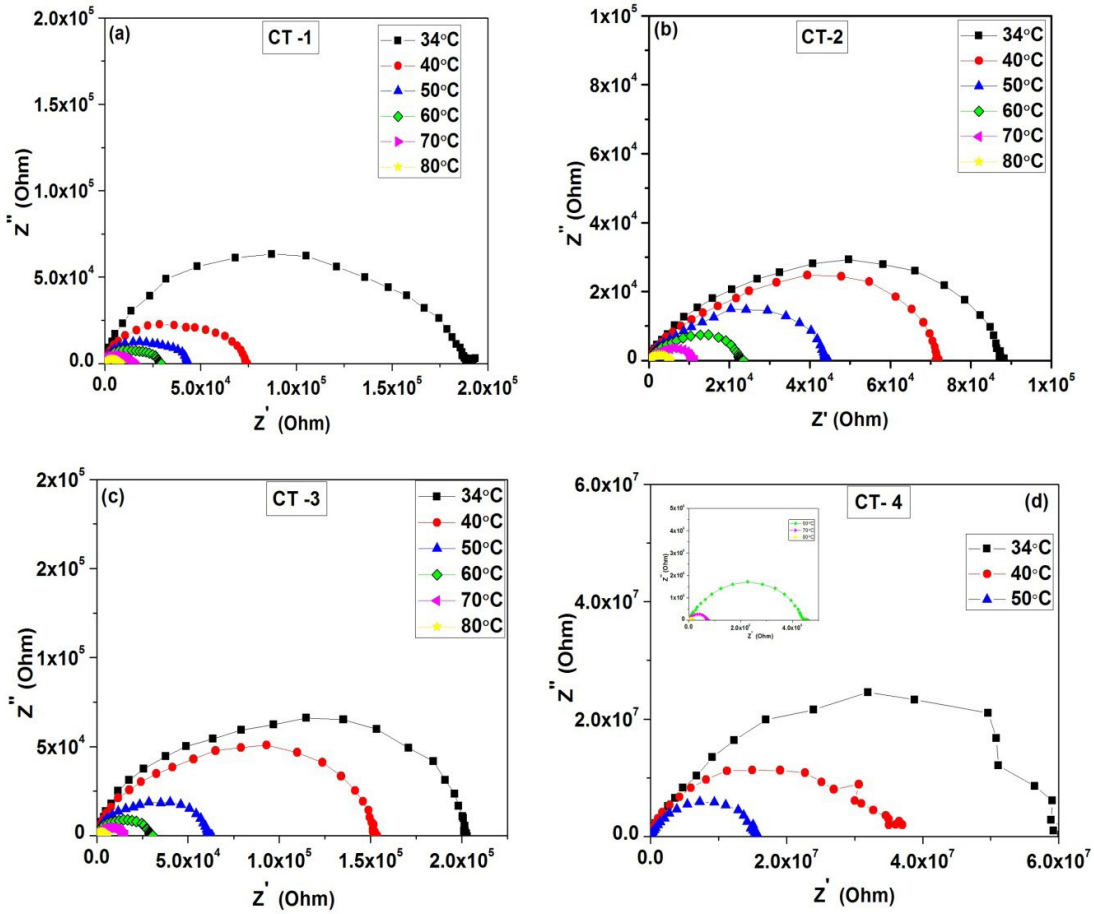

Figure 7.6: Nyquist Plot of the CuO nanostructures

(a) CT-1, (b) CT-2, (c) CT-3 and (d) CT-4

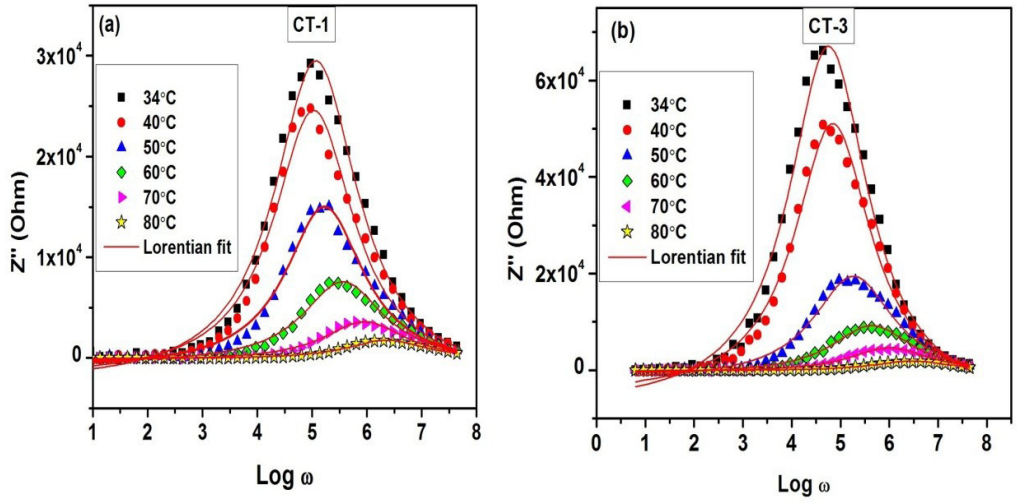

Figure 7.7: Variation of Z'' with frequency and temperature for

(a) CT-1 and (b) CT-3

Table 7.3: Relaxation time for CT-1 and CT-3 at various temperatures.

Temperature (° C)	Relaxation time (μS)	
	CT-1	CT-3
34	8.48	17.6
40	9.39	14.4
50	5.96	5.42
60	2.78	2.28
70	1.11	1.01
80	0.44	0.39

7.3.6.2 AC & DC conductivity studies

` Fig. 7.8 (a) and (d) shows the AC conductivity of the synthesized CuO materials in the frequency range 1Hz to 7 MHz. Conductivity variation with the frequency follows the similar pattern for all the samples. The graph shows the low frequency plateau region followed by the high frequency dispersion region with the change in slope. At low frequency region, conductivity is frequency independent; this is because of the hopping of charge carriers in this region are at random direction [Mariappan et al., 2005]. Dispersion region of the conductance plot strongly depends on the frequency. As the temperature increases, conductivity of the synthesized samples is increased by 2 to 3 orders in magnitude. At high frequencies the conductivity of the materials are coincidence with each other and attain the temperature independent nature. This is attributed to the presence of conduction phenomena which is due to the short range mobility of charge carriers [Behr et al., 2008]. As the temperature increases plateau region increases and the slope decreases.

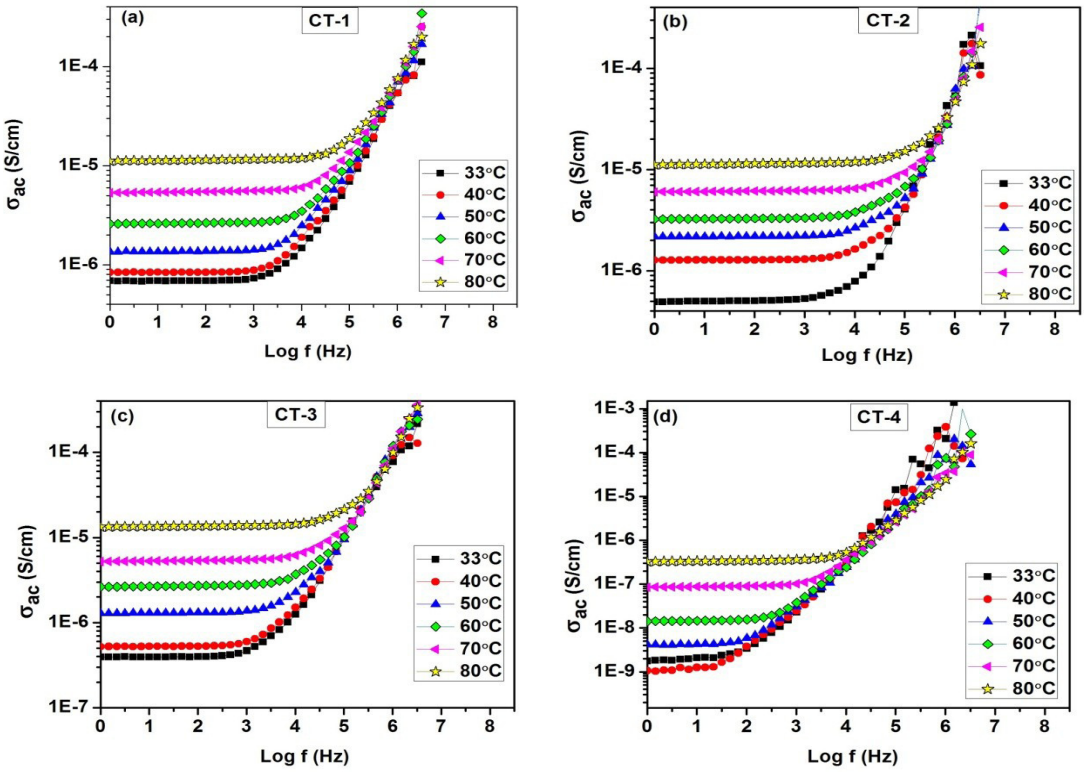

Figure 7.8: Variation of AC conductivity with Temperature and frequency for a) CT-1 b) CT-2, C) CT-3 and d) CT-4

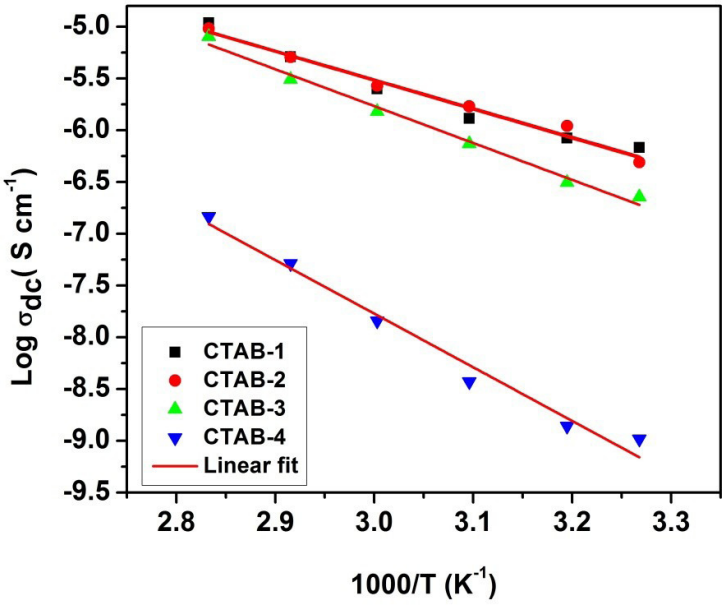

Figure 7.9: Arrhenius plot of the DC conductivity of CuO nanostructures CT-1, CT-2, CT-3 and CT-4

Fig 7.8 shows that, the conductivity decreases with an increment of concentration of surfactant which creates the reduction in particle size. This may due to the increase in the grain boundary volume and the proportionate increase in disorder introduced in the sample due to the surfactant. If the particle size is smaller than the electron mean free path, grain boundary scattering dominates and thus the electrical resistance expected to increase [Ponpandian et al., 2002]. The samples CT-1, CT-2 and CT-3 are relatively have the same range of conductivity. In CT-4, conductivity decreased by two orders of magnitude because of the excess surfactant. For CT-1, CT-2 and CT-3, the dc conductivity region is upto 1000 Hz but for CT-4 it is upto 100 Hz only. σ_{ac} is due to short range intra well hoping of carriers within one defect potential. σ_{dc} is due to long range hopping of charge carriers from one defect potential well to the adjacent defect potential well [Sayer et al., 1978]. In the case of CT-4 intra well hopping is dominated which may due to the small particle size. The dc conductivity values detected from conductance plot was given in Table 7.4.

Table 7.4: Conductivity of the copper oxide nanostructures at various temperatures

Temperature °C	Conductivity (S/cm)			
	CT-1	**CT-2**	**CT-3**	**CT-4**
34	6.8 E-7	4.9 E-7	2.26 E-7	1.04 E-9
40	8.4 E-7	1.1 E-6	3.12 E-7	1.42 E-9
50	1.3 E-6	1.7 E-6	7.4 E-7	3.72 E-9
60	2.5 E-6	2.69 E-6	1.52 E-6	1.44 E-8
70	5.1 E-6	5.09 E-6	3.1 E-6	5.14 E-8
80	1.09 E-5	9.6 E-6	8.02 E-6	1.47 E-7

Arrhenius plots of dc conductivity for CT-1, CT-2, CT-3 and CT-4 was displayed in Fig.7.9. Dc conductivity increases with the temperature reveals that the electrical conduction in this process is thermally activated. Dc conductivity linearly changes with the inverse temperature and obeys the Arrhenius equation $\sigma_{dc} = \sigma_0 \exp\left(\frac{-E_a}{K_B T}\right)$ where σ_{dc}denotes dc conductivity of the samples, K_B is Boltzmann constant, T is absolute temperature. E_a is activation energy. Activation energy is 0.551, 0.553, 0.707 and 1 eV for CT -1, CT -2, CT -3 and CT-4 respectively.

7.3.6.3 Dielectric studies

Dielectric response of the materials CT-1 and CT-3 was shown in Fig 7.10. Fig 7.10(a) shows the variation of dielectric constant with the various temperatures and frequencies for CT-1. Here three regions can be noticed such that (i) oscillating region (from 1 to 10^2 Hz) (ii) frequency independent region (10^2 to 10^4Hz) and (iii) linear decreasing region (10^4 to 10^7 Hz). Dielectric constant value lies in the range of 10^3 to 10^4 for the measured temperatures. Dielectric loss (ε'') of CT-1, linearly decreases from 1 Hz to 7 MHz as shown in Fig. 7.10(b). At low frequencies ε'' is in the range 10^6 to 10^7 with different temperatures for CT-1.

For CT-3, variation of $\varepsilon'$with the frequency can also be divided in to three regions which are shown in Fig. 7.10(c). The value of ε' is linearly decreases in the frequency range 1 Hz to 10^6 Hz but the oscillating values observed between 1 Hz to 500 Hz. In the region 10^6 to 10^7 frequency independent dielectric response is noticed. ε' is varied from 10^2 to 10^4 in the temperature range 34 to 80° C for CT-3. From Fig.7.10 (d) it is noticed that ε'' of CT-3 was linearly decreases with the frequency and its value is in the order 10^6 to 10^7at low frequency region.

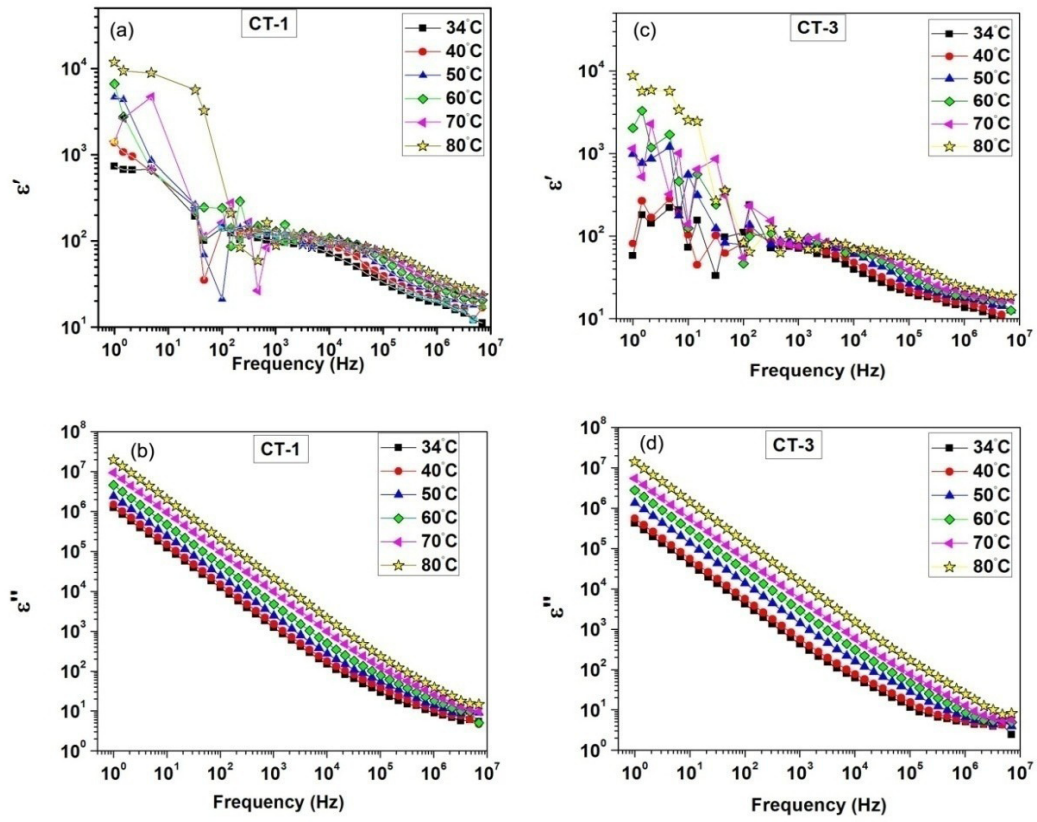

Figure 7.10: Dielectric response of the material CT-1 and CT-3

7.4. Conclusions

CuO nanostrucutres were synthesized by wet chemical method with four various concentration of CTAB and they named as CT-1, CT-2, CT-3 and CT-4. Nano crystalline nature of the materials was confirmed by XRD analysis. Presence of metal oxygen vibration bands were supported by the peaks of FTIR pattern. Particle size variation and distributions were analyzed using particle size histograms. Concentration variation of surfactant, changes the morphology of the synthesized materials is confirmed by the SEM images. Synthesized copper oxide materials absorb the light in the visible region and the band gap values are calculated using Kubelka-Munk theory. No enhancement of electrical conductivity properties is absorbed with the variation of concentration of CTAB in the synthesized samples. Relaxation time and Dielectric response of the CT-1 and CT-3 materials were discussed.

CHAPTER - VIII

SYNTHESIS AND CHARACTERIZATION OF COPPER OXIDE NANOSTRUCTURES USING IGEPAL –CA 210 SURFACTANT

In this chapter Igepal CA 210 (Octyl phenol ethoxylate) which has the following structure was used as the surfactant to synthesize copper oxide nanomaterial. Thanh Son et al., reported the synthesis of Fe_3O_4 nano particles using the Igepal Co 520 surfactant [Thanh Son et al., 2010]. Synthesis of copper oxide using Igepal as surfactant is not reported earlier, to the best of our knowledge.

8.1. Properties of Igepal CA-210

Average M_n	: ~294
Linear Formula	: $(C_2H_4O)_n \cdot C_{14}H_{22}O$ n~1.5
Description	: non-ionic
Density	: 1.009 g/mL at 25 °C
Solubility	: non soluble in water, readily soluble in ethanol
Molecular structure	:

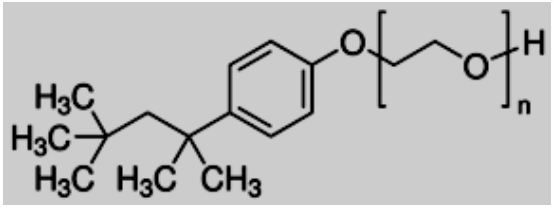

8.2. Synthesis of CuO using Igepal 210 surfactant

CuO nanomaterial was synthesized using Solid state reaction method [Wang et al., 2001]. Copper nitrate trihydrate [Cu $(NO_3)_2 \cdot 3H_2O$] (Himedia 99.5% purity), sodium hydroxide pellets [NaOH] (Nice chemicals), Igepal CA 210 $(C_2H_4\ O)_n$. $C_{14}H_{22}O$ (Sigma Aldrich) are the analytical grade chemicals used in this experiment without any further

purification. 4.83g (0.1M) of cupric nitrate and 1.6 g (0.2 M) sodium hydroxide pellets were grounded using the agate and mortar for 30 minutes. The resulted blue color pasty copper hydroxide was well washed with de-ionized water and ethanol several times. Then the material was kept in the furnace at 300° C for 5 hrs. This yields the black color CuO material. To synthesize CuO with surfactant, copper nitrate was grounded well with Igepal for 20 minutes and then the same procedure was followed. Here copper hydroxide was washed with de-ionized water after removing Igepal by washing with ethanol since the Igepal is immiscible with water. Three samples were synthesized such that NS-S without Igepal, IG -1 using 2.5 ml (0.05M) of Igepal, and IG-2 was using 5ml (0.1M) of Igepal.

8.3. Characterization studies of CuO synthesized using Igepal 210 surfactant

8.3.1. XRD Analysis

Fig.8.1 shows the XRD pattern of the synthesized materials. Broad peaks confirm the nanocrystalline nature of the material. There is no impurity peaks observed in the pattern which confirms the phase of the material. All the diffraction peaks are indexed in the monoclinic system which is well agreed with the JCPDS card no. 80-1916. The crystallite size calculated using Debye – Scherrer's formula. The cell parameters calculated using UNIT CELL software and the crystallite size was depicted in Table 8.1. The crystallite size of IG-2 is smaller than NS-S which confirms that the surfactant Igepal reduces the crystallite size. Table 8.1 also illustrates that all the synthesized materials are in the same monoclinic structure. β value of unit cells and cell volume of IG -1 and IG-2 are almost same, but skewed than the value of NS-S. These results confirm that surfactant affect the unit cell parameters and shape.

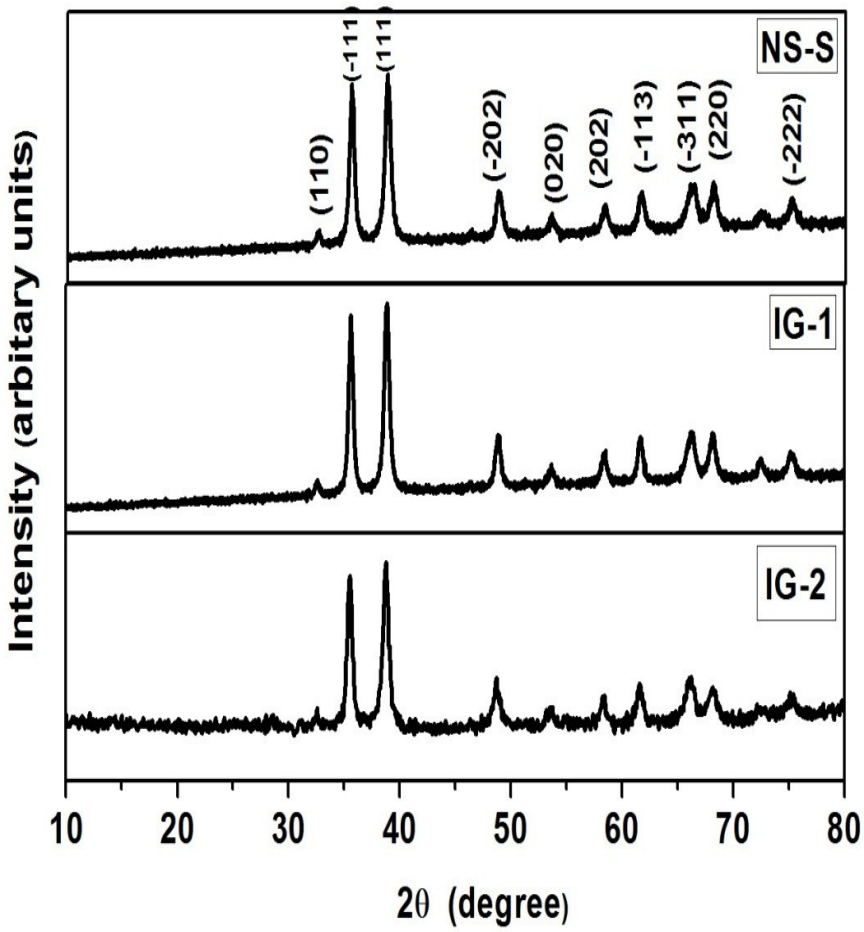

Figure 8.1: XRD Pattern of CuO nanostructures NS-S, IG-1, and IG-2

Table 8.1: Cystallographic data of CuO nanomaterials calculate using the unit cell software

Samples	A	b	c	β (deg)	cell volume (Å) ^{3}	Crystallite size (nm)
	Å					
NS-S	4.69	3.42	5.12	99.50	80.99	44
IG -1	4.81	3.20	4.43	92.79	68.24	37
IG - 2	4.79	3.21	4.42	92.67	68.13	25

8.3.2. FTIR Analysis

FTIR spectrum of synthesized nano CuO materials is shown in Fig. 8.2. The peaks at 442, 537 and 595 cm^{-1} represent the metal - oxygen stretching vibration which confirms the formation of copper oxide. OH bending vibration at 1628 cm^{-1} indicates the presence of the physically adsorbed water on the surface of the material. No peaks in the region 600 to 650 cm^{-1} confirms the absence of another phase of Cu_2O [Anita Sagadevan Ethiraj et al., 2012].

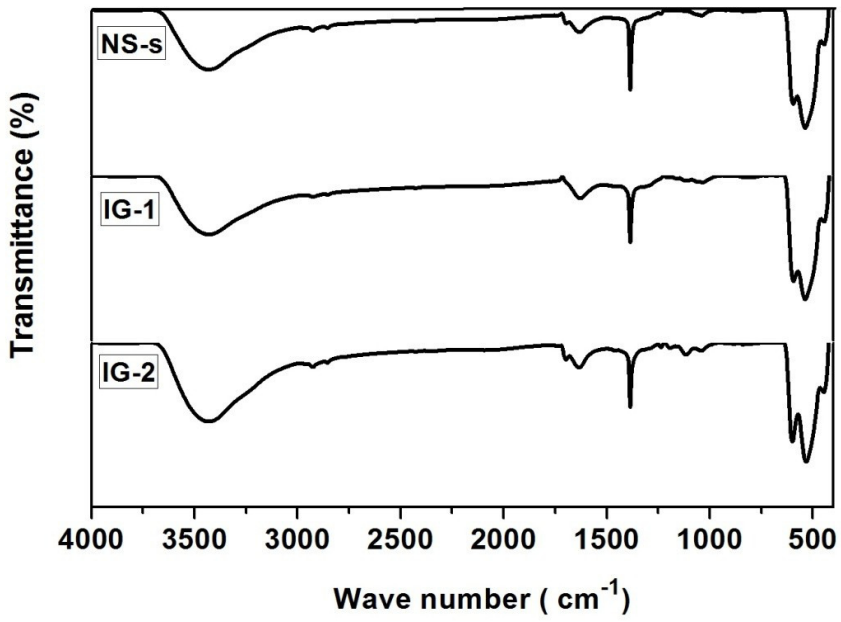

Figure 8.2: FTIR spectrum of CuO nanostructures NS-S, IG-1, and IG-2

8.3.3. SEM Analysis

Fig. 8.3(a), (b) and (c) shows the SEM images of the Copper oxide nanomaterials. Fig. 8.3 (a) clearly reveals that NS-S has the morphology of the particle with smooth surface. Sponge like morphology of the materials IG-1 and IG-2 are displayed in Fig 8.3 (b) and (c). From the different morphologies of the synthesized materials it can be concluded that Igepal can also acts as the template and changes the morphology of the material for the current experimental conditions.

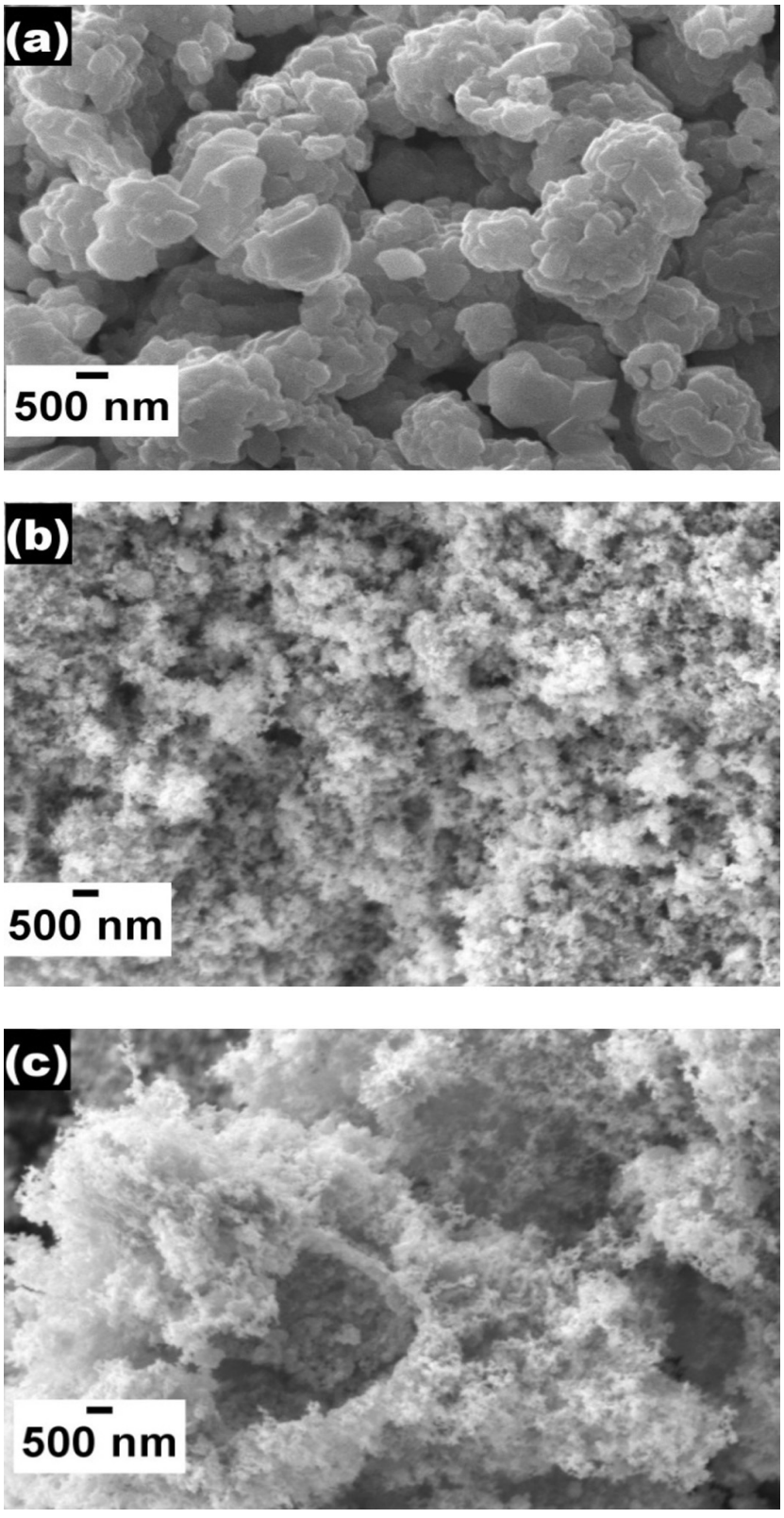

Figure 8.3: SEM images of (a) NS-S, (b) IG-1, and (c) IG-2

8.3.4 UV- Vis DRS spectrum analysis

UV diffusion reflection spectrum and Tauc's plot of NS-S, IG-1 and IG-2 was given in Fig. 8.4(a) and (b) respectively. Fig 8.4(a) clearly shows that sample NS-S have a small absorbance peak in the region of wavelength from 358 to 492 nm. IG-1 shows the broad absorption band from 300 to 850 nm with the peak value 507 nm. And IG-2 has the absorbance band in the range 340 to 840 nm with the peak value 680 nm. Increment of concentration of Igepal- 210, increases the absorption region. Since the absorption occurs at the visible region, NS-S, IG-1, IG-2 can be used as sunlight photocatalysts.

The band gap of the materials calculated using Kubelka- Munk equation and the plot $(\alpha h\upsilon)^2$ versus $(h\upsilon)$. The bandgap of the synthesized materials NS-S, IG-1, and IG-2 calculated is 4.91, 4.59, and 4.27 eV. These values are comparable with reported values [Zayyoun et al., 2016]. Even though the particle size decreases, band gap decreases with the increment of Igepal surfactant. This may due to the changes in electronic structure of the materials with the change of morphology which is caused by increment of surfactant. Band gap of the synthesized materials is higher than that of band gap of the bulk CuO (1.8 eV). This blue shifting is due to the quantum confinement effect [Asha et al., 2014].

8.3.5. Electrical properties

8.3.5.1. Impedance Analysis

Fig 8.5 shows the Nyquist plot of the (a) NS-S, (b) IG-1 and (c) IG-2 nanostructures. For NS-S, IG-1 and IG-2 lightly depressed, strongly depressed and perfect semicircle was obtained respectively. The depression of the semicircles is another evidence of polarization phenomena with the distribution of relaxation times.

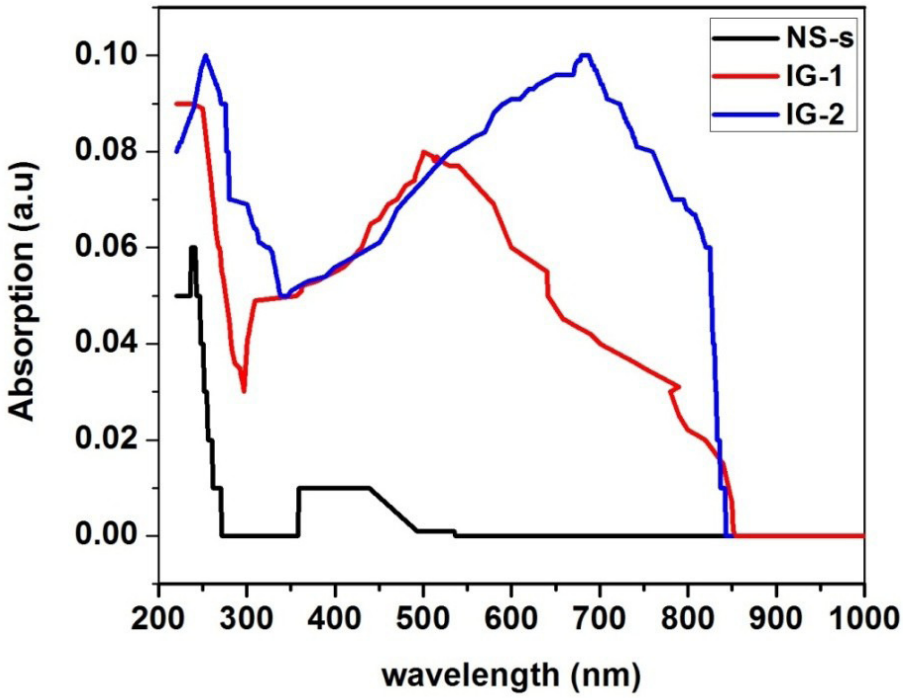

Figure.8.4 (a) UV- Visible diffusion reflectance spectrum of the samples NS-S, IG-1 and IG-2

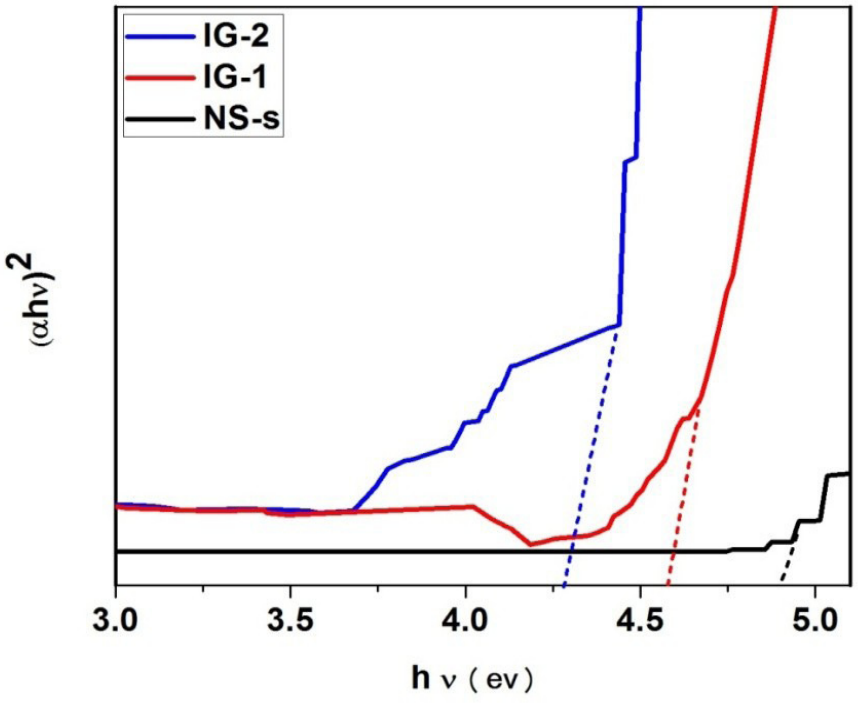

Figure 8.4 (b): Plot of $(\alpha h\nu)^2$ Vs hν of the samples NS-S, IG-1 and IG-2

The most accepted approach to interpret the semicircle depression phenomena is to consider them as being due to statistical distribution of relaxation times [Sen et al ., 2006, Nobre et al., 2001, Cole & Cole 1941]. In general whether a full, partial or no semicircle is observed depends on the strength of the relaxation and the experimentally available frequencies. It is seen that the effect of bulk (single semicircle) is prominent for NS-S at all measured temperatures [Shrabanee Sen et al., 2008]. For IG-1 and IG-2 Nyquist plot have a semicircle and small arc at room temperature, which validate the presence of both the grain and grain boundary effects. It can be concluded that Igepal surfactant creates changes in the electrical properties in consequence of constructing the structural changes. As the temperature increases, radius of the semicircle shrinks for NS-S, IG-1 and IG-2, which signifies the NTCR behavior of the samples.

Loss spectrum for NS-S and IG-2 with frequency at different temperature was shown in Fig. 8.6. Variation of Z'' materialize a peak with a characteristic frequency ($\omega_{max} = 2\pi f_{max}$), which is dependent on temperature and this can be related to the type and strength of the electrical relaxation phenomena in the materials. The asymmetric peak which shifts to higher frequency with the increase in temperature ensures the temperature dependent relaxation process in the sample with a spread of relaxation time. The relaxation time τ was calculated and given in Table 8.2.

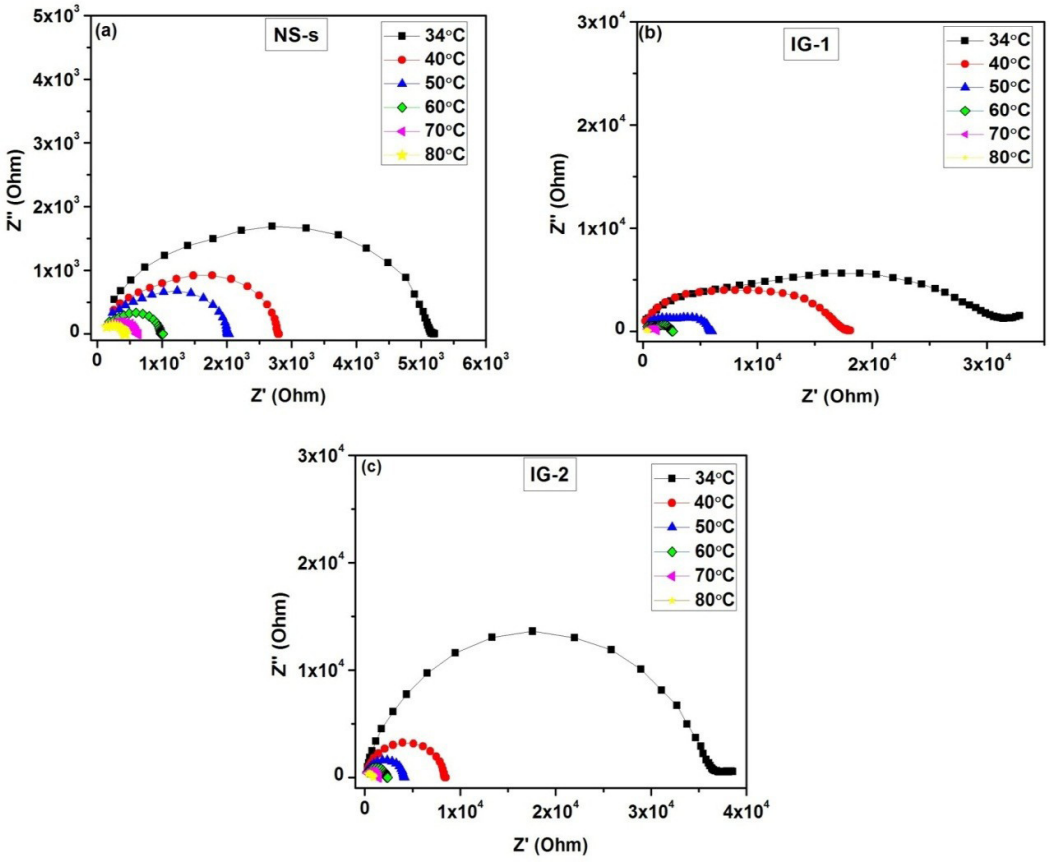

Figure 8.5: Nyquist Plot of CuO nanostructures (a) NS-S, (b) IG-1 and (b) IG-2

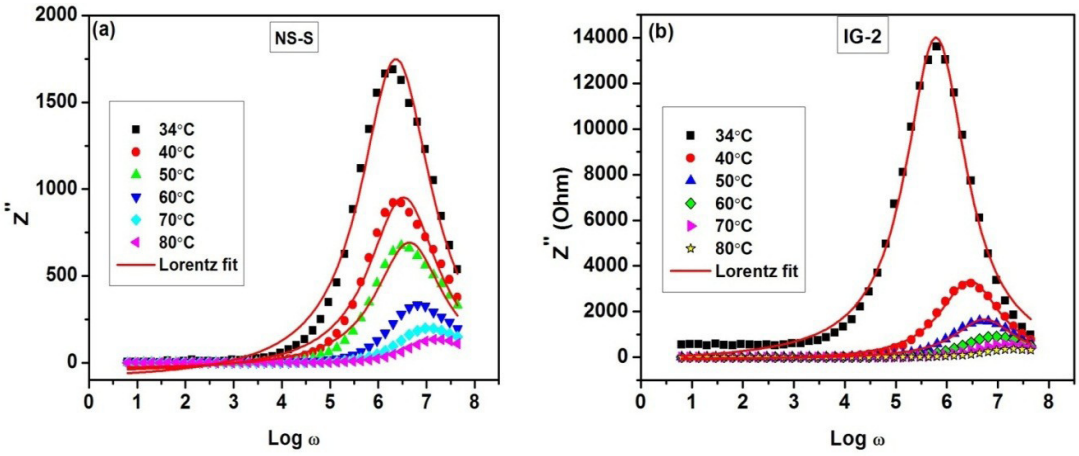

Figure 8.6: Variation of Z'' with frequency and temperature for

(a) NS-S and (b) IG-2

Table 8.2: Relaxation time for NS-S and IG-2 samples at different temperatures

Temperature (° C)	Relaxation time (μS)	
	NS-S	IG-2
34	4.31	1.63
40	3.00	0.35
50	2.28	0.185
60	1.56	0.106
70	1.06	0.072
80	0.491	0.049

8.3.5.2 AC and DC conductivity

Fig 8.7 shows the ac conductivity variation with different frequencies and at various temperatures for (a) NS-S, (b) IG-1 and (c) IG-2. It is observed that the conductivity spectrum indicates the two different regions within the measured frequency range; they are a plateau at low frequency and conductivity dispersion at high frequency. But for NS-S samples, the plateau region extends upto 1 MHz where as for IG -1 sample dc conductivity region extends upto 100 KHZ. This indicates for IG-1 sample intra-well hopping is dominated. DC conductivity of the samples at different temperatures were found from plateau region of fig and illustrated in Table 8.3. Using the dc conductivity and the temperature, Arrhenius plot was drawn which is shown Fig.8.8. From the Arrhenius plot activation energy of the carriers was calculated they are 0.48, 0.81 and 0.39 eV for NS-S, IG-1 and IG-2 samples.

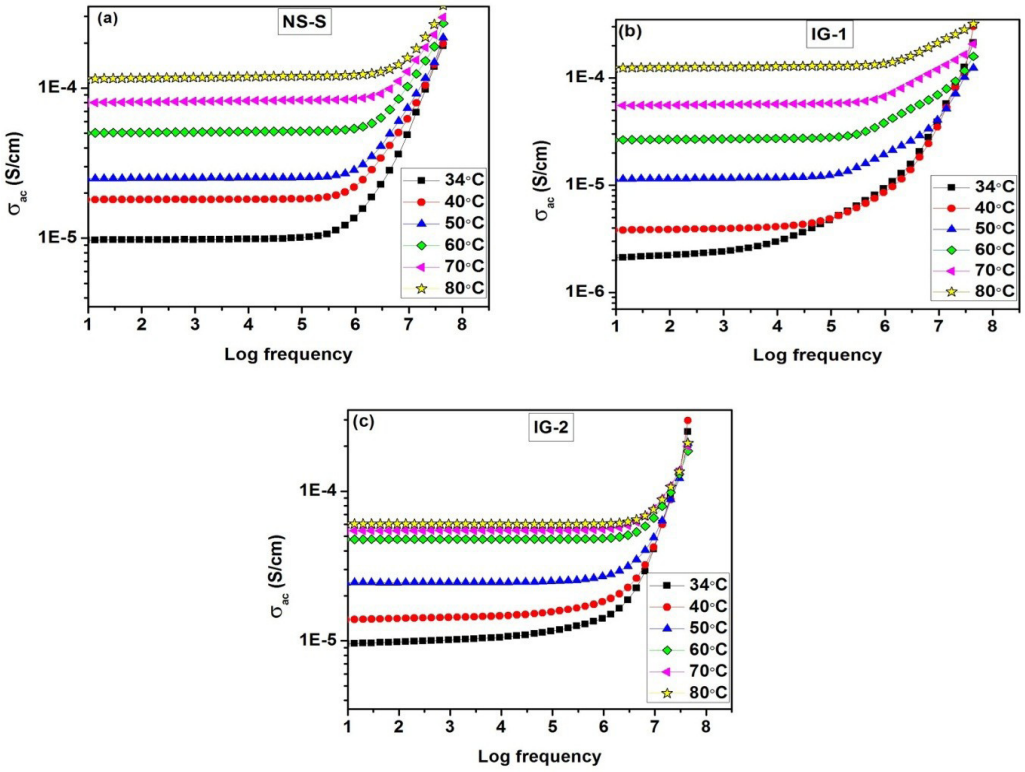

Figure 8.7: Variation of AC conductivity with frequency and temperature for samples (a) NS-S (b) IG-1 and (c) IG-2.

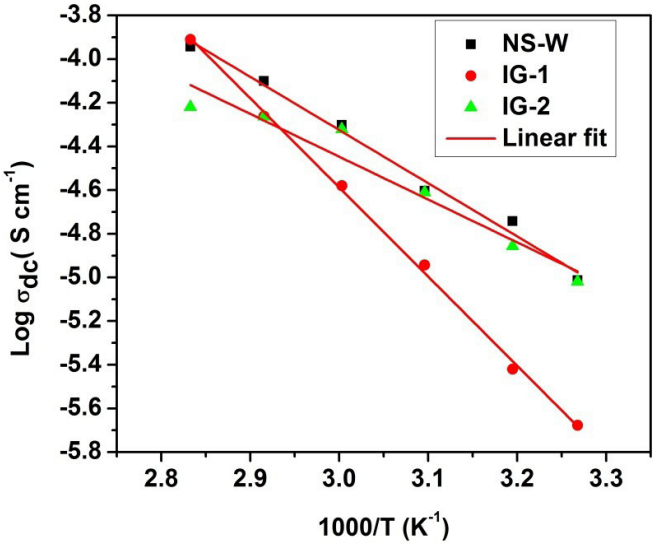

Figure 8.8: Arrhenius Plot of the DC conductivity for the samples NS-S, IG-1 and IG-2.

Table 8.3: DC conductivity values for the samples (a) NS-S (b) IG-1 and (c) IG-2.

Temperature (°C)	Conductivity (S/cm)		
	NS-S	IG-1	IG-2
34	9.71 E-06	2.10 E-06	9.57 E-06
40	1.81 E-05	3.80 E-06	1.39 E-05
50	2.49 E-05	1.14 E-05	2.45 E-05
60	4.99 E-05	2.63 E-05	4.77 E-05
70	7.94 E-05	5.48 E-05	5.46 E-05
80	1.14 E-04	1.23 E-04	6.04 E-05

8.3.5.3. Dielectric properties

Fig 8.9 (a) and (c) shows the variation of dielectric constant with various frequencies and different temperatures. Dielectric loss of the materials NS-S and IG-2 was shown in Fig 8.9 (b) and (d). The dielectric response of the material NS-S from 1 HZ to 1 KHZ is not in a uniform manner. At all the temperatures there is low frequency dispersion with oscillating values. Above 1 KHz to 7 MHz uniform decreasing of dielectric constant is noticed. Maximum of Dielectric constant value at low frequency and higher temperature is in the order of 10^4. For IG-2 some different dielectric behavior is noticed in Fig. 8.9 (b). Here ε' value decreases with the temperature up to 60° C and then slowly started to increase. Low frequency dispersion region of IG-2 sample is continued upto 10^5 Hz and then reached the constant value. Maximum value of dielectric constant of IG-2 is in the order of 10^5. Dielectric loss value of both the samples linearly decreases with the frequency and increases with the temperature

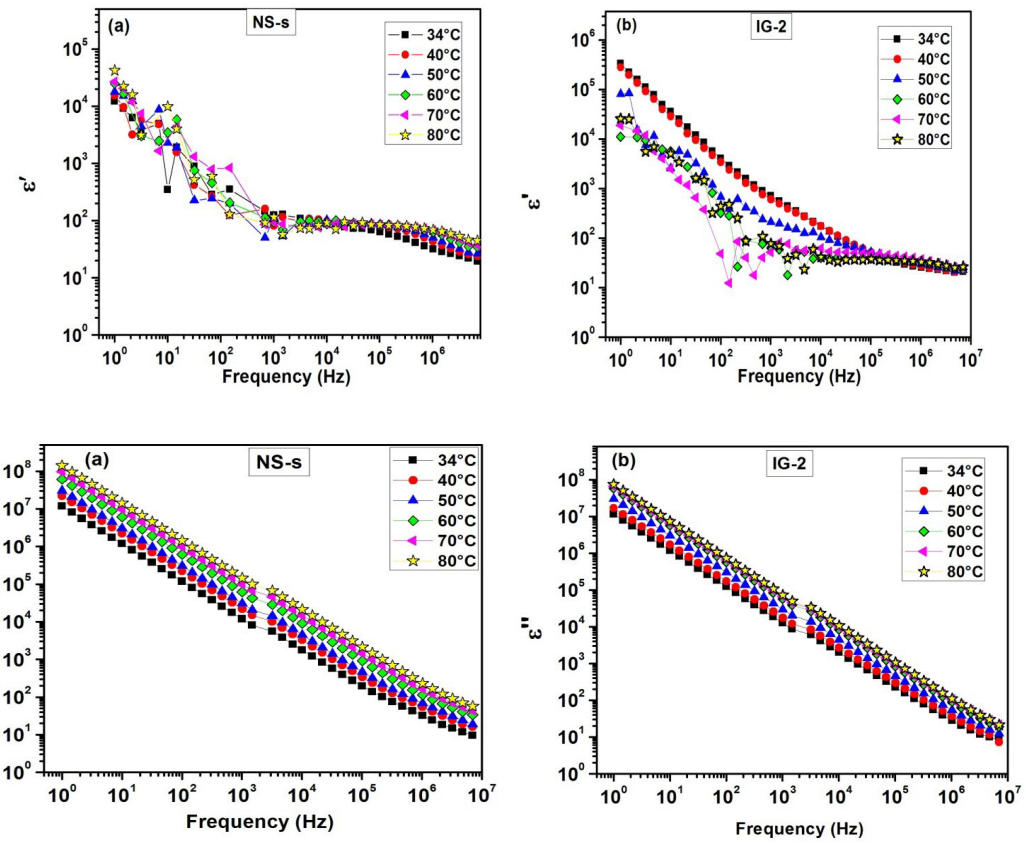

Figure 8.9 Dielectric response of the materials (a & c) NS-S and (b & d) IG-2

For NS-S ε'' has the high value at low frequencies it is in the order of 10^8, in the case of IG-2 it is 10^7. At higher frequencies, Linear dielectric response of IG-2 may reduce the dissipation energy and so the dielectric loss.

8.4. Conclusions

Copper oxide nanomaterials NS-S, IG-1 and IG-2 were synthesized by solid state reaction method using Igepal as the surfactant. Crystallite size was calculated from the XRD pattern, decreased for the material synthesized with Igepal ensures its surfactant effect. UV- Vis DRS spectrum reveals that the band gap of the materials was affected by the surfactant. Igepal surfactant changes the morphology of the material to nanosponge from nanoparticle. Conductivity properties and the Dielectric properties were decreased by adding the surfactant.

CHAPTER – IX
APPLICATIONS

9.1. Photo catalytic properties of CuO Nanostructures

9.1.1. Photocatalyst

A catalyst changes the rate of chemical reactions, while it is not consumed by the reaction itself. A photocatalyst is the substance that generates catalyst activity using energy from light. There are two linked parts of the photocatalysis mechanism (photo and catalysis). The first part (the photo part) concerns the phenomenon linked to the light material interaction which includes photos absorption, charge carrier creation, dynamics and also surface trapping. The second part (catalysis part) concerns the phenomenon linked to the surface radical formation and surface reactivity that is the interaction between H_2O, O_2, organic pollutant and the oxide surface. For the photo part the most effective structural parameter on photocatalysis is the crystalline quality, which can be expressed in terms of the crystallite size. For the catalysis part, the specific surface area is the most effective structural parameter. Together with these parameters, atmospheric pollution, OH groups and particle size distribution also contribute to the photocatalytic process [Boujday et al., 2004].

CuO was reported as the good photo catalyst in many reports, [Meshram et al., 2012, Wang et al., 2012, Xia Hui-li et al., 2007, Hoffmann et al., 1995, Mohammad et al., 2015, Huaxia Shi et al., 2014]. But photo catalytic properties for the degradation of organic dyes directly related to the synthesis technique, particle shape and size. We have synthesized number of copper oxide nanostructures with various concentrations of surfactants. They have diverse morphology, different crystallite and particle size. We have performed the photocatalytic experiment in order to find the degradation ability of

the synthesized materials under natural solar light and Congo red dye is used as model pollutant.

9.1.2. Properties of Congo red dye material

- **Congo red** is an organic compound, the sodium salt of 3,3′-([1,1′-biphenyl]-4,4′-diyl)bis(4-aminonaphthalene-1-sulfonic acid.
- It is under the category of azo dyes.
- Congo red is water-soluble, yielding the red colloidal solution.
- The use of Congo red has long been abandoned, primarily because of its carcinogenic properties.
- Congo red can be used as a pH indicator
- Chemical formula : $C_{32}H_{22}N_6Na_2O_6S_2$
- Molar mass : 696.665
- Chemical structure

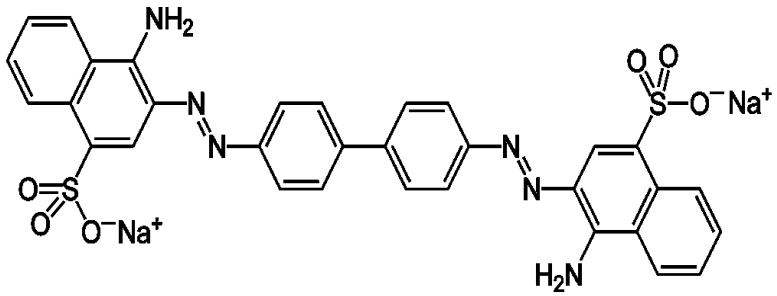

9.1.3. Photocatalytic Experiment

In order to demonstrate the photocatalytic activity of the synthesized CuO nanostructures the degradation of the Congo red under the sunlight irradiation was investigated. Congo red powder was dissolved in the deionized water and solution with 10 ppm concentration was prepared. In a glass beaker 100 ml of Congo red solution 10 mg of synthesized CuO powder was dispersed and it is kept under sunlight. After every

hour 2 ml solution from the beaker was collected separately and the absorption was read out using the UV visible spectrometer in the wavelength range of 200 to 800 nm. In order to get relatively uniform intense light energy the experimentation was carried out from 10.30 am to 2.30 pm. The luminosity of sun light at the time of the experiment was measured using the sun meter and it was found to be as 950 to 1100 Watt/m^2. Photocatalytic experiment was done at the same day and time for the synthesized nanostructures.

9.1.4. Mechanism of Photocatalytic degradation

In the photocatalytic process, the metal oxide is activated with light photons, and photo excited electrons are promoted from the valence band to the conduction band, forming an electron/hole pair (e^-/h^+). The photo-generated pair (e^-/h^+) is able to reduce and/or oxidize the compound adsorbed on the photocatalyst surface. The photocatalytic activity of the metal oxide comes from two sources: (i) generation of OH radicals by oxidation of OH anions (ii) generation of O_2 radicals by reduction of O_2. Both the radicals and anions can react with the pollutants to degrade or transform them to lesser the harmful byproducts.

9.1.5. Dye degradation mechanism of CuO

When photocatalyst (CuO) absorbs radiation from sunlight it will produce the pairs of electrons and holes. The electron of the valence band of copper oxide becomes excited when illuminated by light. The excess energy of this excited electron promoted the electron to the conduction band of CuO therefore creating the negative-electron (e^-) and positive-hole (h^+) pair. This stage is referred as the semiconductor's 'photo-excitation' state.

The positive-hole of CuO breaks the water molecule to form hydrogen gas and hydroxyl radical.

$$h^+ + H_2O \rightarrow OH^- + H^+ \quad \text{---------- (9.1)}$$

$$h^+ + OH^- \rightarrow OH^* \quad \text{---------- (9.2)}$$

The negative-electron reacts with oxygen molecule to form super oxide anion.

$$e^- + O_2 \rightarrow O_2^{*-} \quad \text{---------- (9.3)}$$

$$H_2O + O_2^{*-} \rightarrow OOH^* + OH^- \quad \text{---------- (9.4)}$$

$$Dye + OH^* \rightarrow Dye_{OX} \quad \text{---------- (9.5)}$$

$$Dye + O_2^{*-} \rightarrow Dye_{RE} \quad \text{---------- (9.6)}$$

These hydroxyl radicals are strong oxidation agent to breakdown any organic matter to carbon dioxide and water (Rauf et al., 2009, Behrouz Shaabani et al., 2014, Hoffman et al., 1995]

$$Dye + OH^* \rightarrow \text{Intermediate Products} \rightarrow CO_2 + H_2O \quad \text{---------- (9.7)}$$

So the photocatalyst can be defined as the material that is capable of absorbing light, producing electron–hole pairs that enable chemical transformations. After each cycle of such interactions, the reaction participants and regenerate its chemical composition. [Mohammad MansoobKhan 2015]. Fig. 9.1 shows the pictorial representation of degradation mechanism of the organic dye material.

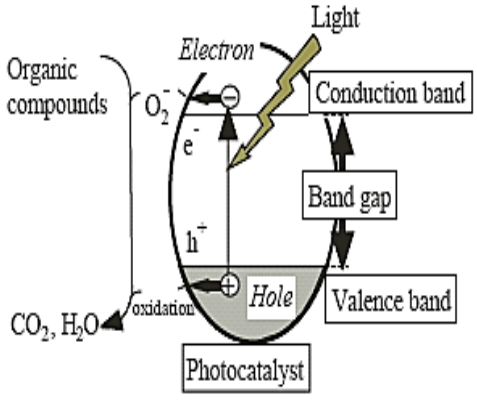

Figure 9.1: Pictorial representation of the degradation of dye in the presence of photocatalyst

9.1.6 Photocatalytic properties of the CuO nanostructures synthesized with PEG surfactant

Fig. 9.2 shows the time dependent UV absorption spectra of Congo red dye solution in the presence of CuO nanocatalyst synthesized using PEG surfactant (a) NS-w (b) PEG-1(c) PEG-2 (d) PEG-3. From Fig. 9.2 it was observed that Congo red has two absorption peaks at 340 nm and 498 nm. Degradation of dye material was shown by the decrement of absorption peak at every one hour interval till four hour. The degradation rate of Congo red in the presence of catalyst was calculated using the formula

$$\text{Degradation rate} = \left(\frac{A_0 - A_t}{A_o} \right) \times 100 \qquad \text{---------- (9.8)}$$

Where A_0 is initial absorption, A_t is absorption after t hours. Fig. 8.3 shows the degradation percentage of NS-W, PEG-1, PEG-2 and PEG-3. The total degradation of NS-W, PEG-1, PEG-2 and PEG-3 catalysts was 52, 47, 53 and 65 % respectively. PEG-3 sample has higher degradation ability and this may due to the smaller crystal size.

Fig 9.3 shows the degradation rate of PEG with different time intervals. Not much difference in degradation path was observed between the samples. After two hours, rapid degradation of dye was noticed and this is due to the higher intensity of sun light at that time (12.30 pm to 2.30 pm).

9.1.7. Photocatalytic properties of the CuO nanostructures synthesized with PVP surfactant

Fig.9.4 shows the UV absorption spectra of Congo red with copper oxide materials (a) PVP-1, (b) PVP-2, (c) PVP-3 and (d) PVP-4. Fig. 9.4 shows that Congo red has two absorption peaks around 490 nm (peak 1) and 340 nm (peak 2). Spectral intensity of peak 1 decreases with the increase in time, but peak 2 increases progressively.

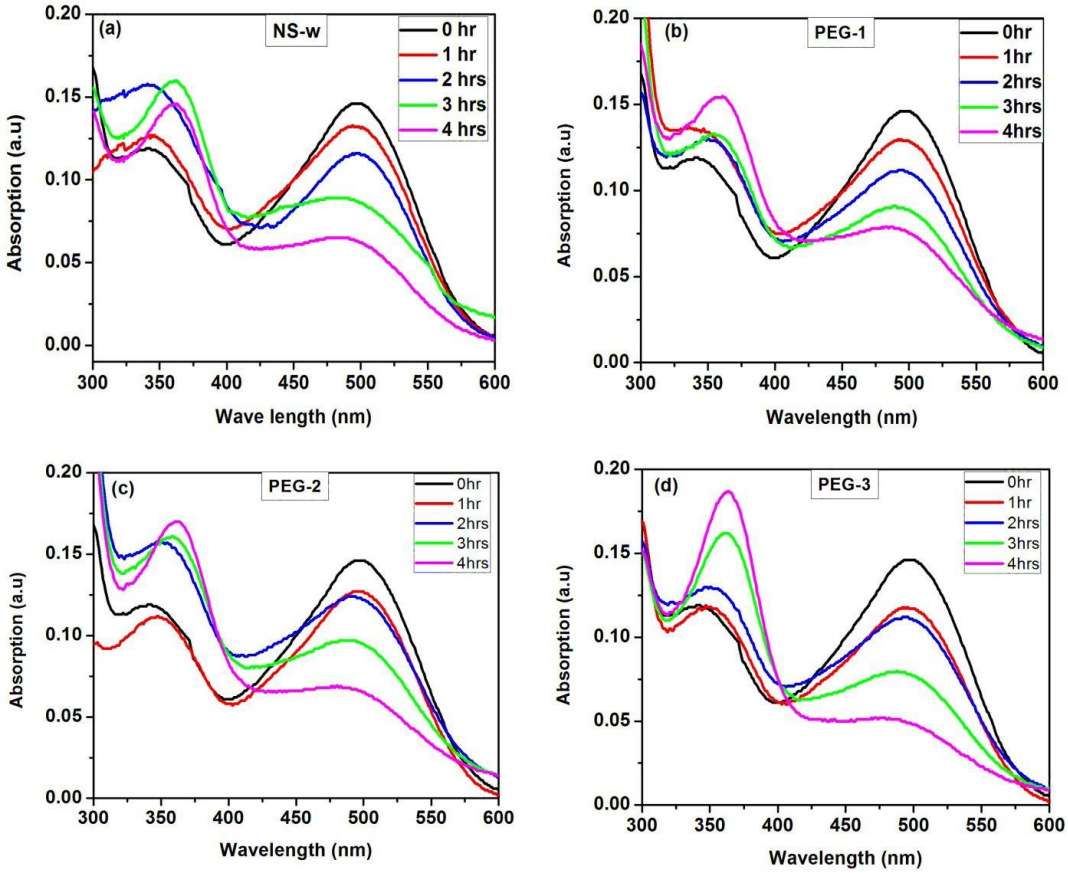

Figure 9.2: Absorption spectra of Congo red in the presence CuO nanostructures (a) NS-W, (b) PEG-1, (c) PEG-2 and (d) PEG-3 at different time intervals

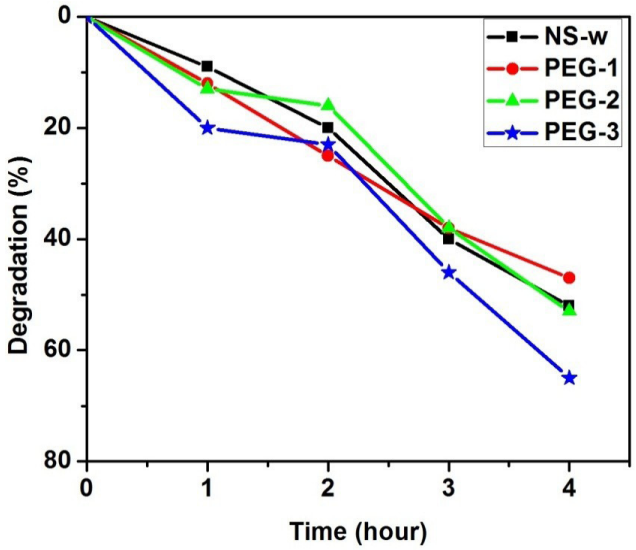

Figure 9.3: Degradation rate of Congo red in the presence of CuO nanostructures synthesized using PEG surfactant.

to the degradation of the dye compound and Peak 2 increases due to the formation of the intermediate compounds which absorbs light around 340 nm. From Fig 9.4 (a) and (b) it is noticed that, peak 2 of PVP-1 and PVP-2 attains maximum intensity only after four hours. It indicates that both the samples take four hours to degrade the dye into intermediate compounds. But, PVP-3 and PVP-4 attains maximum intensity at the end of 3rd hour and 2nd hour as shown in Fig. 9.4 (c), (d). It reveals that, PVP-3 and PVP-4 completely converted the dye into intermediate products at the end of 3rd hour and 2nd hour.

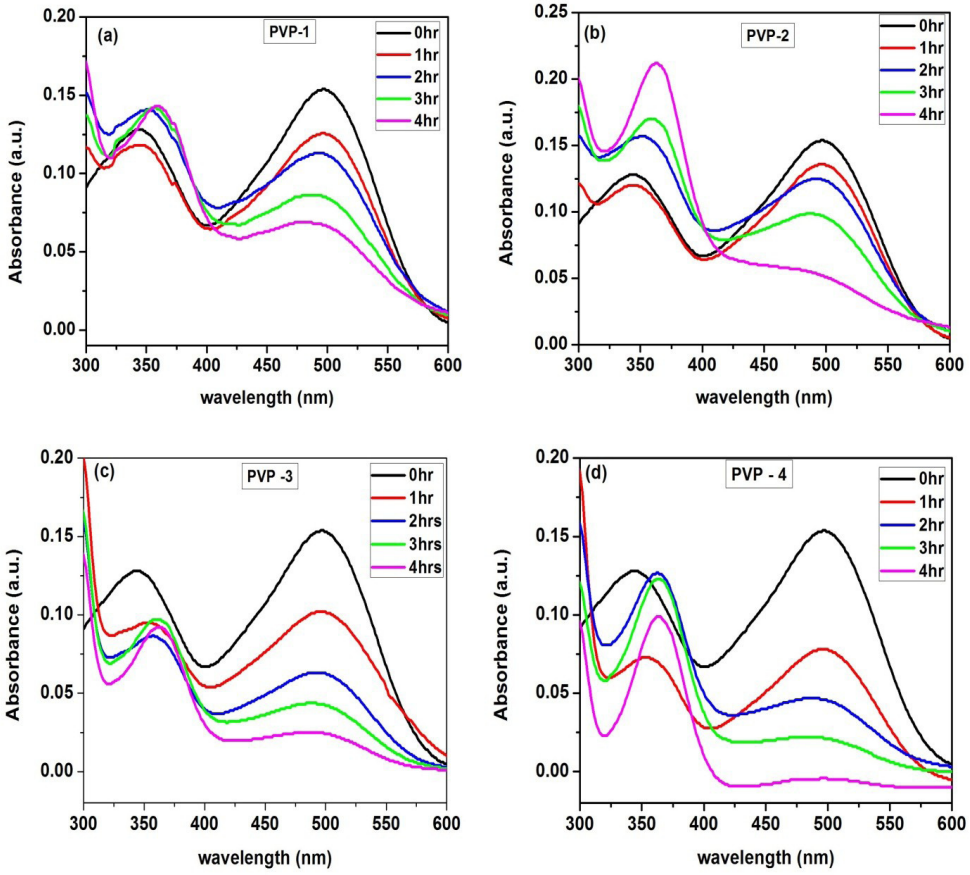

Figure 9.4: Absorption spectra of Congo red in the presence of CuO nanostructures for (a) PVP-1, (b) PVP-2, (c) PVP-3 and (d) PVP-4 at different time intervals

Degradation rate was calculated by the relation given in eqn. no. (9.8) and it was found as 55.5%, 64.5%, 84.2% and 100% for PVP-1, PVP-2, PVP-3 and PVP-4 respectively which is depicted in Fig. 9.5. Each material follows different degradation path it is shown in Fig .9.5. This is possibly due to the difference in morphology and the size of the PVP capped samples.

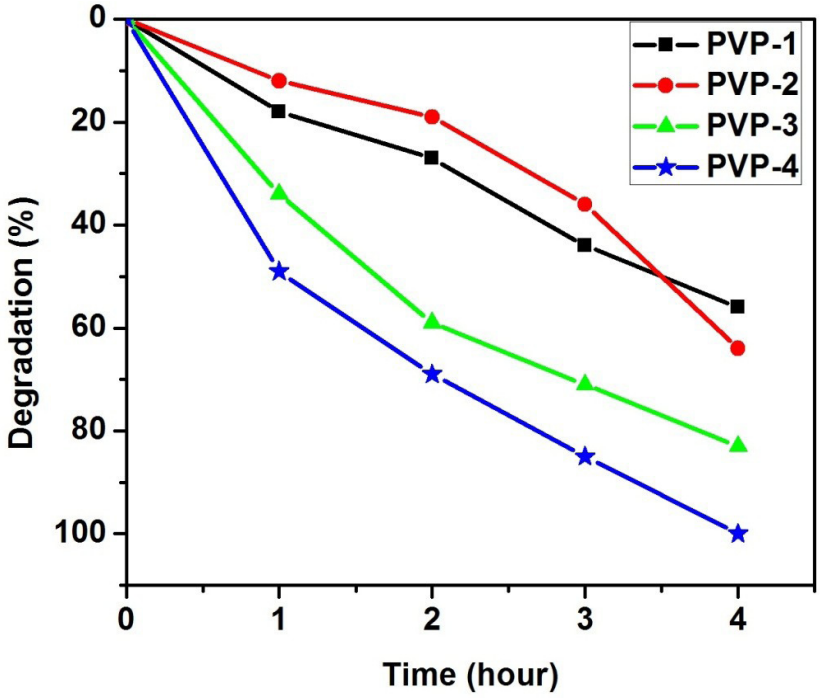

Figure 9.5: Degradation rate of Congo red in the presence of PVP capped CuO nanostructures at different time intervals.

PVP-4 was exhibiting excellent photo catalytic activity than other samples. XRD and particle size analyzer results confirm that PVP-4 has smaller particle size. Small particle and the high surface to volume ratio is the reason for this high Photocatalytic behavior. The high concentration of surfactant in PVP-4 creates more surface defects by reducing the particle size and the bulk defects was reduced by increasing the regularity of the grains. Bulk defects acts as center for recombination of electron hole pair. Increase in bulk defects increases the recombination possibility and reduces the photocatalytic

activity. In the case of surface defects, they increase the charge separation and improve the photo catalytic activity [Hua Xia Shi et al., 2014].

9.1.8. Photocatalytic properties of the CuO nanostructures synthesized with CTAB surfactant

Fig 9.6 shows the UV absorbance spectra of Congo red dye in regular time interval in the presence of synthesized photocatalyts (a) CT-1, (b) CT-2, (c) CT-3. Since CT-4 sample has residue surfactant which was confirmed by FTIR and XRD. So, we cannot use the material for application purpose. Degradation of dye material was shown by the decrement of absorption peak at each one hour interval. Another important result can be noticed from the Fig. 9.6 that is increment and decrement of peak-2 of the UV absorption spectra. During the degradation of dye materials, Peak-2 denotes the formation and destroys of intermediate products [Suresh Sagadevan & Priya Murugesan 2015]. The 2^{nd} peak of sample CT-1 reached its maximum only after four hours. This indicates CT-1 takes four hours to degrade the whole dye into intermediate products. But CT-2 and CT-3 attains the maximum of peak-2 at third and second hour. Degradation ability of the photocatalyst was calculated using the relation given in eqn. (9.8). After 4 hours illumination of sunlight, CT-1, CT-2 and CT-3 degrade 70%, 76% and 79% of the dye respectively. CT-3 has highest degradation capability among the four samples though the light absorbing intensity is lower than others. Photocatalytic activity is not only due to the improvement in the light absorption ability of the photocatalyst and also due to the available reaction sites. [Meshram et al., 2012]. Nature of active sites can be tuned in flower like morphology. Availability of higher number of active sites might be the reason for the higher degradation ability.

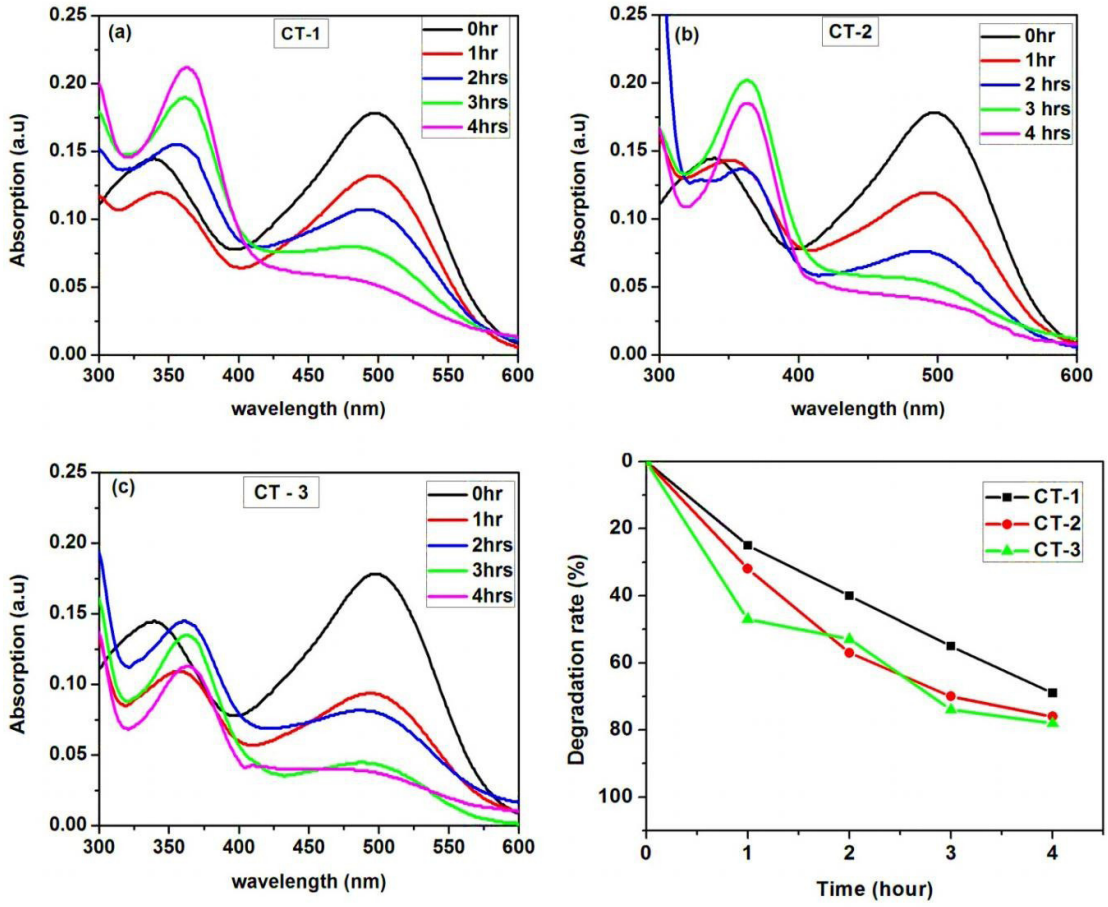

Figure 9.6: Absorption spectra of Congo red in the presence of CuO nanostructures for (a) CT-1, (b) CT-2, (c) CT-3 and (d) Degradation rate of dye at different time intervals.

9.1.9 Photocatalytic properties of the CuO nanostructures synthesized with Igepal surfactant

The effect of synthesized materials NS-S, IG-1 and IG-2 on the absorption spectral changes of the Congo red dye under the sunlight were shown in Fig. 9.7(a), (b) and (c) respectively. Fig. 9.7 (a) shows that Congo red has two absorption peaks around 490 nm (peak 1) and 340 nm (peak 2). Analysis of absorption data of NS-S sample at various time informed that after 4th hour, peak- 2 attain highest intensity. This shows that the dye material was completely changed into intermediate compounds after four hours.

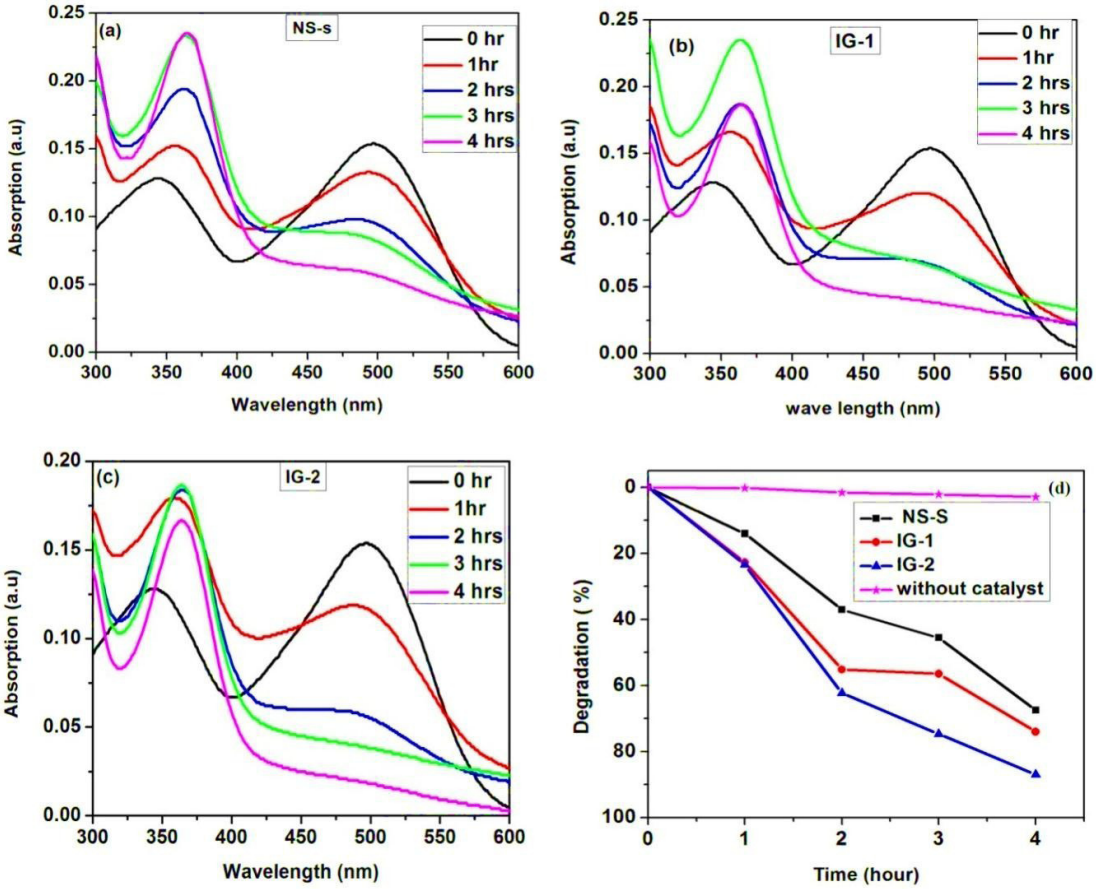

Figure 9.7: Absorption spectra of Congo red in the presence of CuO nanostructures for (a) NS-S, (b) IG-1, (c) IG-2 and (d) Degradation rate of dye at different time intervals

Similarly dye was completely degraded into intermediate compounds by IG-1 and IG-2 after 3rd and 2nd hour which is shown in Fig. 9.7 (b) and (c) respectively. After reaching the maximum intensity, peak 2 started to decrease which indicates the degradation of intermediate compounds into simple molecules. Thus the analysis of data not only informed the degradation ability of the material, but also confirms the mechanism of dye degradation.

The degradation percentage of dye, in the presence and absence of catalyst was calculated using the relation given in eqn. no. 9.8. Fig. 9.7 (d) reveals that, no significant photo degradation in the absence of the catalyst. The degradation percentage of NS-S,

IG-1 and IG-2 are 67%, 74% and 87% respectively. Here, IG-2 has relatively more ability to degrade the Congo red dye, due to smaller particle size. Smaller particle size of the nano materials increases the photo catalytic ability by reducing the possibility of recombination of charge carriers [Sonia et al., 2015]. Nano sponge like morphology adsorbs the dye comparatively in nanoparticle morphology of NS-S. The higher adsorption in IG-2 helps the hydroxyl ions act efficiently than in NS-S.

9.2. Super capacitor (CV studies)

9.2.1 Introduction

In the recent decades, there has been a significant amount of interest in developing new technologies to address the energy challenges. Since the petroleum resources are limited there is a need for alternate energy sources. Therefore, it has become a critical research area to manufacture cost effective, long lasting, durable, efficient and trustworthy energy storage devices. Although different types of energy storage devices like batteries, fuel cells and conventional capacitors have substantial significance. However, supercapacitors have played an imperative role to meet the emerging necessities. Supercapacitor technology has undergone considerable research and development in the recent years due to its potential to enable advancement of energy storage technology. Capacitors are fundamental electrical circuit elements that store electrical energy in the order of microfarads. A supercapacitor (SC) (ultracapacitor, or electric double-layer capacitor (EDLC)) is a high-capacity electrochemical capacitor with capacitance values in the order of Farad but with lower voltage limits.

9.2.2. Construction and working of supercapacitors

An ordinary capacitor consists of two plates separated by a relatively thick dielectric made from something like mica. When the capacitor is charged, positive

charges form on one plate and negative charges on the other, creating an electric field between them. The field polarizes the dielectric, so its molecules line up in the opposite direction to the field and reduce its strength. That means the plates can store more charge at a given voltage. Fig 9.8(a) shows the construction and charge formation in the conventional capacitor while the Fig 9.8(b) explain of supercapacitor.

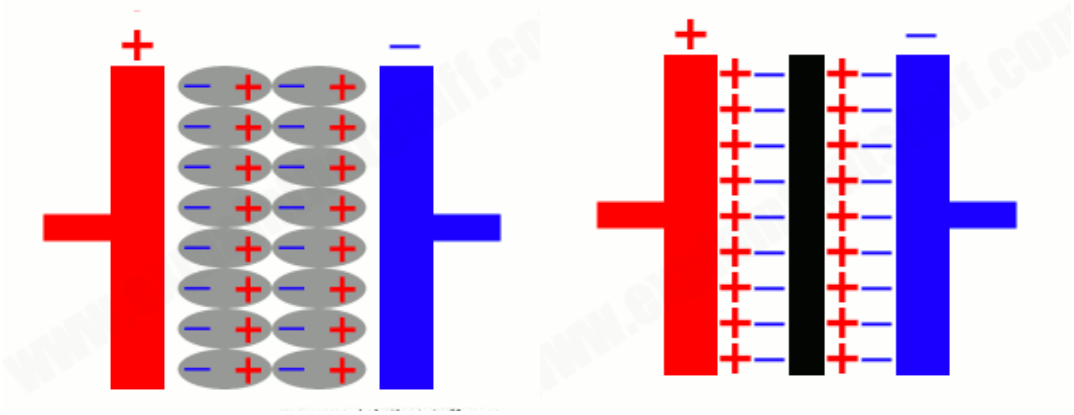

Figure 9.8: Schematic diagrams of (a) conventional capacitor and (b) Supercapacitor

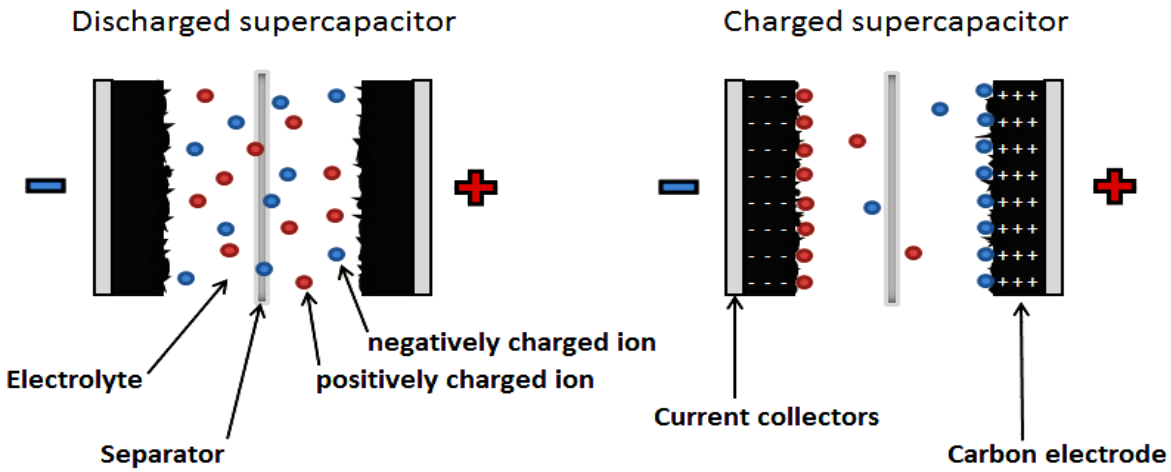

Figure 9.9: Elements of supercapacitor

In a supercapacitor, consists of two electrodes separated by a very thin insulator placed in container with electrolyte solution. When the voltage is applied, the positive electrode attracts the solvated anions while the cations are accumulated onto the negative electrode surface and an opposite charge forms on either side of the separator. These two parallel regions of charge form the source of the term "double layer." This effectively creates two capacitors that are series-connected by the electrolyte. This charge separation is naturally created at each liquid-solid interface. Charge separation is measured in molecular dimensions (*i.e.*, few angstroms). (Compared to the dielectric, range in thickness varies from a few microns to a millimeter or more in a conventional capacitor). Fig 9.9 (b) explains the position of solvated ions in the charging and discharging stages of a supercapacitor.

9.2.3. Materials used in Electrodes

Recently 3 category of materials was using for electrodes and they are

- Activated carbons
- Metal oxides
- Conducting polymers

9.2.3.1. Activated carbons

Activated carbons find application in electrodes for EDLC type supercapacitors where it is a commonly used material. These carbons are known for their large surface area [Pandolfo 2006]. Their large surface is due to their highly porous structure. They are also less expensive compared to other carbon materials. The high porosity can cause some problems. Pores that may be smaller than the electrolyte ions will not contribute to charge storage [Shi et al., 1996, Qu et al., 1998]. Also high porosity can lead to poor conductivity, causing the maximum power density to be limited [Frackowiak et al.,

2001] Also, a distributed electrolyte resistance may be created, which restricts charge and discharge rates [Pandolfo 2006].

9.2.3.2. Metal oxides:

Metal oxide like RuO_2 [Hu et al., 2006], CuO, CoO_3 [Cao et al., 2005], Fe_3O_4 [Wang et al., 2006] MnO_2 [Pang et al., 2000], NiO [Rajendra Prasad et al., 2004], SnO_2 can be used as electrodes. Compared to the reported capacitance values for CuO electrodes are still low (<32%) though it has a high theoretical capacitance values around 1783 F/g within the window of 0.68 V [Senthilkumar et al., 2013].

9.2.3.3 Conducting polymers

Conducting polymers are being employed in supercapacitors because their relatively high capacitance and conductivity, and low equivalent series resistance. Conducting polymers have redox storage capability as well as providing a large surface area and therefore it is employed in supercapacitors for high capacitance. [Mastragostino et al., 2001] In the meanwhile such compounds can be doped to have metallic conductivity which is a desirable property to serve as supercapacitor electrode materials of the commonly used conducting polymers include polypyrrole, polyaniline (PANI) and poly-(3,4- ethylene dioxy thiopheneor (PEDOT), which have been shown to exhibit specific capacitance comparable to that of metal oxides like ruthenium oxide [Zou et al., 2007, Fan et al., 2006, Gupta et al., 2006]. The challenges with conducting polymers include a lack of efficient n-type doped (negatively charged) conducting polymer material [Xu et al., 2006]. Another problem is the insufficient mechanical stability during charge-discharge cycles due to mechanical stress [Arbizzani et al., 2001, Frackowiak et al., 2006].

9.2.4 Composite electrodes

Composite materials are used in hybrid type supercapacitors.

Composite materials involve combinations of

(i) Carbon materials with metal oxides [Alfred et al., 2012] NiO- Carbon [Wang et al., 2003]

(ii) Carbon materials conducting polymers [Jurewicz 2001]

(iii) Metal oxides and conducting polymers [Frackowiak et al., 2006]

Composite electrodes thereby incorporating aspects of both EDLC and pseudocapacitor materials, namely a capacitive double layer of charge and faradaic mechanisms On the basis of electrodes supercapacitors categorized into two groups such that Symmetric supercapacitors : in which the electrodes used in this supercapacitor are made up of same material. Usually in this type of supercapacitors consists of activated carbon materials electrode, metal oxides [Hui Xia et al., 2012], or composite electrodes

9.2.5 Categories in supercapacitor

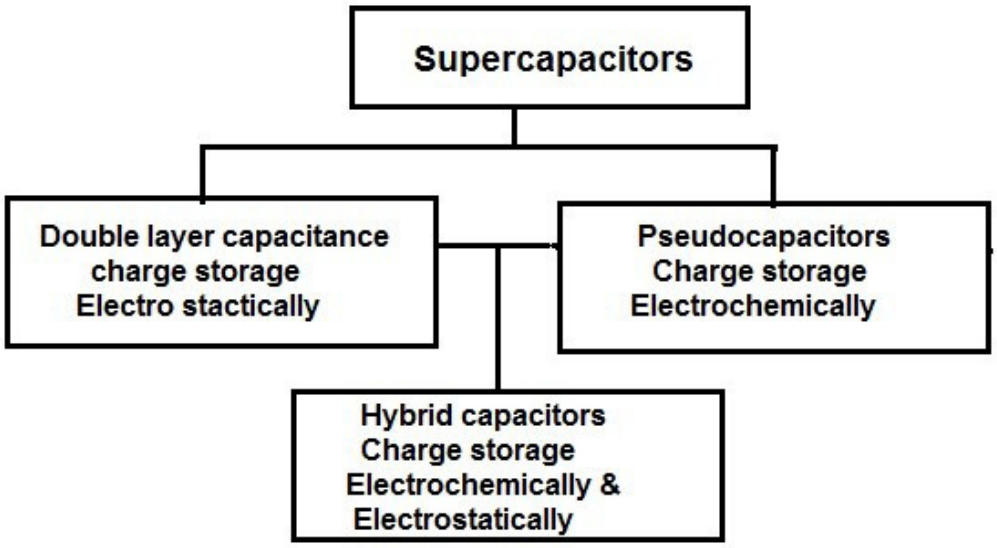

On the basis of storage mechanism supercapacitors categorized as (i) Electric double layer capacitor and (ii) Pseudo capacitor and (iii) Hybrid capacitor

9.2.5.1 Electric double layer capacitor

Electrostatic double-layer capacitors use carbon electrodes or derivatives with much higher electrostatic double-layer capacitance than electrochemical pseudo-capacitance, achieving separation of charge in a Helmholtz double layer at the interface between the surface of a conductive electrode and an electrolyte. The separation of charge is of the order of a few angstroms (0.3–0.8 nm), much smaller than in a conventional capacitor. The symmetrical and rectangular cyclic voltammetric curve is a trademark for double layer capacitance [Jayalakshmi et al., 2007].

9.2.5.2 Pseudo capacitor

Electrochemical pseudo capacitors use metal oxide or conducting polymer electrodes with a high amount of electrochemical pseudo capacitance. Pseudo capacitance is achieved by Faradaic electron charge-transfer with redox reactions, intercalation or electrosorption.

9.2.5.3 Hybrid capacitors.

Hybrid capacitors, such as the lithium-ion capacitor, use electrodes with differing characteristics: one exhibiting mostly electrostatic capacitance and the other mostly electrochemical capacitance.

9.2.6 Applications

Supercapacitors are used in applications requiring many rapid charge/discharge cycles rather than long term compact energy storage

- Releasing the power in acceleration

- Starting power in start-stop systems
- Regulate voltage to the energy grid
- Capture power when lowering loads and assisting when loads are lifted
- Back-up power in any application where quick discharge (or charge) is required
- Regenerative braking in vehicles, cranes, trains and elevators
- Backup power sources for, load-leveling, engine start or acceleration for hybrid vehicles and electricity storage generated from solar or wind energy.

  [Jayalakshmi & Balasubramanian 2008]

9.2.7 CuO nanostructures as supercapacitors

Transition metal oxides are considered as ideal electrode materials for pseudo capacitors, as they provide variable oxidation states for efficient redox charge transfer [Endut et al., 2013]. Some of the oxides which have been studied as SC electrode material are NiO, Ni $(OH)_2$, MnO_2, Co_2O_3, IrO_2, FeO, TiO_2, SnO_2, V_2O_5 and MoO. None of these oxides are used in commercial production of EDLCs and they are still in lab-scale research. Among the metal oxides, CuO is one of the promising candidates due to its low cost, no toxicity, chemical stability and environmental friendly. However, little work has been carried out on the application of CuO as super capacitor electrodes because of their low electrical conductivity and unstable cycling performances [Dubal et al., 2013(A)]. Hang et al first reported the usage of copper oxide electrodes in super capacitors at 2008 [Hongxia Zhang et al., 2008]. After that many groups working with CuO super capacitors, especially Dubal et al proved that specific capacitance of CuO widely depends on morphology and synthesis method [Dubal et al., 2013 (B)]. In the current work, we synthesized the copper oxide nano structures by surfactant assistant wet chemical method and solid state reaction method. Table 9.1 shows the literature survey of the electrochemical properties of the CuO nanostructures with the three electrode

configuration. Meryl D. Stoller et al., proved that the value of specific capacitance is varied with the testing methods and cell configuration. According to him, three electrodes cell calculations yield double the value of capacitance compared to packaged super capacitors, but the two electrode cell measurements closely matches the packaged ones [Stoller et al., 2010]. Seyyed Ebrahim reported the two electrode asymmetric super capacitors using CuO and AC electrodes [Seyyed Ebrahim et al., 2015]. Here we demonstrate, for the first time electrochemical Properties of CuO nanostructures using two electrode beaker cells with symmetrical configuration. The prepared electrodes were placed inside the beaker such that they face to each other with small gap. The beaker cell filled with electrolyte such that the coated part of electrode fully immersed in electrolyte. 1M Na_2SO_4 was used as electrolyte and the CV were taken in the potential window of 0 to 0.5 V.

9.2.8. Electrode preparation

The electrode was prepared to construct supercapacitor. Steps involved in the preparation of CuO electrodes were shown in Fig.9.10. The electrode was prepared from slurry mixture, which was composed of 80wt% copper oxide, 15 wt % carbon black (Alfa Aesar) and 5% poly-vinylidene fluoride (PVDF) binder in N-methyl-2-pyrrolidone

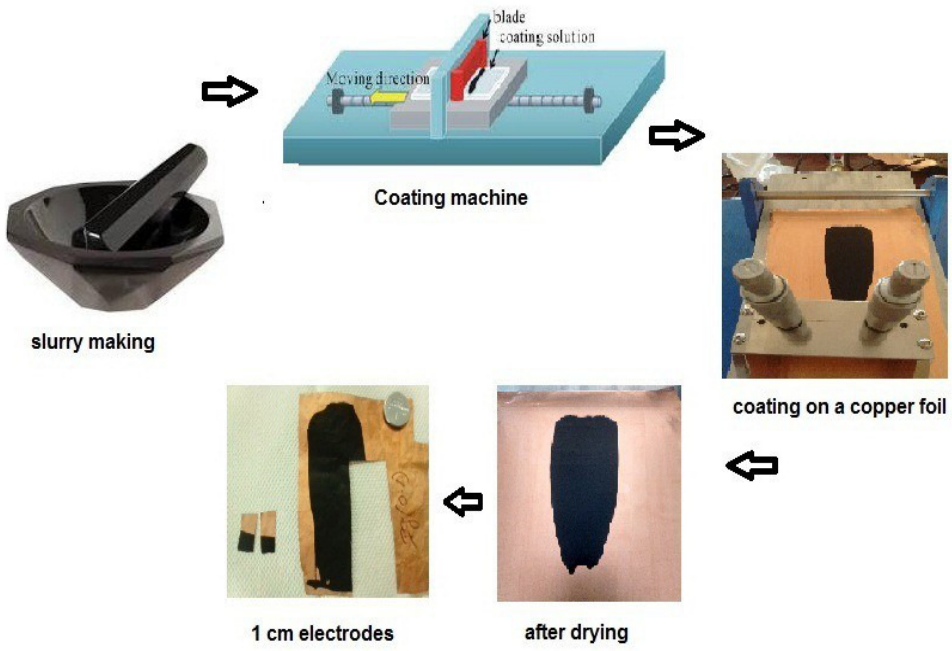

Figure 9.10: Electrode preparation

(NMP) solvent. The slurry was coated on a cleaned copper foil substrate using the doctor blade technique. Copper foil was cleaned by acetone before coating of slurry mixture. Coated foil was dried at 120°C for 12 hours at vacuum to completely remove the solvent and then it was pressed under roller press. Next, electrode was cut into piece of (~3 x 1) dimension which contained 1cm X 1cm of coated CuO. Electrical connections were made from empty copper foil.

9.2.9 Cyclic Voltammetry Studies

Fig. 9.11 (a-f) shows the CV curves of the CuO nanostructures electrodes recorded with scan rates 5, 10, 25, 50, 75 and 100 mVs^{-1}. All the Cyclic Volta grams having relatively rectangular shape and there is no clear redox peaks which indicative of charge storing mechanism is not fully due to the Pseudo capacitance mechanism. Generally metl oxides are pseudo capacitors and the most of researchers reported CV

curve for CuO electrodes having redox peaks [Shen et al., 2014]. The current study deals with symmetric super capacitors in which very feeble potential difference is created between same electrodes. This may enough to separate the ions of electrolyte and not enough for intercalation of ions into the CuO electrodes. The shape of the CV curve has no noteworthy change over higher scan rates which indicate the good electronic conductivity within the CuO nano structures (Awale et al., 2016). But the voltammetry current is directly proportional to the scan rates of CV, indicating an ideally capacitive behavior [Karthikeyan & Sang-Jae 2013]. The measured currents were normalized with the one electrode mass. The shape of the CV curve and voltammetry current differs for each CuO nanostructure electrodes. This may due to the different morphology, electronic conductivity and dielectric properties of the samples. Among all the electrodes CT-3 having perfect rectangular shape even at the high scan rate. CV curve of the IG -2 having redox peak which is indicates the occurring of some more redox reactions rather than other samples. This may due to the sponge like morphology of the material allows the electrolyte ions even at small potential difference.

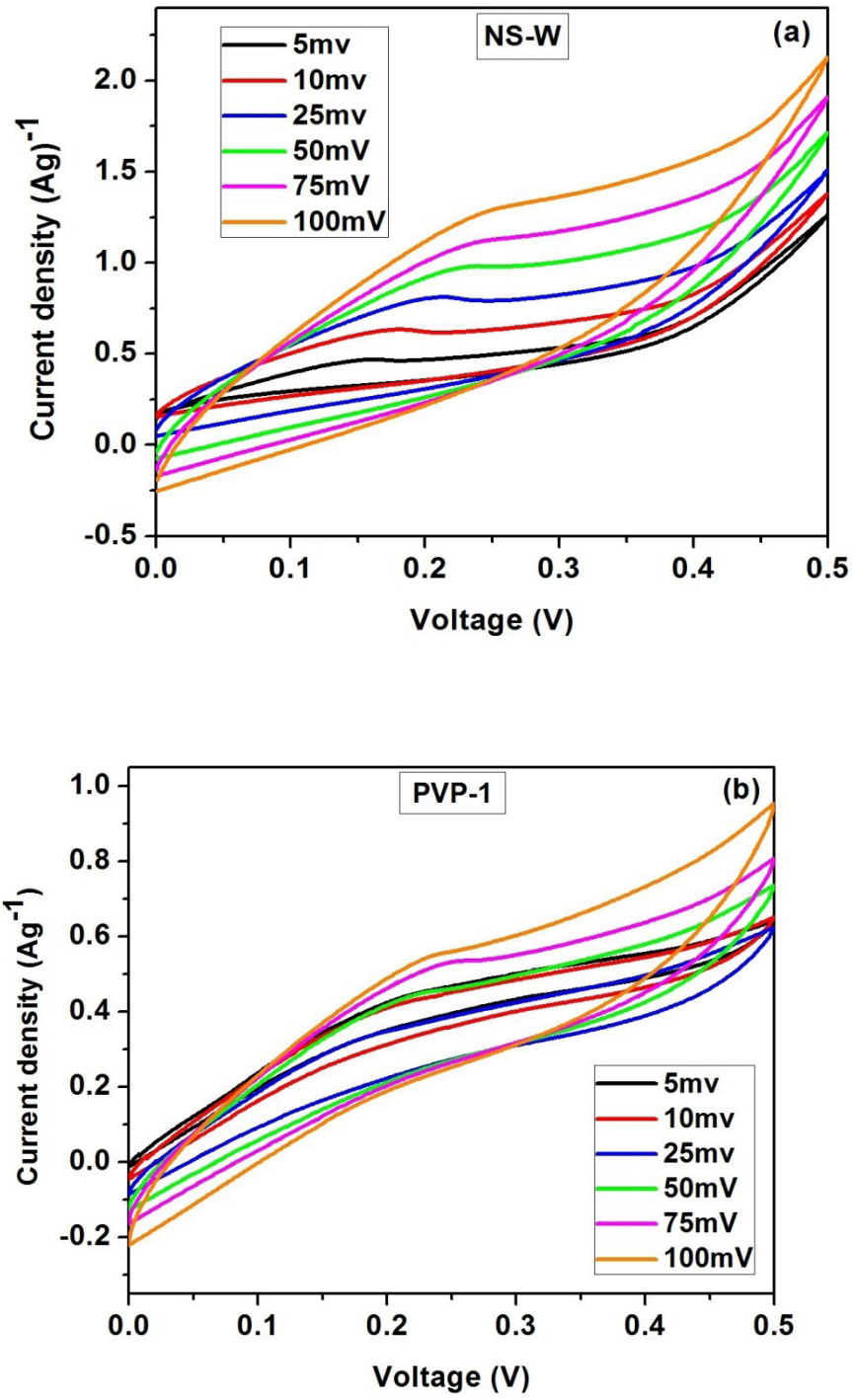

Figure 9.11: CV graphs of CuO nanostructures (a) NS-W (b) PVP-1

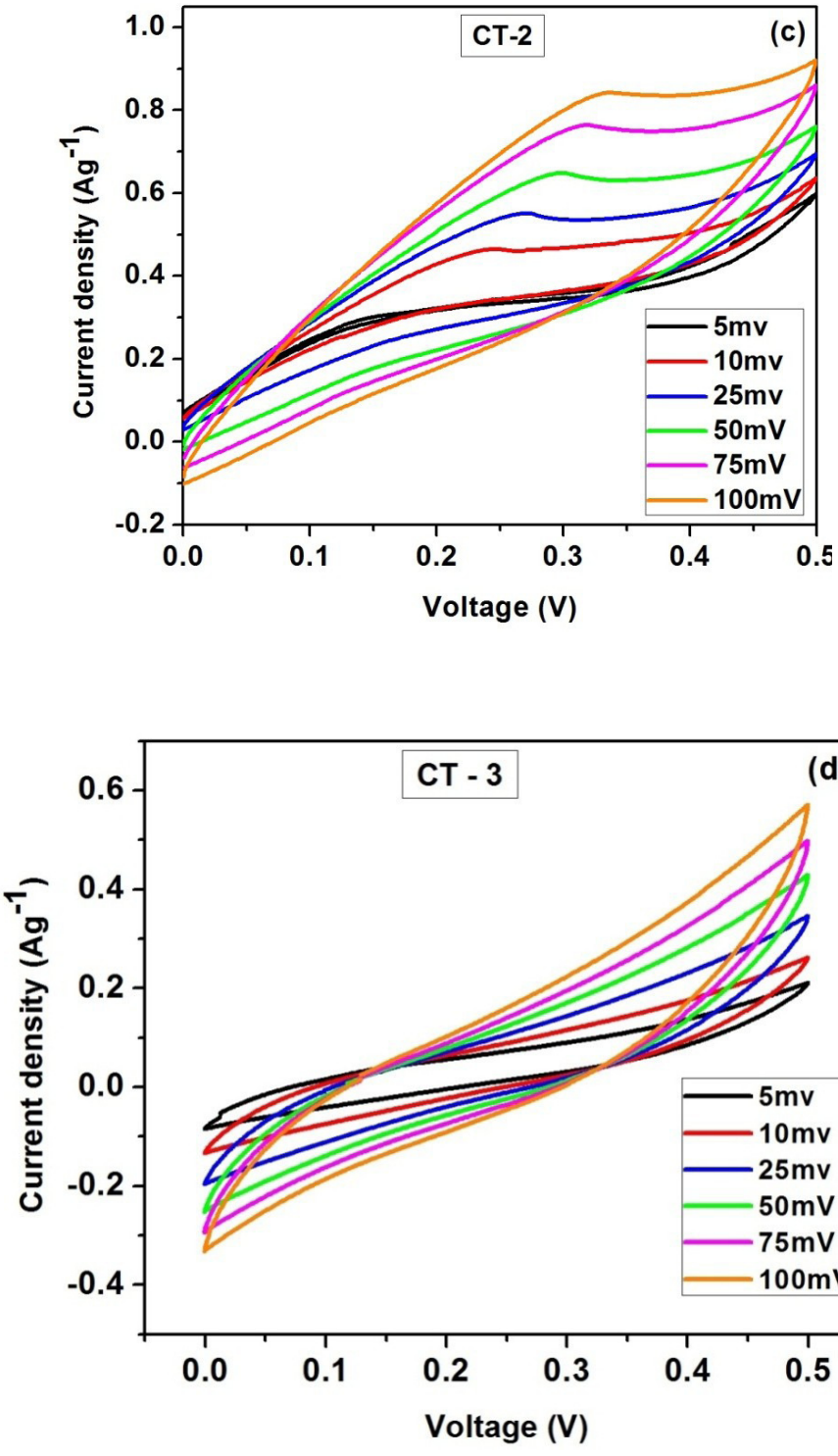

Figure 9.11: CV graphs of CuO nanostructures (c) CT-1 (d) CT-3

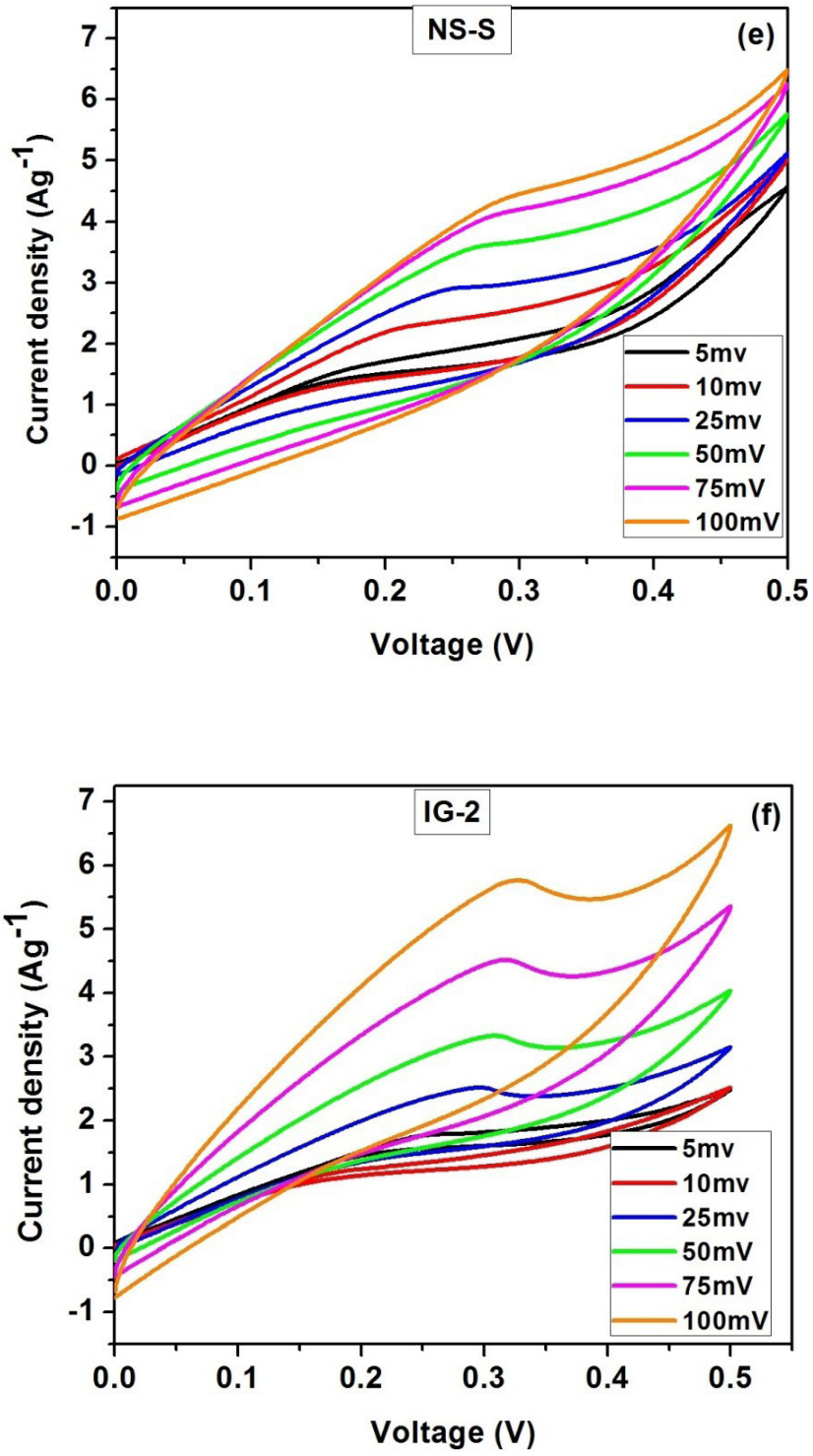

Figure 9.11: CV graphs of CuO nanostructures (e) NS-S (f) IG-2

The specific capacitance of one CuO electrode was calculated using the formula $C_s = \frac{\int IV\,dV}{vs}$ [Dubal et al., 2013] where C_s is the Specific capacitance, I is average current which is predicted by integrate the curve using EC Lab software, v is potential window and s indicates the scan rate. For a capacitor with two electrodes are needed with doubled weight and half the total capacitance. The difference between single electrode values and for the complete capacitor is factor of four [Kotz et al., 2000]. The specific capacitance of the cell was calculated by the relation $C_{cell} = \frac{C_s}{4}$ Specific capacitance values of one electrode and cell for different CuO nanostructures were tabulated in table one.

Table 9.1: Specific capacitance values of the synthesized CuO nanostructures.

Scan rate mVs^{-1}	Specific capacitance (F/g)											
	NS-W		CT -1		CT-3		PVP -1		NS-S		IG-2	
	S_e	S_{cell}	S_e	S_{cell}	S_e	S_{cell}	S_e	S_{cell}	S_e	S_{cell}	S_e	S_{cell}
5	208	51	132	33	20	5	152	38	747	186	572	143
10	118	29	73	18	10	2.5	72	18	414	104	249	62
25	51	13	30	8	4.5	1.1	24	6	171	43	135	33
50	28	7	16	4	2.5	0.63	13	3	94	24	82	20
75	20	5	11	3	1.8	0.47	9	2.3	66	17	69	17
100	17	4	9	2	1.5	0.39	7.5	1.9	52	13	62	16

Even though all the samples have the useful capacitance value, NS-S exhibits highest C_s it has the C_{cell} value 186 F/g. 2E configuration cell using NS-S electrodes has pretty capacitance value when compared with the reported literatures which has three electrode configurations.

9.3. Conclusions

This chapter deals with the basic mechanism and experimental part of the photo degradation and Supercapacitor applications. Sunlight driven photocatalytic CuO nanostructures was synthesized using various surfactant with different concentration was studied using Congo red as the model dye. Samples synthesized with PEG surfactant shows small differences in degradation rate. PEG-3 has 65% degradation rate and it is the highest ability among the PEG samples. In the case of PVP group samples degradation rate is linearly increases with the increase in crystallite size. PVP-4 has 100% degradation rate on Congo red solution within four hours. This is the only material attained this ability among the synthesized materials. It may due to the smaller particle size which reduces the bulk defects which can reduce the recombination ability of the e-h pairs. Reduction of bulk defects was confirmed by low dc conductivity of PVP-4 among the samples. The CTAB group of samples not given much different in the degradation rate, but they have the ability to degrade in the range 70%. Among the above samples, CT-3 has highest degradation rate 79%. IG-2 degrades the dye solution up to 87% in four hours and provides better photo catalytic property than NS-W and IG-1. Even with the smaller crystallite size NS-W has lowest degradation 52%, NS-S has 67% degradation and it has high crystallite size compared with NS-W. This may due to the morphological differences between them. PEG-1 is the sample has lowest degradation rate among all the samples. The presence of defects in PEG-1 may be the reason for red shift in band gap and higher conductivity properties of PEG-1.The present results elucidated that morphology controlled synthesis of nanomaterials is a novel technique to design better performance sunlight driven photo catalyst.

Symmetric super capacitor was built using CuO electrodes with two electrode configuration and CV measurements were carried out. High specific capacitance value of 747 F/g for an electrode and 186 F/g for one Cell was obtained for the sample synthesized by solid state reaction method.

CHAPTER – X

SUMMARY, CONCLUSIONS AND SUGGESTIONS FOR FUTURE WORK

10.1 Summary and Conclusions

In this project we have synthesized and characterized the CuO nanostructures. Totally eighteen samples were synthesized. Three samples synthesized using EG as the surfactant namely EG-1, EG-2 and EG-3. Likewise three samples synthesized using PEG-400 as the surfactant namely PEG-1, PEG-2 and PEG-3, taking PVP as the surfactant PVP-1, PVP-2, PVP-3, PVP-4 was synthesized and CTAB was taken as the surfactant CT-1, CT-2,CT-3, CT-4 nanostructures were synthesized. And also the two samples IG-1, IG-2 synthesized using Igepal as the surfactant. The sample NS-W was synthesized without using surfactant by wet chemical and NS- S was synthesized without surfactant by solid state reaction method. The result of the characterization studies and applications were summarized in Table 10.1. From the Table 10.1 following conclusions can be drawn.

The synthesized material, crystallite sizes varies from 7.7 nm to 44 nm. CT-4 has the smallest crystallite size whereas NS-S has the largest crystallite size. SEM studies elucidated the presence of various morphologies such that Nano flakes, nano leaves, nano rods, now flowers, nano sheets, nano particles, nano granules and nano sponge for different surfactants. Among the surfactants used in this project CTAB has the excellent structure directing properties in current experimental condition. UV studies elucidated that the samples synthesized using EG and PEG-400 having same range of band gap values. In the same way, PVP samples and CTAB samples has comparable band gap value range. The samples synthesized by solid state reaction method have the high band gap values compared with the materials prepared by Wet chemical method. IG-1and NS-S has the highest bandgap values 4.59 and 4.91 eV respectively. EG-2 has the

Table 10.1: Summarization of the results

Surfactant	Sample code	Crystallite size (XRD)	Optical band gap	Morphology	DC conductivity at room temperature	Degradation Percentage (%)	Specific capacitance (F/g)
EG	NS-W	21	1.73	nanoflakes	3.40 E-07	52	51
	EG-1	23	2.29		1.49 E-07		
	EG-2	25	1.47		6.08E-07		
	EG-3	16	1.48		9.37E-08		
PEG-400	PEG-1	40.4	1.68	Nano leaves	2.36 E-07	47	
	PEG-2	37.3	2.00	Nanoflakes	1.19 E-07	53	
	PEG-3	35.7	2.23	Nanorods	1.09 E-07	65	
PVP K_{30}	PVP-1	35.7	3.64	Nanoleaves	2.3E-7	55.5	38
	PVP-2	32.0	3.76		3.9E-8	64.5	
	PVP-3	28.1	3.79		1.7E-9	84.2	
	PVP-4	22.2	3.48		6.2E-10	100	
CTAB	CT-1	32.8	3.12	Nanoflakes	6.8 E-7	70	33
	CT-2	19.2		Nanoleaves	4.9 E-7		
	CT-3	17.9	3.16	Nanoflowers	2.26 E-7	76	
	CT-4	7.7	3.2	Nanosheets	1.04 E-9	79	5
Igepal 210	NS-S	44	4.91	Nanoparticle	9.71E-06	67	186
	IG-1	37	4.59	Nanogranules	2.10E-06	74	
	IG-2	25	4.27	nanosponge	9.57E-06	87	143

smallest band gap value 1.47. NS-S has the high dc conductivity value 9.76 x 10^{-6} whereas the PVP-4 has the lowest electrical conductivity. In the photocatalytic dye degradation, it can be concluded that PEG-1 sample has the lowest degradation rate among all the samples. At the same time, PVP-4 degraded the Congo red fully (100%) within four hours. Symmetric super capacitor was built using CuO electrode with the two electrode configuration and the CV measurements were carried out. NS-S sample has high specific capacitance value 186 F/g for one cell.

The Conclusions are as follows

- Appropriate amount of Ethylene glycol can be used as surfactant because it reduced the particle size.
- CTAB can act as the structure directing agent in high alkaline condition where as EG and PEG-400 has less structure directing properties.
- Igepal -210 can be used as the surfactant and structure directing agent for synthesis of Copper oxide nanostructures.
- From the analysis of all the samples, it can be concluded that, the particle size are reduced, Conductivity properties are decreased but the photocatalytic properties is enhanced.
- For electrical applications, solid state reaction method is suitable as well as wet chemical method is suitable for photocatalytic applications.

10.2. Suggestions for future work

The research raised many questions that were not initially postulated and provided. Many conclusions of this study need to be revisited. Future studies want to conduct to answer questions pertaining to details, which can improve existing nanomaterials performance or motivated to focus on developing new nanomaterials for environmental applications. In this project, EG surfactant CuO nanostrucutres prepared

by wet chemical and Igepal surfactant CuO nanostructures by Solid state reaction method. In future, we can synthesize EG surfactant CuO by Solid state reaction method and Igepal surfactant CuO by wet chemical method. Enhanced Photocatalytic property and excellent electrochemical performance may achieve by this process. This is also a worthwhile future study.

Thus the investigation has proved that, the CuO nanostructures with different morphology can have the diverse catalytic characteristics on the treatment of Congo red. The study may be extended, using the treatment of waste water with single or multi components of contaminants. To produce the good quality potential catalyst CuO, Comparison study with various dye components can be done in future. CV studies confirmed that CuO can use as electrodes for symmetric supercapacitor. So the scheme of the construction of symmetric and asymmetric packed cell supercapacitor with suitable electrolyte was explored.

LIST OF REFERENCES

1. Ahmad, M, Rafiq, M. A, Rasool, K, Imran, Z & Hasan, M. M 2013, 'Dielectric and transport properties of Bismuth sulfide prepared solid state reaction method', Journal of Applied Physics, vol. 113, pp. 043704–043706.
2. Alfred Chidembo, Seyed Hamed Aboutalebi, Konstantin Konstantinov, Maryam Salari, Brad Winton, Sima Aminorroaya Yamini, Ivan P. Nevirkovets & Hua Kun Liua 2012, 'Globular reduced graphene oxide-metal oxide structures for energy storage applications', Energy Environmental Science, vol. 5, pp. 5236- 5239
3. Anita Sagadevan Ethiraj & Dae Joon Kang, 2012,'Synthesis and characterization of CuO nanowires by a simple wet chemical method', Nanoscale Research Letters, vol. 7, no.70, pp.1-5.
4. Arbizzani, C, Mastragostino, M & Soavi, F 2001, 'New trends in electrochemical supercapacitors', Journal of Power Sources, vol. 100, pp. 164-170.
5. Asha Radhakrishnan, A & Baskaran Beena, B 2014, 'Structural & Optical Absorption Analysis of CuO Nanoparticles', Indian Journal of Advances in Chemical Science, vol. 2, no.2, pp. 158-161.
6. Ashok Kumar, Singh, B.P, Choudhary, R.N.P & Thakur, A.K 2006, 'Characterization of electrical properties of Pb-modified $BaSnO_3$ using impedance spectroscopy', Materials Chemistry and Physics, vol. 99, pp. 150–159.
7. Awale, D.V, Bhise, S.C, Patil, S.K, Vadiyar, M.M, Jadhav, P.R, Navathe, G.J, Kim, J.H, Patil, P.S, Kolekar, S.S 2016, 'Nanopetals assembled copper oxide electrode for supercapacitor using novel 1-(10-methyl-20-oxo-propyl)-2,3-dimethylimidazolium chloride ionic liquid as an electrolyte', Ceramics International, vol. 42, pp.2699-2705.
8. Ayekpam Bimolini Devi, Dinesh Singh Moirangthem, Narayan Chandra Talukdar, Damayanti Devi, M Rajen Singh, N & Meitram Niraj Luwang, 2014 'Novel synthesis and characterization of CuO nanomaterials: Biological applications', Chinese Chemical Letters, vol. 25, no.12, pp. 1615-1619
9. Azar Sadollahkhania, Zafar Hussain Ibupotoa , Sami Elhaga , Omer Nura & Magnus Will &era 2014, 'Photocatalytic properties of different morphologies of CuO for the degradation of Congo red organic dyes', Ceramics International, vol. 40, pp. 11311–11317.

10. Baiju Vidyadharan, Izan Izwan Misnon, Jamil Ismail, Mashitah M. Yusoff & Rajan Jose 2015, 'High performance asymmetric supercapacitors using electrospun copperoxide nanowires anode', Journal of Alloys and Compounds, vol. 633, pp. 22 – 30.
11. Behr, B, Nayak, P & Choudhary, R.N.P 2008, 'Structural & impedance properties of $KBa_2V_5O_{15}$ ceramics', Material Research Bulletin, vol. 43, pp. 401.
12. Behrouz Shaabani, Ebrahim Alizadeh-Gheshlaghi, Yashar Azizian – Kalandaragh & Ali Khodayari 2014, 'Preparation of CuO nanopowders & their catalytic activity in photodegradation of Rhodamine-B', Advanced Powder Technology, vol. 25, pp. 1043-1052.
13. Bello, A, Dodoo-Arhin, D, Makgopa, K, Fabiane, M & Manyala, N 2014, 'Surfactant Assisted Synthesis of Copper Oxide (CuO) Leaf-like Nanostructures for Electrochemical Applications', American Journal of Materials Science, vol.4, no. 2, pp. 64-73.
14. Bojun Heng, Chen Qing, Daming Sun,Bixiao Wang, Hai Wang & Yiwen Tang 2013,'Rapid synthesis of CuO nanoribbons and nanoflowers from the same reaction system, & a comparison of their supercapacitor performance', RSC Advances, vol.3, pp.15719- 15726.
15. Boujday, S, Wunsch, F, Portes , P, Bocquet, J.F & Justin, C.C 2004, 'Photocatalytic & electronic properties of TiO_2 powders elaborated by sol–gel route and supercritical drying', Solar Energy Materials & Solar Cells, vol. 83, pp.421- 433.
16. Cao, L, Lu, M & Li, H.L 2005, 'Preparation of Mesoporous Nanocrystalline Co_3O_4 and Its Applicability of Porosity to the Formation of Electrochemical Capacitance', Journal of Electrochemical Society, vol. 152, no. 5, pp. A871-A875.
17. Carmichael, H. J, Kochan, P & Sanders 1996, B. C, 'Photon Correlation Spectroscopy', Physical review letters, vol. 77, no. 4.
18. Chonghai Deng, Hanmei Hu, Xinqing Ge, Chengliang Han, Difang Zhao & Guoquan Shao 2011, 'One-pot sonochemical fabrication of hierarchical hollow CuO sub-microspheres', Ultrasonics Sonochemistry, vol. 18, pp. 932–937.
19. Christy, A.J, Nehru, L.C & Umadevi, M 2013, 'A novel combustion method to prepare CuO nanorods & its antimicrobial & photocatalytic activities', Powder Technology, vol. 235, pp. 783- 786.

20. Chuanyue Hu, Jun Guo & Jin Wen, 2013, 'Hierarchical nanostructure CuO with peach kernel-like morphology as anode material for lithium-ion batteries', Ionics, vol. 19, no. 2, pp. 253- 258.
21. Cole, K.S &Cole, K.S 1941, 'Dispersion & Absorption in Dielectrics I. Alternating Current Characteristics', Journal of Chemical Physics, vol. 9, pp. 341 – 351.
22. Cudennec, Y & Lecerf, A 2003, 'The transformation of $Cu(OH)_2$ into CuO revisited', Solid State Science, vol. 5, pp. 1471–1474.
23. Cullity, B.D &. Stock S.R, 1978, Elements of X-Ray Diffraction, Third edition, Prentice Hall
24. Daries Bella, R. S, Karthick prabhu, S, Maheswaran, A, Ambika, C, Hirankumar, G & Premanand, D 2015, 'Investigation of the Ionic conductivity & dielectric measurements of poly (N- Vinyl Pyrrolidone) - Sulfamic acidpolymer complexes', Physica B, vol. 458, pp. 51-57.
25. Das, A, Bonu Venkataramana , Partheephan , D, Prasad, A.K, Dhara, S, Tyagi, A.K 2013, 'Facile synthesis of nanostructured CuO for low temperature NO_2 sensing', Physica E, vol. 54, pp. 40–44.
26. Das, P.S, Chakraborty, P.K, Banarji Behra & Choudhary, R.N.P 2007, 'Electrical properties of $Li_2BiV_5O_{15}$ ceramics', Physica B, vol. 395, pp. 98 – 103.
27. Deepthi, K.R, Pandiyarajan, T & Karthikeyan, B 2013, 'Vibrational, giant dielectric and AC conductivity properties of agglomerated Copper oxide nanostructures', Journal of Material Science: Materials in Electronics, vol. 24, pp.1045-1051.
28. Du, G.H & Van Tendeloo, G 2004, 'Cu $(OH)_2$ nanowires, copper oxide nanowires and copper oxide nanobelts', Chemical Physics letters, vol. 393, pp. 64-69.
29. Dubal, D. P, Gund, G. S, Rudolf Holze, Harsharaj S. Jadhav, Lokhande, C.D & Chan-Jin Park 2013 (B), 'Surfactant-assisted morphological tuning of hierarchical CuO thin films for electrochemical supercapacitors', Dalton Transactions, vol. 18, pp. 6237 – 6656.
30. Dubal, D.P, Dhawale, D.S, Salunkhe, R.R, Jamdade, V.S, Lokhande, C.D 2010, 'Fabrication of copper oxide multilayer nanosheets for supercapacitor application', Journal of Alloys & Compounds, vol. 492, pp.26–30.
31. Dubal, D.P, Gund , G.S, Lokhande, C.D, Rudolf Holze 2013 (A),'CuO cauliflowers for supercapacitor application: Novel potentiodynamic deposition', Materials Research Bulletin, vol. 48, pp.923–928.

32. Emil Roduner, 2006, 'Size matters: why nanomaterials are different', Chemical Society Reviews., vol. 35,pp. 583–592
33. Endut, Z, Hamdi, M & Basirun, W.J 2013, 'Pseudocapacitive performance of vertical copper oxide nanoflakes', Thin Solid Films, vol. 528, pp.213–216.
34. Fan, L.Z & Maier, J 2006, 'High performance polypyrrole electrode materials for redox supercapacitors', Electrochemistry Communications, vol. 8, pp. 937-940.
35. Felix, S, Bala, R, Praveen Chakkravarthy & Nirmala Grace, A 2015, 'Microwave assisted synthesis of copper oxide & its application in electrochemical sensing', Materials Science and Engineering, vol. 73, pp. 012115.
36. Feynman, R.P 1960, 'There's Plenty of room at the bottom', Engineering and science, pp. 22-36.
37. Frackowiak, E & Beguin, F 2001, 'Carbon materials for the electrochemical storage of energy in capacitors', Carbon, vol. 39, pp. 937-950.
38. Frackowiak, E, Khomenko, V, Jurewicz, K, Lota, K & Beguin, F 2006, 'Supercapacitors based on conducting polymers/nanotubes composites', Journal of Power Sources, vol. 153, pp. 413-418.
39. Ghadge, T.S & Lokhande, B. J 2015,'Electrochemical Characterization of Cathodized Copper Oxide Thin Films', Journal of Nuclear Physics, Material Sciences, Radiation and Applications, vol. 2, no. 2 pp. 159–167.
40. Guanhua Chen, Jean-Marc Langlois, Yuejin Guo, & William A. Goddard III 1989, 'Superconducting properties of copper oxide high-temperature superconductors', Proceedings of the National Academy of Sciences: USA, vol. 86, pp. 3447-3451.
41. Guiling Wang, Jichun Huang, Shuli Chen, Yinyi Gao & Dianxue Cao 2011, Preparation and supercapacitance of CuO nanosheet arrays grown on nickel foam', Journal of Power Sources, vol.196, pp. 5756–5760.
42. Guo, X, Mao, D, Lu, G, Wang, S, Wu, G 2010, 'Glycine-nitrate combustion synthesis of CuO–ZnO–ZrO_2 catalysts for methanol synthesis from CO_2 hydrogenation',Journal of Catalysis, vol. 271, pp. 178–185.
43. Gupta, V. & Miura, N 2006, 'High performance electrochemical supercapacitor from electrochemically synthesized nanostructured polyaniline', Materials Letters, vol. 60, pp. 1466-1469.
44. Hafsa, S.M.S, Qureshi, F & Haque, Z 2016, 'Surfactant assisted wet chemical synthesis of copper oxide nano strucutures and their spectroscopic analysis', Optik, vol. 127, pp. 2740-2747.

45. Hamed Sadabadi, Adeleh Aftabtalab, Shirzad Zafarian, Ch, Shilpa Chakra, K. Venkateswara Rao & Sarah Shaker 2015, 'Influence of fuel & condition in combustion synthesis on properties of copper (II) oxide nanoparticle', Advanced Materials Research, vol. 829, pp. 152-156.
46. Hao-Wen Wu, Siang-Yun Lee, Wen-Chung Lu & Kao-Shuo Chang 2015, 'Piezoresistive effects enhanced the photocatalytic properties of Cu_2O/CuO nanorods', Applied Surface Science, vol. 344, pp. 236–241.
47. He, S, Hu, C, Hou, H &Chen, W 2014, 'Ultrathin MnO2 nanosheets supported on cellulose based carbon papers for high-power supercapacitors', Journal Power Sources, vol. 246, pp.754–761.
48. Ho¨lzer ,G, Fritsch, M, Deutsch, M, Ha¨rtwig, J & Fo¨rster1, E 1997, '$K_{\alpha 1,2}$ and $K_{\beta 1,3}$ x-ray emission lines of the 3*d* transition metals', Physical Review A vol. 56, no. 6 pp. 4554-4568.
49. Hoffmann, M.R, Martin, S.T, Wonyong Choi, & Bahnemannt, D.W 1995, 'Environmental Applications of Semiconductor', Photocatalysis Chemical Review, vol. 95, pp. 69-96.
50. Honghong Nan, Wenqin Ma, Qingqing Hu & Xiaojun Zhang 2015, 'Copper oxide nanofilm on 3D copper foam as a novel electrodematerial for supercapacitors', Applied Physics A, vol. 119, pp. 1451–1457.
51. Hu, C-C, K-H, lin, M-C & Wu, Y-T 2006, 'Design and Tailoring of the Nanotubular Arrayed Architecture of Hydrous RuO_2 for Next Generation Supercapacitors', Nano Letters, vol. 6, pp. 2690-2695.
52. Huaxia Shi, Yunxuan Zhao, Na Li, Kai Wang, Xia Hua, Mindong Chen & Fei Teng 2014, 'Synthesis & photo catalytic activity of novel CuO Cauliflowers grown from $Cu(OH)_2$', Catalysis communications, vol. 47, pp. 7 -12.
53. Hui Wang, Jin-Zhong Xu, Jun-Jie Zhu &Hong-Yuan Chen 2002,'Preparation of CuO nanoparticles by microwave irradiation', Journal of Crystal Growth vol. 244, pp. 88–94.
54. Hui Xia, Ying Shirley Meng, Guoliang Yuan, Chong Cui, & Li Luc, A 2012, 'Symmetric RuO_2/RuO_2 Supercapacitor Operating at 1.6 V by Using a Neutral Aqueous Electrolyte', Electrochemical & Solid-State Letters, vol. 15, no. 4, pp. A60-A63.

55. Huxia Shi, Yunxuan Zhao, Na Li, Kai Wang Xia Hua, Mindong Chen & Fei Teng 2012, 'Synthesis & photocatalytic activity of novel CuO cauliflowers grown from $Cu(OH)_2$', Catalytic Communication, vol. 47, pp. 7 – 12.
56. Jayalakshmi, M & Balasubramanian, K 2008, 'Simple Capacitors to Supercapacitors - An Overview', International Journal of Electrochemical Science, vol. 3, pp. 1196 – 1217.
57. Jayalakshmi, M, Mohan Rao, M, Venugopal, N & Kwang-Bum Kim 2007,'Hydrothermal synthesis of SnO_2–V_2O_5 mixed oxide and electrochemical screening of carbon nano-tubes (CNT), V_2O_5, V_2O_5–CNT, and SnO_2–V_2O_5–CNT electrodes for supercapacitor applications', Journal of Power Sources, vol. 166, pp. 578- 583.
58. Jegatha Christy, A, Nehru, L.C & Umadevi, M 2013, 'A novel combustion method to prepare CuO nanorods and its antimicrobial and photocatalytic activities', Powder Technology, vol. 235, pp. 783–786.
59. Jia Dianzeng, Yu Jianqun & Xia Xi 1998, 'Synthesis of CuO nanometer powder by one step solid state reaction at room temperature', Chinese Science Bulletin, vol. 43, no. 7, pp. 571- 573.
60. Jiang, Z 2009, 'Copper oxide nanosheets synthesized by hydrothermal proecess', Chinese Physics letters, vol. 26, pp. 0862021-0862023.
61. Jingang Zhao, Renming Liu & Zhenghe Hua 2015, 'Hydrothermal synthesis & optical properties of single crystalline CuO nanosheets', Superlattices and Microstructures, vol. 81, pp. 243-247.
62. Junwu, Z, Huiping, B, Yanping, W, Xin, W, Xujie, Y & Lude, L 2007, 'Synthesis of flower like copper oxide nanostructures via a simple hydrolysis route', Materials letters, vol. 61, pp. 5236-5238.
63. Jurewicz, K, Delpeux, S, Bertagna, V, Beguin, F & Frackowiak, E 2001, 'Supercapacitors from nanotubes/polypyrrole composites', Chemical Physics Letters, vol. 347, pp. 36-40.
64. Kankanit Phiwdang, Sineenart Suphankij, Wanichaya Mekprasart & Wisanu Pecharapa 2013, 'Synthesis of CuO Nanoparticles by Precipitation Method Using Different Precursors', Energy Procedia, vol. 34, pp. 740 – 745.
65. Karthick Prabhu, S, Hirankumar, G, Maheswaran, A, DariesBella, R. S & Sanjeeviraja, C 2014, 'Structural & electricalstudies on Zn^{2+} doped $LiCoPO_4$', Journal of Electrostatics, vol. 72, pp. 181-186.

66. Ke, F.S, Huang, L, Wei, G.Z, Xue, L.J, Li, J.T, Zhang, B, Chen, S.R, Fan, X.Y & Sun, S.G 2009, ' One-step fabrication of CuO nanoribbons array electrode & its excellent lithium storage performance', Electrochimica Acta, vol. 54, pp. 5825–5829.
67. Kebin Zhou, Ruipu Wang, Boqing Xu & yadong Li 2006, 'Synthesis, characterization and catalytic properties of CuO nanocrystals with various shapes', Nanotechnology, vol. 17, pp. 3939 – 3943.
68. Kim, S.H, Ahmad Umar, Rajesh Kumar, Ahmed A. Ibrahim & Kumar, G 2015, 'Facile synthesis and photocatalytic activity of cocoon-shaped CuO nanostrucures', Materials Letters, vol. 156, pp. 138-141.
69. Kotz, R & Carlen, M 2000, 'Principles & applications of electrochemical capacitors', Electrochimica Acta, vol. 45, pp. 2483–2498.
70. Krishnamoorthy, K, & Sang-Jae Kim 2013, 'Growth, characterization & electrochemical properties of hierarchical CuO nanostructures for supercapacitor applications', Materials Research Bulletin, vol. 48, pp. 3136–3139.
71. Kumar, R.V, Diamant, Y & Gedanken, A 2000, 'Sonochemical synthesis & characterization of nanometer-size transition metal oxides from metal acetates', Chemistry of Materials, vol. 12, pp. 2301-2305.
72. Likun Zheng & Xinjian Liu 2007, 'Solution-phase synthesis of CuO hierarchical nanosheets at near-neutral pH & near-room temperature', Materials Letters, vol. 61, pp. 2222–2226.
73. Liu, J, Jun, J, Zhao, D, Shao-Zhuan, H, Zhi-Yi, H, Li, W, Chao, W, Li-Hua, Ch, Yu, L, Van Tendeloo, G & Bao-Lian, S 2012, 'Tailoring CuO nanostructures for enhanced photo catalytic property', Journal of Colloid & Interface Science, vol. 384, pp. 1-9.
74. Liutao Yu, Yuanyuan Jin, Lanlan Li, Jie Ma, Guangfeng Wang, Baoyou Geng & Xiaojun Zhang 2013, '3D Porous Gear-like Copper Oxide and their High Electrochemical Performance as Supercapacitor', Crystal Engineering communication, vol.15, pp. 7657-7662.
75. Lu, C.H, Qi, L.M, Yang, J.H, Wang, X.Y, Zhang, D.Y, Xie, J.L & Ma, J.M 2005, 'One-Pot Synthesis of Octahedral Cu_2O Nanocages via a Catalytic Solution Route', Advanced Materials, vol. 17, pp. 2562-.2567.
76. Mageshwari, K, Sathyamoorthy, R & Jinsub Park 2015, 'Photocatalytic activity of hierarchical CuO microspheres synthesized by facile reflux condensation method', Powder Technology, vol. 278, pp.150-156.

77. Mahdi Shahmiri, Nor AzowaIbrahim , NastaranFaraji , Wan Mahmood Mat Yunus , Nilofar Asim & Norhazlin Zainuddin 2013, 'Third-order nonlinear optical properties of chemically synthesized copper oxide nanosheets', Physica E vol. 54, pp. 109–114.
78. Malka Rochkind, Sagi Pasternak & Yaron Paz 2015, 'Using Dyes for evaluating photocatalytic properties: A critical review', Molecules, vol. 20, pp. 88-110.
79. Mallick, P & Sahu, S 2012, 'Structure, microstructure & optical absorption analysis of CuO nanoparticles synthesized by sol–gel route', Journal of Nanoscience and Nanotechnology, vol. 2, no.3, pp. 71–74.
80. Mariappan, C.R, Govindaraj, G,Vinoth Rathan, S & Vijaya Prakash, G 2005, 'Preparation, Characterization, ac conductivity & permittivity studies on vitreous $M_4AlCdP_3O_{12}$ (M = Li, Na, K) system', Materials Science and Engineering B, vol. 121, pp. 2–8.
81. Mastragostino, M, Arbizzani, C & Soavi, F 2001, 'Polymer-based supercapacitors', Journal of Power sources, vol. 97-98, pp. 812-815.
82. Meshram, S.P, Adhyapak, P.V, Mulik, U.P & Amalnerkar, D.P 2012, 'Facile synthesis of CuO nanomorphs & their morphology dependent sunlight driven photocatalytic properties', Chemical engineering journal, vol. 204 – 206, pp. 158 – 168.
83. Minhua Cao, Yonghui Wang, Caixin Guo, Yanjuan Qi, Changwen Hu, & Enbo Wang, J. A, 2004, 'Simple Route Towards CuO Nanowires and Nanorods', Journal of Nanoscience and Nanotechnology, Vol. 4, No. 7, pp. 824-828
84. Mohamed Fterich, Férid Ben Nasr, Ramzi Lefi, Mohamed Toumi & Samir Guermazi 2016, 'Effect of concentration of hexamethylenetetramine in structure, microstructure & optical properties of CuO nanoparticles synthesized by hydrothermal route,' Materials Science in Semiconductor Processing, vol. 43, pp. 114–122.
85. Mohammad Mansoob Khan, Syed Farooq ,Adil & Abdullah Al-Mayouf 2015, 'Metal oxides as photocatalysts', Journal of Saudi Chemical Society, vol. 19, no. 5, pp. 462-464.
86. Momeni, M.M, Nazari, Z, Kazempour, A, Hakimiyan, M & Mirhoseini, S. M 2014, 'Preparation of CuO nanostructures coating on copper as supercapacitor materials', Surface Engineering, vol.30, no.11, pp.775 – 778.
87. Morales, J, Sanchez, L, Martin, F, Ramos-Barrado, J.R & Sanchez, M 2005, 'Use of low-temperature nanostructured CuO thin films deposited by spray-pyrolysis in lithium cells', Thin Solid Films, vol. 474, pp. 133.

88. Narongdet Wong pisutpaisan, Piyanut Charoonsuk, Naratip Vittayakorn & Wisanu Pecharapa 2011, 'Sonochemical Synthesis & Characterization of Copper Oxide Nanoparticles', Energy Procedia, vol. 9, pp. 404 – 409.
89. Nikam, A.V, Arulkashmir, A, Krishnamoorthy, K, Kulkarni, A. A & Prasad, B. L. V 2014, 'pH-Dependent Single-Step Rapid Synthesis of CuO & Cu_2O Nanoparticles from the Same Precursor', Crystal Growth & Design, vol. 14, no. 9, pp. 4329–4334.
90. Nillohit Mukherjee, Bihutibhushan show, swarup Kumar Maji, Utpal Madhu, Sanjib kumar Bhar Bibhas Ch&ra mitra, Gobinda Gopal khan & Anup Mondal 2011, 'CuO nanowhiskers: Electrodeposition, Raman analysis, Photoluminescence study & photocatalytic activity', Materials letters, vol. 65, pp. 3248 – 3250.
91. Nishtar Nishad Fathima, Anantanarayanan Rajaram, Sreedhar, B & Asit Baran Mandal, 2008, 'The formation of Copper Oxide Nanorods in the Presence of Various Surfactant Micelles', Indian Journal of Science and Technology, vol.1, no. 7, pp.1-6
92. Nobre, M.A.L & Lanfredi, S 2001, 'Dielectric properties of $Bi_3Zn_2Sb_3O1_4$ ceramics at high temperature', Materials Letters, vol. 47, pp. 362 – 366.
93. Oberdo¨ rster, G, Oberdo¨ rster, E, Oberdo¨ rster, J 2005, 'Nanotoxicology: an emerging discipline evolving from studies of ultrafine particles', Environmental Health Perspectives, vol. 113, pp. 823–839.
94. Ovchinnikov, S.G, Gizhevskii, B.A, Sukhorukov, Y.P, Ermakov, A.E, Uimin, M.A,Kozlov, E.A, Kotov, Y & Bagazeev, A.A.V 2007, 'Specific features of the electronic structure & optical spectra of nanoparticles with strong electron correlations', Physics of the Solid State, vol. 49, pp.1116.
95. Pallavi Amet, Anil kumar, Rameshwar Amet & Malkani, R.K 2010, 'A comparative study of Photocatalytic Activity of some coloured semiconducting oxides', Iranian Journal of Chemical Engineering, vol. 29, no.2, pp. 43-48.
96. Pandolfo, A.G & Hollenkamp, A.F 2006, 'Carbon properties & their role in supercapacitors', Journal of Power Sources, vol. 157, no.1, pp. 11-27.
97. Pang, S. C, Anderson, M. A & Chapman, T. W. J 2000,' Novel Electrode Materials for Thin-Film Ultracapacitors: Comparison of Electrochemical Properties of Sol-Gel-Derived and Electrodeposited Manganese Dioxide', Journal of Electrochemical Society, vol. 147, no.2, pp. 444-450
98. Patake, V.D, Joshi, S.S, Lokhande, C.D & Oh-Shim Joob 2009, 'Electrodeposited porous & amorphous copper oxide film for application in supercapacitor', Materials Chemistry and Physics, vol. 114, pp. 6–9.

99. Pitkethly, M.J 2004, 'Nanomaterials – the driving force', Nanotoday 2004, pp. 21- 29.
100. Ponpandian, N & Narayanasamy, A 2002, 'Influence of grain size & structural changes on the electrical properties of nanocrystalline zinc ferrite', Journal of applied Physics, vol. 92, no. 5, pp. 2770-2778.
101. Prakash Chand, Anurag Gaur & Ashavani Kumar 2011, 'Study of CuO Nanoparticles Synthesized by Solgel Method', AIP Conference Processing, vol. 1393, pp. 211- 212.
102. Prakash Chandra, S, Manisha, A, Sunil, Ch, Manoj, K & Sandeep, Ch 2014, 'Structural, magnetic, vibrational and impedance properties of Pr and Ti co doped $BiFeO_3$ multiferroic ceramics', Ceramic International, vol. 40, pp.7805-7816.
103. Prakash, Ch, Anurag, G, Ashavani, K & Umesh, K. G 2015, 'Effect of NaOH molar concentration on morphology, Optical & ferroelectric properties of hydrothermally grown CuO nanoplates', Materials Science: Semiconductors Processing, vol. 38, pp. 72-80.
104. Priyanka Jha, A. K 2013, 'Electrical characterization of zirconium substituted barium titanate using complex impedance spectroscopy', Bulletin of Materials Science, vol. 36, pp. 135-141.
105. Qingwei Zhu, Yihe Zhang, Jiajun Wang, Fengshan Zhou & Paul K.Chu 2011, 'Microwave Synthesis of Cuprous Oxide Micro-/Nanocrystals with different Morphologies & Photocatalytic Activities', Journal of Material Science & Technology, vol. 27, pp. 289 -295.
106. Qu, D.Y & Shi, H 1998, 'Studies of activated carbons used in double-layer capacitors', Journal of Power Sources, vol. 74, no.1, pp. 99-107.
107. Rahman, A. U, Rafiq, M. A, Karim, S, Maaz, K, Siddique, M & Hasan, M. M 2011, 'Reduced conductivity and enhancement of debye orientational polarization in lanthanum doped Cobalt ferrite nanoparticles' Physica B, vol. 406, No. 23, pp. 4393–4399.
108. Rajendra Prasad, K & Miura, N 2004, 'Electrochemically deposited nanowhiskers of nickel oxide as a high-power pseudocapacitive electrode', Applied Physics Letters, vol.85, no. 18 pp. 4199-4201
109. Rao, K.S, Krishna, P.M, Prasad, D.M 2007,' Effect of simultaneous substitution of Li^+ and Ti^{4+} in ceramics of $Pb_2KNb_5O_{15}$ on structure, dielectric, modulus, impedance and conductivity properties, Physics Status Solidi (b), vol. 244, No.6, pp. 2267-2287.

110. Rauf, M.A & Salman Ashraf, S 2009, 'Fundamental Principles & application of heterogeneous photocatalytic degradation of dyes in solution', Chemical Engineering Journal, vol. 151, pp. 10-18.
111. Razium Ali Soomroa, Keith Richard Hallam, Zafar Hussain Ibupotob, Aneela Tahira, Syed Tufail Hussain Sherazi, Sirajjuddin, Safia Sanam Memon & Magnus Willander, 2015,' Amino acid assisted growth of CuO nanostructures and their potential application in electrochemical sensing of organophosphate pesticide', Electrochimica Acta, vol. 190, pp. 972-979
112. Rehman, S, Mumtaz A & Hasanain, S.K 2011, 'Size effects on the magnetic & optical properties of CuO nanoparticles', Journal of Nanoparticle Research, vol. 13, pp. 2497.
113. Ren, G, Hu, D & Cheng, E.W.C 2009,'Characterization of copper oxide nanoparticles for antimicrobial applications', International Journal of Antimicrobiology Agents, vol. 33, pp. 587–590.
114. Samarasekara, P, Kumara, N.T.R.N & Yapa, N U S 2006, 'Sputtered copper oxide (CuO) thin films for gas sensor devices', Journal of Physics: Condensed Matter, vol. 18, pp. 2417–2420.
115. Sarkar, S, Pradip Kumar Jana, Chaudhuri, B. K & Sakata, H 2006, 'Copper (II) oxide as a giant dielectric material', Applied Physics Letters, vol. 89, pp. 212905-1 -3.
116. Sayer M, Mansingh A, Webb J B et al 1978,'Long range potential centers in disordered solids', Journal of physics C: solid state physics, vol. 11, pp. 315 – 320.
117. Sen, S, Choudhary, R.N.P, Tarafdar, A & Pramanik, P 2006, 'Impedance spectroscopy study of strontium modified lead zirconate titanate', Ceramics Journal of Applied Physics, vol.99, pp.124114-1-8.
118. Senthilkumar, V, Yong Soo Kim, Chandrasekaran, S, Balasubramaniyan Rajagopalan, Eui Jung Kim & Jin Suk Chung 2013, 'Comparative supercapacitance performance of CuO nanostructures for energy storage device applications' RSC advances, vol.5, pp.20545-20553.
119. Sergiu T.ShishiyanuTeodor, S.ShishiyanuOleg I.Lupan 2006, 'Novel NO2 gas sensor based on cuprous oxide thin films', Sensors & Actuators B: Chemical, vol. 113, no. 1, pp. 468-476.
120. Seyyed Ebrahim Moosavifard, El-Kady, M.F, Mohammad, S. Rahmanifar, Kaner, R.B & Mir Fazlollah Mousavi 2015, 'Designing 3D highly ordered nanoporous CuO electrodes for high-performance asymmetric supercapacitors', ACS Applied Material Interfaces, vol. 7, no.8, pp. 4851–4860.

121. Shen-Ming Chen,Rasu Ramachandran, Veerappan Mani & Ramiah Saraswathi 2014, 'Recent Advancements in Electrode Materials for the Highperformance Electrochemical Supercapacitors: A Review', International Journal Electrochemical Science, vol. 9, pp. 4072 – 4085.
122. Shi, H 1996,'Activated carbons & double layer capacitance', Electrochimica Acta, vol. 41, no. 10, pp. 1633-1639.
123. Shinde, S. K, Dubal, D. P, Ghodake, G. S & Fulari, V.J 2015, 'Hierarchical 3D-flower-like CuO nanostructure on Copper foil for Supercapacitors', RSC Advances, vol. 5, pp. 4443-4447.
124. Shrabanee Sen, Mishra, S. K, Sagar Palit, S, Das, S.K, Tarafdar, A 2008,'Impedance analysis of 0.65 $Pb(Mg_{1/3}Nb_{2/3})O_{3-0.35}$ $PbTiO_3$ ceramic', Journal of Alloys & Compounds, vol. 453, pp. 395–400.
125. Sonia, S, Poongodi, S, Suresh Kumar, P, Mangalaraj, D, Ponpandian, N & Viswanathan, C 2015,' Hydrothermal synthesis of highly stable CuO nanostructures for efficient photocatalytic degradation of organic dyes', Materials Science in Semiconductor Processing, vol. 30, pp. 585–591.
126. Stoller, M.D & Ruoff, R. S 2010,'Best practice methods for determining an electrode material's performance for ultracapacitors', Energy Environment Science, vol. 3, pp. 1294–1301.
127. Sukhorukov, Yu.P, Gizhevskii, B.A, Mostovshchikova, E. V, Yermakov, A. Ye, Tugushev, S.N & Kozlov, E. A 2006, 'Nanocrystalline Copper Oxide for Selective Solar Energy Absorbers',Technical Physics Letters, vol. 32, no. 2, pp. 132–135.
128. Suman, C. K, Prasad, K & Choudhary, R. N. P 2005, 'Impedance spectroscopic studies of ferroelectric $Pb_2Sb_3DyTi_5O_{18}$ ceramic', Advances in Applied Ceramics, vol. 104, no.6, pp. 294-296.
129. Sun, T, Yan, Y, Zhao, Y, Guo, F & Jiang, G 2012,'Copper oxide nanoparticles induce autophagic cell death in A549 cells', Plos one, vol. 7, pp. e43442.
130. Suramwar, N.V, Thakare, S.R & Khaty, N.T, 2012, 'Synthesis and catalytic properties of nano CuO prepared by soft chemical method', International Journal of Nano Dimension, Vol. 3, no. 1, pp.75-80
131. Suresh , P, Umabala, A.M, Prasada Rao, A.V 2015, 'Rapid sunlight degradation of Rhodamine-B, Methylene blue, Methyl Orange, Congo red and their binary mixtures using suprastoichiometric Bi-Molybdate', International Journal of engineering and Applied Sciences, vol. 2, pp. 42 – 46.

132. Suresh Sagadevan & Priya Murugasen 2015, 'Electrical Properties of Copper Oxide Nanoparticles', Journal of Nanoparticle Research, vol. 30, pp. 1-8.
133. Syeda Amber Yousaf & Salamat Ali 2007-2008,'Why Nanoscience & Nanotechnology? What is there for us', Journal of Faculty of Engineering & Technology, pp. 11- 20.
134. Tanmaya Badapanda, Ranjan Kumar Harichandan, Sudhasu Sekhar Nayak, Avinna Mishra & Sahid Anwar 2014, 'Frequency & temperature dependence behaviour of impedance,modulus & conductivity of BaBi4Ti4O15 Aurivillius ceramic', Processing & Application of Ceramics, vol. 8, no.3, pp.145–153.
135. Tao Hong, Kyle Brinkman & Changrong Xia 2016, 'Copper oxide as a synergistic catalyst forthe oxygen reduction reaction on $La_{0.6}Sr_{0.4}Co_{0.2}Fe_{0.8O}$ perovskite structured electrocatalyst', Journal of Power Sources, vol. 329, pp. 281- 289.
136. Tariq Jan, Javed Iqbal, Umar Farooq, Asma Gul, Rashda Abbasi, Ishaq Ahmad & Maaza Malik 2015, 'Structural, Raman & optical Characteristics of Sn doped CuO Nanostructures: A novel anticancer agent', Ceramics International, vol. 41, pp. 29-35.
137. Thanh Son, V, Le Van Phong, Md. Nazrul Islam, Tran Quang Hung, Sarah Kim, Jun-Ho Jeong, CheolGi Kim & Jong-Ryul Jeong 2010, 'Effect of Non-ionic Igepal CO-520 in Sonochemical Synthesis of Monodisperse Fe3O4 Nanoparticles', Journal of Magnetics, vol. 15, no.3,pp. 112-115.
138. Tranquada, J.M, Sternlleb, B.J, Axe, J.D, Nakamura, Y & Uchida, S 1995,'Evidence for stripe correlations of spins and holes in copper oxide superconductors Nature', vol. 375, no.15, pp. 561 -563.
139. Uma Nerle & M. K. Rabina, 2013, 'Thermal Oxidation of Copper for Favorable Formation of Cupric Oxide (CuO) Semiconductor', Journal of Applied Physics, vol. 5, no.1, pp. 01-07.
140. Vahidshad, Y, Abdizadeh, H, Baharvandi, H. R & Akbari Baseri, M 2011, 'Sol-Gel Synthesis and Characterization of Copper stabilized Zirconia Nanoparticles', International Journal of Modern Physics B, vol. 25, no. 21 pp. 2823–2839.
141. Vijaya Kumar, B, Sankarappa , T, Santosh Kumar, Prashant Kumar, M, Sadashivaiah, P.J &Ramakrishna Reddy, R 2009, 'Dielectric properties & conductivity in CuO and MoO3 doped borophosphate glasses', Physica B, vol. 404, pp. 3487–3492. (Reference Particle size analyzer)

142. Vijaya Kumar, R, Elgamiel, R, Diamant, Y & Gedanken, A 2001, Sonochemical Preparation and Characterization of Nanocrystalline Copper Oxide Embedded in Poly(vinyl alcohol) and Its Effect on Crystal Growth of Copper Oxide', Langmuir, vol.17 , no.5, pp. 1406–1410.
143. Visalakshi, S, Kannan, R, Valanarasu, S, Kathalingam, A & Rajashabala, S 2017, 'Studies on optical & electrical properties of SILAR-deposited CuO thin films', Materials Research Innovation, vol. 21, pp. 146 – 151.
144. Wanchanthuek, R & Nunrung, W 2001, 'The adsorption study of Methylene blue onto MgO from various preparation methods', Journal of Environmetnal Science & Technology, vol. 4, no. 5, pp. 534-542.
145. Wang, S.L, Li, P.G, Zhu, H.W & Tang, W.H 2012,'Controllable synthesis & Photocatalytic property of uniform CuO/Cu_2O composite hollow microspheres'. Powder Technology, vol. 230, pp 48- 53.
146. Wang, S.Q, Zhang, J.Y & Chen, C.H 2007, 'Dandelion-like hollow microspheres of CuO as anode material for lithium-ion batteries', Scripta Materialia, vol. 57, pp. 337.
147. Wang, S.Y, HO, K.C, Kuo, S.L & Wu, N.L 2006,' Investigation on Capacitance Mechanisms of Fe3O4 Electrochemical Capacitors', Journal of Electrochemical Society, vol.153,no.1 pp. A75-A80.
148. Wang, W, Zhan, Y & Wang, 2001, 'One-step, solid-state reaction to the synthesis of copper oxide nanorods in the presence of a suitable surfactant', Chemical Communication, No. 8, pp.727-728
149. Wang, X, Hu, C, Liu, H, Du, G, He, X& Xi, Y 2010, 'Synthesis of CuO nanostructures & their application for nonenzymatic glucose sensing', Sensing Actuators B: Chemistry, vol. 144, pp. 220–225.
150. Wang, X. F, Wang, D. Z & Liang, L 2003, 'Electrochemical Capacitor Using Nickel Oxide/Carbon Nanotube Composites Electrode', Journal of Inorganic Materials, vol. 18, no.2 pp. 331-336.
151. Wang, X.X, Tang, X.G, Chan, & H.L.W 2004,' Electromechanical and ferroelectric properties of $(Bi_{1/2}Na_{1/2})TiO_3$–$(Bi_{1/2}K_{1/2})TiO_3$–$BaTiO_3$$(Bi_{1/2}Na_{1/2})TiO_3$–$(Bi_{1/2}K_{1/2})TiO_3$–$BaTiO_3$ lead-free piezoelectric ceramics, Applied Physics Letters, vol. 85, no.1, pp. 91-94.

152. Wei Changa, Xiaosai Rena, Guorui Yangb, Wei Yanb, & Yanrong Guoa 2015, 'Synthesis & Photocatalytic Activity of $Zn_xCd_{1-x}S/TiO_2$ Heterostructures Nanofibre Prepared by Combining Electrospinning and Hydrothermal Method', South African Journal of Chemistry, vol. 68, pp. 138–142.
153. Xia Hui-li, Zhuang Hui-sheng, Zhang Tao, & Xiao Dong-chang 2007, 'Photocatalytic degradation of Acid Blue 62 over $CuO\text{-}SnO_2$ nanocomposite photocatalyst under simulated sunlight', Journal of environmental sciences vol. 19, pp. 1141-1145.
154. Xiang, J.Y, Tu, J.P, Huang, X.H & Yang, Y.Z 2008, 'A comparison of anodically grown CuO nanotube film and Cu_2O film as anodes for lithium ion batteries', Solid State Electrochemistry, vol. 12, pp. 941-945.
155. Xiaoqiang Du, Jingwei Huang, Yingying Feng & Yong Ding 2016, 'Flower-like 3D CuO microsphere acting as photocatalytic water oxidation catalyst', Chinese Journal of Catalysis, vol. 37,pp.123–134.
156. Xinyuan Zhao, Wei, C.M, Yang, L & Chou, M.Y 2004, 'Quantum Confinement and Electronic Properties of Silicon Nanowires', Physical Review Letters, vol. 92, pp. 236805-1- 4.
157. Xu, Y, Wang, J, Sun, W & Wang, S 2006, 'Capacitance properties of poly-(3,4-ethylenedioxythiophene)/polypyrrole composites', Journal of Power Sources, vol. 159, pp. 370-373.
158. Xueqin Liu, Zhen Li, Quiang Zhang, Fei Li & Tao Kong 2012, 'CuO nanowires prepared via a facile solution route & their photocatalytic property', Materials Letters, vol. 72, pp. 49 – 52.
159. Yang, W, Gao, Z, Ma,J, Zhang, X &Wang, J, 2014 ' Controlled synthesis of Co3O4 andCo_3O_4@MnO_2 nanoarchitectures and their electrochemical capacitor application, Journal of Alloys and Compounds', vol.611, pp. 171–178.
160. Yange Zhang, Shutao Wang, Xiong Wang, Yitai Qian, & Zude Zhang , 2006, 'Assembled CuO Hollow Spheres from Nanoparticles' , Journal of Nanoscience and Nanotechnology, Vol.6, pp. 1423–1426.
161. Yu Li, Xiao –Yu Yang, Joanna Rooke, Guastaaf Van Tendeloo & Bao- Lian Su 2010, 'Ultralong $Cu(OH)_2$ & CuO nanowire bundles: PEG 200 – directed crystal growth for enhanced photocatalytic performance', Journal of Colloid Interface Science, vol. 348, pp. 303 – 312.

162. Yu Xin Zhang, Ming Huang, Fei Li & Zhong Quan Wen 2008, 'Controlled Synthesis of Hierarchical CuO Nanostructures for Electrochemical Capacitor Electrodes', Materials Research Bulletin, vol. 43, pp. 3221–3226.
163. Yu Xin Zhang, Ming Huang, Fei Li & Zhong Quan Wen, 2013, 'Controlled Synthesis of Hierarchical CuO Nanostructures for Electrochemical Capacitor Electrodes', International Journal of Electrochemical Science, vol.8, p.p 8645 – 8661
164. Yuan, C, Bin Wu, H, Xie,Y,. Lou & X.W.D, 2014, ' Mixed transition-metal oxides: design,synthesis, and energy-related applications, Angewandte Chemie, Vol. 53, pp. 1488–1504.
165. Yuanyuan Ma, Hao Li , Rongfang Wang , Hui Wang , Weizhong Lv & Shan Ji 2015,'Ultrathin willow-like CuO nanoflakes as an efficient catalyst for electro-oxidation of hydrazine', Journal of Power Sources, vol. 289, pp. 22- 25.
166. Yu-Ch & Hua Ch, Z 2004, 'Controlled synthesis and self assembly of single crystalline copper oxide nanorods and nanoribbons', Crystal growth design, vol. 4, pp. 397-402.
167. Yueming Li, Jing Liang, Zhanliang Tao, Jun Chen 2008, 'CuO particles and plates: Synthesis & gas-sensor application', Materials Research Bulletin, vol. 43, pp. 2380–2385.
168. Yu-Kuei Hsu , Ying-Chu Chen & Yan-Gu Lin, 2012, 'Characteristics and electrochemical performances of lotus-like CuO/$Cu(OH)_2$ hybrid material electrodes' Journal of Electroanalytical Chemistry, vol. 673, pp.3–47
169. Zayyoun, N, Bahmad, L, Laanab, L & Jaber, B 2016, 'The effect of pH on the synthesis of stable Cu_2O/CuO nanoparticles by sol–gel method in a glycolic medium, Applied Physics A, vol. 122, pp. 1- 6.
170. Zhang, H, Jing Feng & Milin Zhang 2013, 'Preparation of flower-like CuO by a simple chemical precipitation method and their application as electrodematerials for capacitor', Materials Research Bulletin, vol. 43, pp. 3221–3226.
171. Zhang, P, Zhang, L, Zhao, G.C & Feng, F 2012, 'A highly sensitive nonenzymatic glucose sensor based on CuO nanowires', Microchimica Acta, vol. 176, pp. 411–417.
172. Zhang, Q, Zhang, K, Xu, D, Yang, G, Huang, H, Nie, F, Liu, C, & Yang, S, 2014, 'CuO nanostructures: synthesis, characterization, growth mechanisms, fundamental properties, and applications,' Progress in Materials Science vol. 60, pp. 208–337.
173. Zhongli Hu & Hongdong Liu, 2015, 'Three-dimensional CuO micro flowers as anode materials for Li-ion batteries', Ceramics International, vol. 41, no.6, pp. 8257-8260
174. Zou, X, Zhang, S, Shi, M & Kong, J 2007, 'Remarkably enhanced capacitance of ordered polyaniline nanowires tailored by stepwise electrochemical deposition', Journal of Solid State Electrochemistry, vol. 11, pp. 317-322.